DNA and Metal Ion Mediated Modification of Nanomaterials

by

Zhicheng Huang

A thesis

presented to the University of Waterloo

in fulfillment of the

thesis requirement for the degree of

Doctor of Philosophy

in

Chemistry

Waterloo, Ontario, Canada, 2021

Examining Committee Membership

The following served on the Examining Committee for this thesis. The decision of the Examining Committee is by majority vote.

External Examiner	**Dr. Jennifer I-Ling Chen** Associate Professor, Department of Chemistry, York University, Toronto, Canada
Supervisor	**Dr. Juewen Liu** Professor, Department of Chemistry, University of Waterloo, Waterloo, Canada
Internal Member	**Dr. Vivek Maheshwari** Associate Professor, Department of Chemistry, University of Waterloo, Waterloo, Canada
Internal Member	**Dr. Thorsten Dieckmann** Associate Professor, Department of Chemistry, University of Waterloo, Waterloo, Canada
Internal Member	**Dr. Shawn Wettig** Professor, School of Pharmacy, University of Waterloo, Waterloo, Canada

Author's Declaration

This thesis consists of material all of which I authored or co-authored: see Statement of Contributions included in the thesis. This is a true copy of the thesis, including any required final revisions, as accepted by my examiners.

I understand that my thesis may be made electronically available to the public.

Statement of Contributions

The work presented in the thesis was performed by the author and several collaborators. The resulting publications and contributions of each collaborator are listed below in details.

The work in Chapter 2 has been published as Zhicheng Huang, Yu Zhao, Biwu Liu, Shaokang Guan, and Juewen Liu. Stronger Adsorption of Phosphorothioate DNA Oligonucleotides on Graphene Oxide by van der Waals Forces. ***Langmuir***, 2020, 36, 13708-13715. All of the experiments were performed by the first author. MD simulations were performed by Yu Zhao and Shaokang Guan. The manuscript was written by the first author and the corresponding author.

The work in Chapter 3 has been published as Zhicheng Huang, Biwu Liu and Juewen Liu. Mn^{2+}-Assisted DNA Oligonucleotide Adsorption on Ti_2C MXene Nanosheets. ***Langmuir***, 2019, 35, 9858-9866. All of the experiments were performed by the first author. Biwu Liu helped with the experimental design. The manuscript was written by Zhicheng Huang and Juewen Liu.

The work in Chapter 4 has been published as Zhicheng Huang, Biwu Liu and Juewen Liu. A High Local DNA Concentration for Nucleating a DNA/Fe Coordination Shell on Gold Nanoparticles. ***Chem. Commun.***, 2020, 56 (30), 4208-4211. All of the experiments were performed by the first author. Biwu Liu helped with the experimental design. The manuscript was written by the first author and the corresponding author.

The work in Chapter 5 has been published as Zhicheng Huang, Biwu Liu and Juewen Liu. Enhancing the Peroxidase-like Activity and Stability of Gold Nanoparticles by Coating a Partial Iron Phosphate Shell. ***Nanoscale***, 2020, 12, 22467-22472. Biwu Liu helped with the experimental design. All of the experiments were performed by the first author. The manuscript was written by Zhicheng Huang and Juewen Liu.

Abstract

DNA-modified nanomaterials have been applied in diverse areas such as biosensing, catalysis, drug delivery, and biomedical diagnostics. Metal ion mediated DNA conjugation is an important strategy for the construction of DNA/nanomaterials. The interactions between metal ions and DNA phosphate backbones were found critical for DNA adsorption. Most previously reported metal ion mediated DNA/nanomaterial conjugates focused on the role of metal ions for charge screening but ignored the potential formation of DNA/metal complexes, especially for multivalent ions. Since the report of DNA/Fe^{2+} coordination polymers (CPs), Fe^{2+} has become attractive in the modification of nanomaterials. One popular nanomaterial is gold nanoparticle (AuNP) which exhibits unique localized surface plasma resonance (LSPR) and enzyme-mimic catalytic activities. The primary focus of this thesis has two main parts: (a) the fundamental understandings of metal ion mediated adsorption of DNA oligonucleotides on 2D nanosheets such as graphene oxide (GO) and Ti_2C MXene; (b) the exploration of Fe^{2+} containing complexes and their applications in designing AuNP-based colorimetric sensors.

In Chapter 1, the relevant background knowledge of DNA oligonucleotides, DNA hybridization and melting, DNA-modified nanomaterials, nano-sized CPs, and AuNP-based colorimetric sensors are introduced. In addition, the motivation and objectives of my research are also described.

In Chapter 2, Na^+ and Mg^{2+} mediated the adsorptions of phosphorothioate (PS)-modified DNA (PS DNA) on GO are systematically studied. Using fluorescently labeled oligonucleotides as probes, all the tested PS DNA strands are adsorbed more strongly on GO compared to the normal DNA with phosphodiester linkages (called PO DNA) of the same sequence. The adsorption mechanism is probed by washing the adsorbed DNA with proteins, surfactants, and urea. Molecular dynamics simulations show that van der Waals forces are responsible for the tighter adsorption of PS DNA.

In Chapter 3, Mn^{2+}-mediated DNA adsorption on MXene is studied. Compared to other 2D materials such as GO, MoS_2, and WS_2, few fundamental studies were carried out on DNA adsorption by MXene. Due to its exfoliation and delamination process, the surface of MXene is abundant in −F, −OH, and −O– groups, rendering the surface negatively charged and repelling DNA. In previous studies, surface modification of MXene was performed to promote DNA adsorption. Herein, Mn^{2+} was discovered to promote DNA adsorption on unmodified Ti_2C MXene. Different from Ca^{2+} and Mg^{2+}, Mn^{2+} can invert the ζ-potential of the Ti_2C MXene from negative to positive. DNA mainly uses its phosphate backbone for adsorption, while its bases contribute significantly less.

In Chapter 4, DNA/Fe CPs were synthesized with Fe^{2+} by utilizing the high local DNA concentration of DNA/Au conjugates. Preparing DNA/Fe CP nanoparticles in solution requires a high

concentration of DNA. Taking advantage of the high local DNA density on the gold surface, the required DNA concentration decreased by 60-fold, and the thickness of the CP layer can be precisely controlled. Simultaneously, the good encapsulation property of CPs was utilized for loading a chemotherapeutic drug doxorubicin (DOX). In addition, a AuNP-aggregation-based colorimetric sensor was developed for phosphate detection, and the detection limit for phosphate was 0.78 mM.

In Chapter 5, The growth of a partial iron phosphate (FeP) shell with Fe^{2+} ions on citrate-capped AuNPs boosted the peroxidase-like activity of AuNPs by up to 20-fold. The FeP-enhanced activity was demonstrated on AuNPs of different sizes and on gold nanostars. When the FeP layer is thick enough to block the access to the Au/FeP interface, the activity was fully inhibited. Capping the remaining Au surface by thiol also inhibited the activity, suggesting that faster reactions occurred at the interface of Au and FeP. We also found that the adsorbed DNA strands on the AuNPs may disrupt the crystalline structures of the FeP shell. Thus, more channels may be available for accessing the Au/FeP interfaces. Moreover, sensitive detection of Fe^{2+} was achieved with a detection limit of 0.41 μM, while no other tested transition metal phosphates enhanced the peroxidase-like activity of AuNPs.

In Chapter 6, following the work in Chapter 4 and 5, a new AuNP-etching-based sensing platform was demonstrated. The goal was to convert the color of typical ELISA product, TMB+, to a color change of AuNPs to achieve more sensitive colorimetric detection. In previous work, the etching of gold nanomaterials (e.g., Au nanorods or AuNRs) usually need multiple steps and harsh conditions, which limits their applications. Herein, we developed a new colorimetric biosensing platform with urchin-like gold nanoparticles (AuNUs). The important roles of surfactant, pH and bromide were individually studied. Compared with AuNRs, the etching of AuNUs can happen under mild conditions in the existence of TMB^{+} at pH 6. With these understandings the AuNU-etching-based sensors were developed which can sensitively detect H_2O_2 with a detection limit of 80 nM (2.7 parts-per-billion).

Overall, my work found that metal ion mediated DNA adsorption on 2D nanomaterials GO, and Ti_2C MXene has been extensively studied, and the role of metal bridged interactions were deemed important. The growth of Fe^{2+} mediated DNA CPs and FeP on AuNPs was performed, which showed a great potential in drug loading and sensing. In particular, AuNP-based sensors for the detection of phosphate and Fe^{2+} ions were demonstrated. Finally, the fundamental process of etching of AuNUs has been carefully studied, and its application for the detection of H_2O_2 was also demonstrated.

Acknowledgements

I want to thank my supervisor, Prof. Juewen Liu, who constantly supports and guides me throughout my six-year graduate study. The learning and research experience under his supervision is quite rewarding and enjoyable for me. This is very important period in my life. Thank you professor for the invaluable advice, guidance and encouragement!

I would also like to thank my committee members and internal/external examiners: Dr. Jennifer I-Ling Chen, Dr. Shawn Wettig, Dr. Vivek Maheshwari, Dr. Thorsten Dieckmann and Dr. Shirley Tang for their time and helpful advice during my studies and throughout the preparation of this thesis. A special thanks to Dr. Vivek Maheshwari for being my committee member for both Master and PhD studies.

I greatly appreciate the help from all the current and former colleagues in the Liu lab: Dr. Po-Jung Jimmy Huang, Dr. Zijie Zhang, Dr. Yibo Liu, Dr. Runjhun Saran, Dr. Sona Jain, Dr. Feng Wang, Dr. Wang Li, Dr. Liu Wang, Dr. Jinyi Zhang, Tianmeng Yu, Dr. Dong Peng, Dr. Rong Wu, Dr. Wenhu Zhou, Xiaohan Zhang, Woohyun J. Moon, Mohamad Zandieh, Anand Lopez, Lei Chen, Yichen Zhao, and other members and visiting scholars. In particular, I would like to thank Dr. Biwu Liu, Yuqing Li, and Lingzi Ma for making our office a great place to share ideas and happiness. I would also like to thank Prof. Xuhui Sun for encouraging me to study abroad.

Also, a sincere thank you to my roommates Yuhan Huang, Fuwei Qiang, and Silu Chen for making the time enjoyable during the lockdown.

Finally, I would like to express my greatest gratitude to my family members. They always support and encourage me whenever I get into trouble and desperately need a hand. I wish they could always be happy and healthy.

Dedication

I would like to dedicate this thesis to my family for their encouragement and support.

Table of Contents

List of Figures

List of Tables

List of Abbreviations

A	Adenine
AgNP	Silver nanoparticle
AuNP	Gold nanoparticle
AuNR	Gold nanorod
AuNS	Gold nanostar
BSA	Bovine serum albumi
C	Cytosine
CaP	Calcium phosphate
CD	Circular dichroism
cDNA	Complementary DNA
CP	Coordination polymer
CTAB	Cetyltrimethylammonium bromide
CTAC	Cetyltrimethylammonium chloride
DOX	Doxorubicin
DTT	dithiothreitol
DNA	Deoxyribonucleic acid
dsDNA	Double-strand DNA
EDC	N-(3-dimethylaminopropyl)-N′-ethylcarbodiimide hydrochloride
EDTA	Ethylenediaminetetraacetic acid
ELISA	Enzyme-linked immunosorbent assay
FAM-DNA	6-carboxyfluorescein labeled DNA
FeP	Iron phosphate
FITC-BSA	Albumin-fluorescein isothiocyanate conjugate

G	Guanine
GO	Graphene oxide
GOx	Glucose oxidase
HEPES	4-(2-hydroxyethyl) piperazine-1-ethanesulfonate
HPR	Horseradish peroxidase
LSPR	Localized surface plasmon resonance
MCH	6-mercapto-1-hexanol
MD	Molecular dynamic
MIP	Molecularly imprinted polymer
PAA	Poly(acrylic acid)
PCR	Polymerase chain reaction
PME	Particle-mesh Ewald
PNA	Peptide nucleic acids
PO	Phosphodiester
Poly-A	Poly-adenine
Poly-C	Poly-cytosine
PS	Phosphorothioate
QD	Quantum dot
rDNA	Random DNA
RNA	Ribonucleic acid
SDS	Sodium dodecyl sulfate
SERS	surface-enhanced Raman scattering
SH-DNA	Thiolated DNA
SPR	Surface plasmon resonance

ssDNA	Single-strand DNA
T	Thymine
TECP	Tris(2-carboxyethyl) phosphate
TEM	Transmission electron microscopy
TEOS	Tetraethyl orthosilicate
Tm	Melting temperature
TMB	3,3’,5,5’-tetramethylbenzidine
UV-vis	Ultraviolet and visible
VDW	van der Waals

Chapter 1 Introduction

1.1 Introduction to DNA

Deoxyribonucleic acid (DNA) is an important molecule that acts as a carrier of genetic information in biology. With the study of DNA, a new field of molecular biology was developed in the last century. At the same time, significant progress was achieved in the analysis, synthesis, and sequence design of DNA. Especially, efficient chemical methods of synthesizing natural and modified DNA were developed. Based on these, in the early 1980s, Professor Nadrian Seeman hypothesized to use DNA in bio-nanotechnology theoretically.[1] Now, this rapidly developing field is known as DNA nanotechnology, where DNA is used as an intelligent biopolymer.[2] Aside from building nanoscale object using pure DNA, DNA oligonucleotides have also been functionalized to various nanomaterials, such as gold nanoparticles (AuNPs), graphene oxide (GO) and quantum dots (QDs), for biosensing, drug delivery and imaging applications. In the past decades, DNA has attracted significant interest for its potential applications in synthetic biology, supramolecular chemistry, and material sciences.[3-8]

1.1.1 The structure of DNA

1.1.1.1 Chemical components

A single-stranded DNA (ssDNA) is a polynucleotide composed of four nucleobases (adenine (A), thymine (T), cytosine (C), and guanine (G)) which are linked by a sugar-phosphate backbone (Figure 1.1A). The sugar-phosphate backbone is built with repeat end-to-end monophosphorylated deoxyribose sugars. Based on the chemical naming carbon atoms of the deoxyribose sugar, the two endings of a ssDNA are respectively named 5′-end and 3′-end. Two ssDNA strands with complementary sequences can pair with each other following the classical Watson-Crick base-pairing interactions (Figure 1.1B). This process is named as hybridization. In this resulting self-assembly double stranded structure, two strands run in opposite directions and the main interactions are the hydrogen bonds between A-T and C-G. Typically, the double helix structure has a width of 2 nm and a length of 3.4 nm for every ten base pairs (Figure 1.1C).

According to the handedness, length of the helix turn, number of base pairs per turn, and sizes of grooves, the tertiary arrangements of DNA structures in space are divided into B-DNA, A-DNA, and Z-DNA. In my research, the ssDNA and double-stranded DNA (dsDNA) whose lengths were shorter than 50-mer were used. Thus, the tertiary arrangement of DNA was not considered. These short DNA molecules are also known as oligonucleotides.

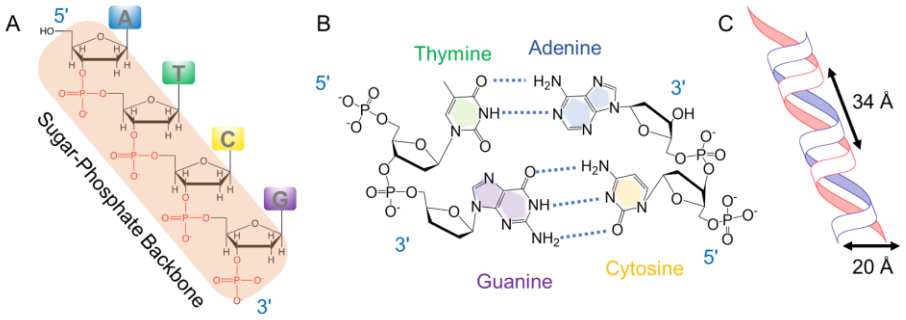

Figure 1.1 (A) The structure of a ssDNA strand. (B) The hydrogen bonds formed in the Watson-Crick base pairs. (C) The characteristic length scales for a dsDNA strand.

1.1.1.2 **Physicochemical properties of DNA**

The physicochemical properties of DNA are mainly from both the phosphate backbone and nucleobases. The nucleobases have characteristic ultraviolet light absorption at 260 nm, which can be utilized to determine the concentration of DNA. Another important property of DNA bases is their pK_a values (Figure 1.2).[9-10] For example, the protonation pK_a value of G is 2.1 and the deprotonation pK_a value of T is 9.9. This means that the charge of DNA nucleobases can be altered by tuning the pH environment. Since the pK_a value of the phosphate backbone is below 2, and all the nucleobases are charge neutral at neutral pH, DNA strands are negatively charged under physiological conditions.

Another important property of DNA is the melting temperature (T_m), which is defined by the temperature where 50% of the DNA is in the duplex form. In contrast to the hybridization, the process that breaks hydrogen bonds of base pairs and separates dsDNA into two ssDNA is called denaturation or melting. Due to the hydrophobicity of the nucleobases, the addition of hydrophobic molecules such as organic solvents, can decrease the T_m. The increasing salt concentration such as Na^+ and Mg^{2+} usually can increase the T_m by reducing the electrostatic repulsion force between two phosphate backbones. In dsDNA structures, the π-π stacking formed between the base pairs significantly increase the stability of double helix structure. The π-π stacking is also a critical force for DNA to bind to surfaces with the phenyl structures, such as GO.

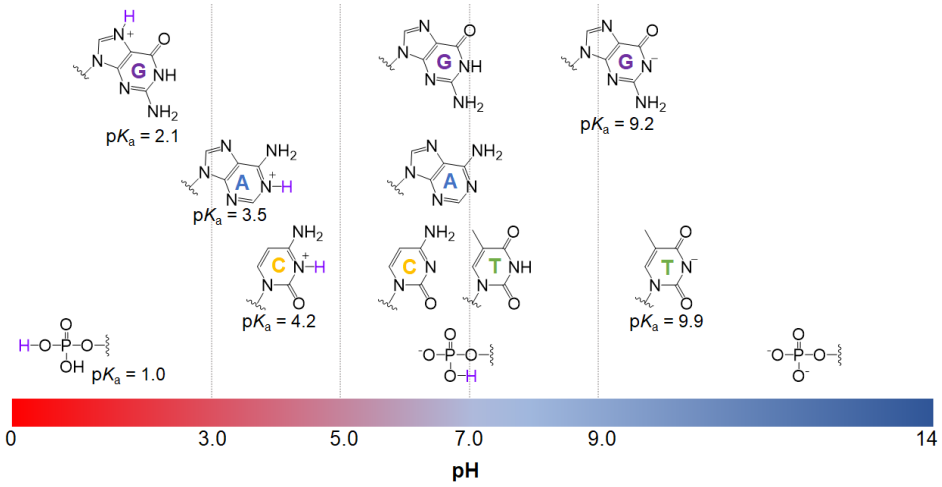

Figure 1.2 The structures of four DNA nucleobases and their pKa values. The protonation and deprotonation sites of DNA bases and phosphate are labelled in purple at pH environments.

1.1.1.3 **DNA-metal ion interactions**

Under physiological conditions, negatively charged DNA implies the binding of cations by electrostatic interactions. Generally, there are three types of interactions between cations and DNA.[11] In diffuse binding, with long-range nonspecific electrostatic interaction, the positions of cations on DNA are mainly dependent on the electrostatic potential (Figure 1.3 A). In nonspecific site binding, the interactions between hydrated cations and DNA are associated through hydrogen bindings of water molecules (Figure 1.3B). When one or more cation aqua ligands are replaced by the ligands on DNA, the site binding is specific (Figure 1.3C).

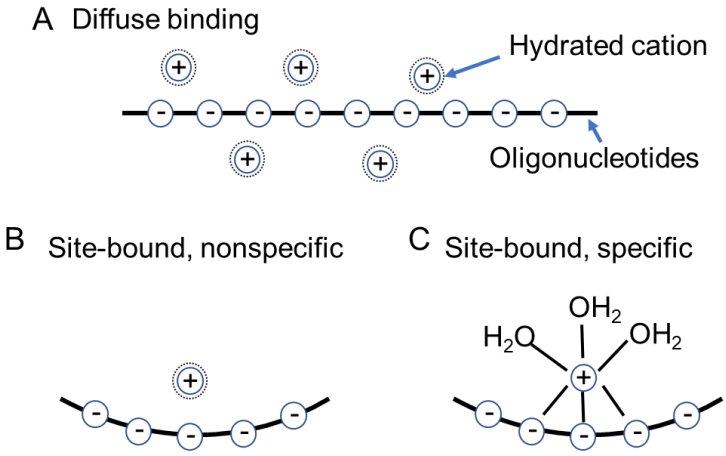

Figure 1.3 Three general interactions between metal ions and DNA: (A) diffuse binding; (B) nonspecific site-bound; and (C) specific site-bound.

The metal binding sites in DNA are mainly located on the phosphate backbone and nucleobases. More specifically, the N and O atoms in nucleobases and the O atoms in phosphate can provide electrons for the metal cations (Figure 1.4A).[12-13] For O atoms, based on the hard and soft characteristics for the metal ions, metal ions bind the O atoms in phosphates or nucleobases can be roughly predicted. For N atoms in nucleobases, the binding affinity with metal ions depends largely on the protonated and deprotonated states. In general, for transition metals, the affinities follow the order of N7 (G) > N3 (C) > N7 (A) > N1 (A) > N3 (A, T).[13] In addition, some DNA-metal bindings which involve more than one nucleobase also have been revealed (Figure 1.4B-D).

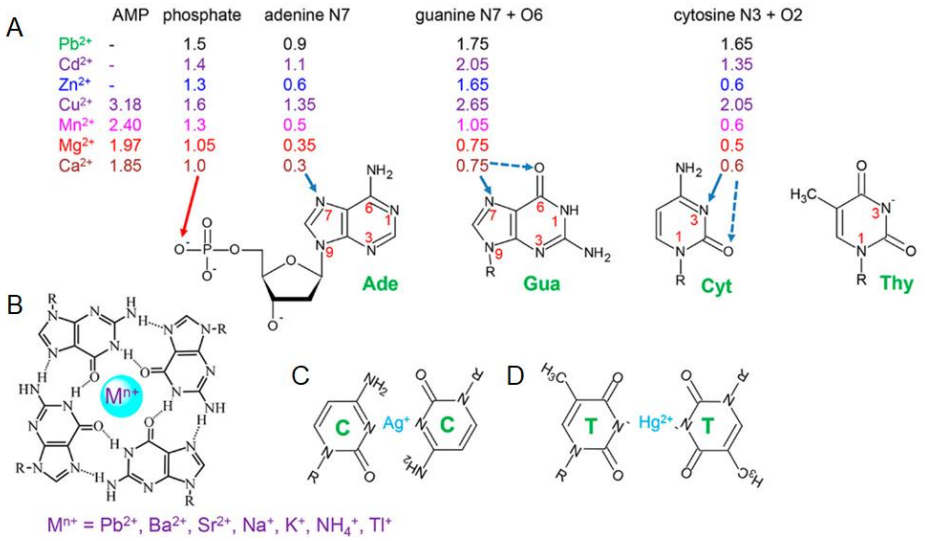

Figure 1.4 (A) The metal binding sites in DNA phosphate backbone and nucleobases. The values of the log of K_a are labelled. The interactions between (B) metal ions/G-quadraplex DNA, (C) Ag^+/cytosine, and (D) Hg^{2+}/thymine. Figures adapted with permission from ref ([13]). Copyright © 2017 American Chemical Society.

The DNA-metal ion interactions have significant effects on the properties of DNA. As mentioned above, increasing salt concentration usually stabilizes DNA duplex. However, for the metal ions, which can bind nucleobases strongly, may denature duplex DNA by disrupting inter-nucleobase hydrogen bonds. For example, a few μM Pb^{2+} ions can dramatically decrease the T_m of DNA since Pb^{2+} binds both guanine and cytosine stronger than phosphate.[14] The study of these interactions motivated the adsorption of DNA on inorganic nanomaterials and the growth of metal-containing nanomaterials on DNA templates.[8, 15-16]

1.1.2 **Chemically modified DNA**

Thanks to the great advancement in synthetic organic chemistry of DNA, DNA modifications are realized at all the three parts (phosphate, sugar, and nucleobases). More than 100 different types of functional groups can be easily obtained such as phosphorylation, alkane spacers, fluorophores, dark quenchers, thiols, and attachment linkers. These modified-DNA molecules have shown great potential applications in chemical biology, sensing, and drug delivering.[17-20] A few modifications used in this thesis are introduced below.

1.1.2.1 **Phosphorothioate DNA**

Phosphorothioate (PS) modification replaces one of the non-bridging oxygen atoms by sulfur in the DNA phosphate backbone (Figure 1.5A). PS-modified nucleic acids have useful properties for various applications. First, such single atom substitution only slightly perturbs the structure of DNA, and Watson-Crick base pairing can still take place, retaining the programmability of DNA.[21] Second, PS modifications are cost-effective. From commercial sources, each PS just adds a few dollars to the synthesis. For comparison, modified bases typically cost more than $100 each. Third, PS increases the stability of DNA against degradation by nucleases, which was one of the original motivations of developing it for antisense applications. Nevertheless, PS modification also has its own complications. For example, each PS modification results in a chiral phosphorus center, and most synthesis methods yield a racemic mixture of R and S diastereomers. It is not easy to obtain stereo pure molecules, especially for those with multiple PS modifications.

With a sulfur atom introduced to the phosphate backbone, many interesting applications have been developed. Most of these are related to the metal-binding property of the sulfur. The DNA sequences reviewed here sometimes contain two main blocks: a PS block (for metal binding), and a PO block (for molecular recognition), which are named diblock DNA (Figure 1.5B). Compared with normal DNA, PS DNA is easier to adsorb onto thiophilic materials (e.g. Cd containing QDs, AuNPs, and silver nanoparticles or AgNPs). Thus, PS DNA has been widely used in assembling these nanoparticles to form nanostructures.[22-24]

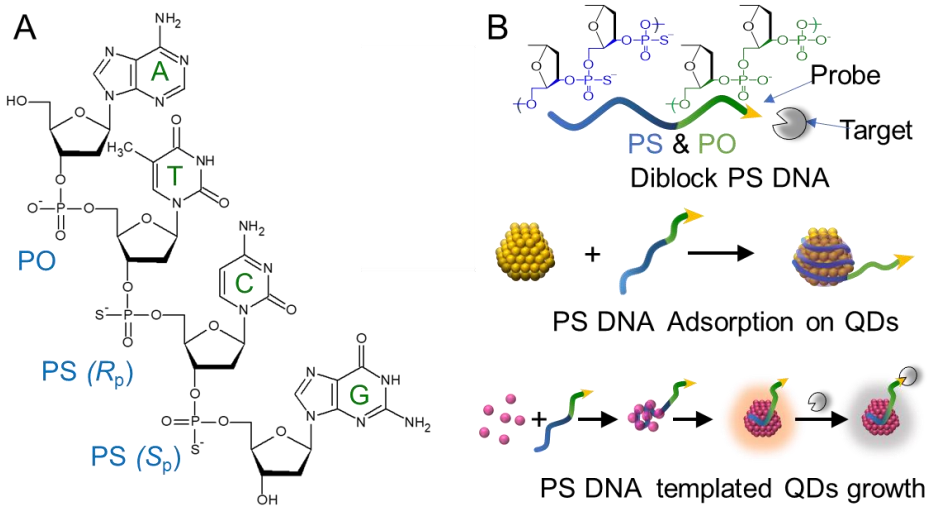

Figure 1.5 (A) The structures of a 4-mer ATCG DNA with a normal phosphodiester (PO), a PS (Rp), and a PS (Sp) linkage. (B) Schematic depicting of a DNA sequence with two blocks (PS and PO). Compared with PO block, PS block has much stronger interactions with Cd-containing QDs.

1.1.2.2 **Thiolated DNA**

Thiol modifications can be introduced at either the 5′-end or the 3′-end during the solid-phase phosphoramidite oligonucleotide synthesis (Figure 1.6A and B). Thiolated DNA (SH-DNA) can be further reacted with various groups including α,β-unsaturated ketone, maleimide, and cysteines. These features allow SH-DNA sequences to be covalently linked to a wide range of molecules and materials (e.g. proteins and AuNPs).[25-26]

In this research, SH-DNA were mainly used in gold surface modification due to the strong thiol-gold interaction. Commercial SH-DNA sample always come with a small alkanethiol protective cap formed via a disulfide bond. To remove the protection groups, reduce agents such as dithiothreitol (DTT) and Tris(2-carboxyethyl) phosphate (TECP) are usually used for pretreatment (Figure 1.6C). Our previous study showed that the addition of DTT/TCEP is not essential for SH-DNA adsorption on AuNPs,[27] but it is essential for reacting with organic molecules such as maleimide.

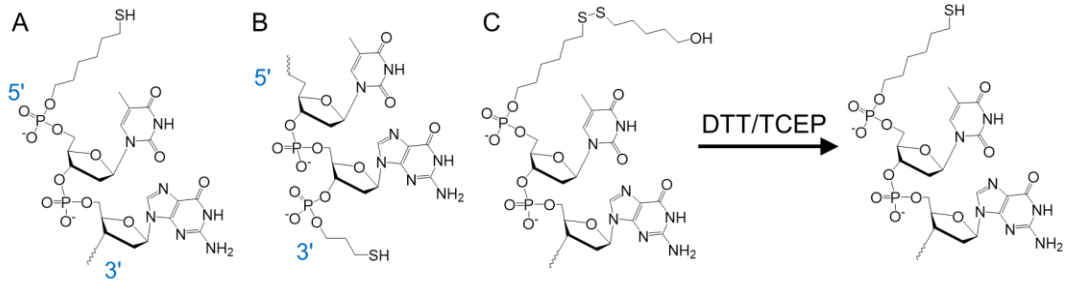

Figure 1.6 The structures of thiolated DNA with the thiol group at 5′-end (A), and 3′-end (B). (C) Scheme showing the process of reducing disulfide bonds in a commercial thiolated DNA.

1.1.2.3 Fluorophore-labelled DNA

For fluorophore-labelled DNA, one or more fluorescent dye molecules can be attached on a DNA strand. Trace amount of fluorescence labelled DNA can be monitored by fluorescence spectroscopy in solution, or by fluorescence microscopy on suitable solid surfaces. Fluorophore labelled DNA is quite powerful in studying the interaction between nanomaterials and DNA since many nanomaterials are good fluorescence quenchers. Both fluorescence quenching and recovering can be utilized in developing various functional DNA/nanomaterial based biosensors.[28]

1.1.3 DNA nanotechnology

1.1.3.1 Functional DNA (DNA aptamers and DNAzymes)

The well-known biological function of DNA is to carry genetic information. Since the early 1990s, DNA with chemical functions such as molecular binding and catalysis have been reported. Functional DNA molecules include two main types: aptamers and DNAzymes. DNA aptamers are ssDNA which can bind analytes specifically. Since the report of the first DNA aptamer for thrombin in 1992, a number of aptamers for various targets (e.g. metal ions, small molecules and proteins) have been isolated.[29] DNAzymes acting as enzyme mimics are inspired by the discovery of ribozymes, and they are obtained from a ssDNA library by in vitro selection. These functional DNA molecules are promising to design biosensors by combining them and nanomaterials.[20, 30-31]

1.1.3.2 DNA nanostructures

Based on Watson-Crick base pairing rule, DNA molecules could be programmed to form nanoscale or microscale structures. Over the past decades, this is widely used in the bottom-up fabrication of well-defined nanostructures. One impressive example is DNA origami. A classic DNA origami involves a long single-stranded scaffold DNA and a number of short DNA strands (called staples). After annealing treatment, the long scaffold DNA is folded by the base pairs formed with the short staple DNA. As a result,

large-scaled DNA origami structures are obtained with more scaffold and staple DNA (Figure 1.7A).[32] Since the first four-way DNA junction reported by Seeman et al., various DNA origami structures from 1D to 3D can be synthesized (Figure 1.7B).[33-34] Besides the DNA origami, DNA can also be used to program the assembly of nanoparticles.[35] Herein, a typical case about DNA-directed assembly of AuNPs for detecting adenosine molecules is recited (Figure 1.7C).[36] The aggregation of AuNPs are assembled by the hybridization between the linker DNA and the other two sequences that respectively modified on different AuNPs, leading to a blue solution. Since a segment of the sequence of the linker DNA is the adenosine aptamer, with the existence of adenosine molecules, the linker DNA bound adenosine instead of directing the aggregation of AuNPs. As a result, a red color is obtained.

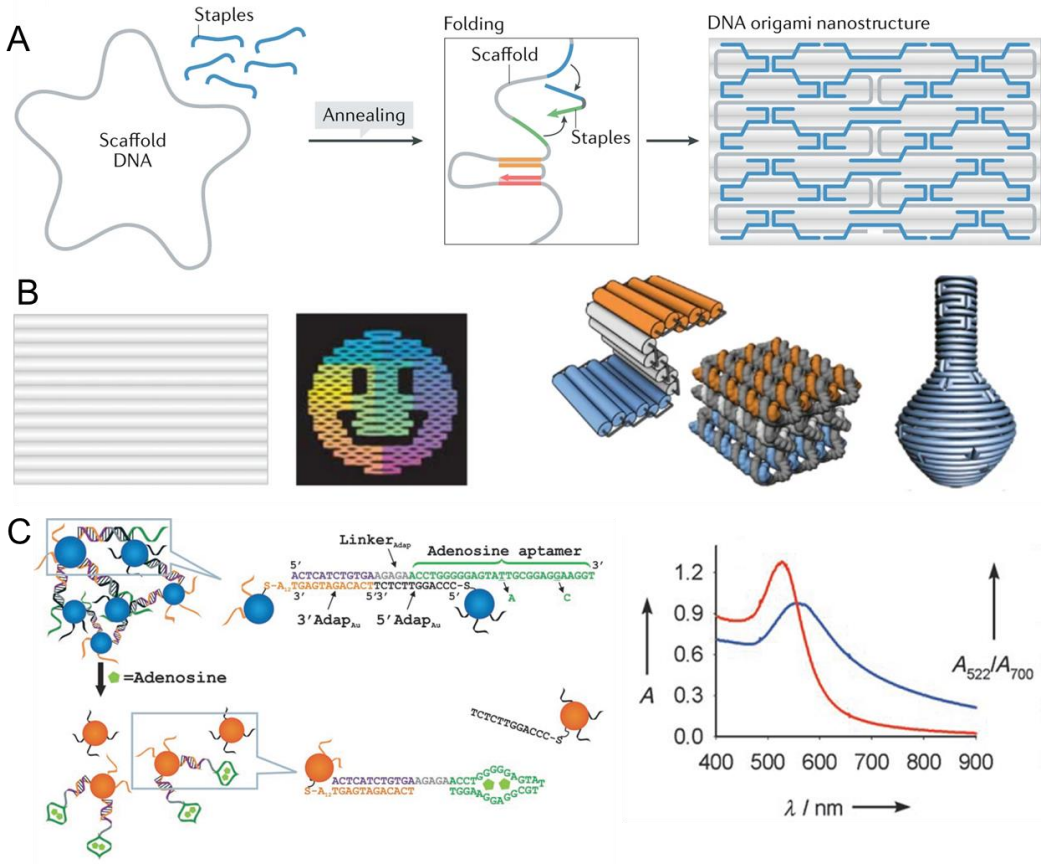

Figure 1.7 (A) Schematic depicting the principles of classic DNA origami. (B) 2D and 3D DNA origami structures. (C) DNA base-paring directed assembly of AuNPs which act as colorimetric sensors for adenosine detection. Figures A and B adapted with permission from ref ([34]). Copyright © 2021, Springer Nature Limited. Figure C adapted with permission from ref ([36]). Copyright © 2006 WILEY-VCH.

1.2 DNA-Nanomaterial Complexes in Nanotechnology

Nanomaterials possess many unique properties, such as antibiotic property of graphene oxide (GO), molecular adsorption property of MXene, and localized surface plasmon effect of AuNPs. Interfacing DNA with these nanomaterials has resulted in various hybrids widely used in chemistry, physics, material science, and medicine.[37-40] In this section, I introduce the properties, applications, and synthetic strategies of three DNA/nanomaterial complexes: DNA/GO, DNA/MXene, and DNA/AuNPs.

1.2.1 DNA-modified GO

1.2.1.1 Introduction to GO

As the most studied two-dimensional nanomaterial, graphene is comprised of thin layers of sp^2-bonded carbon atoms. GO which is usually obtained from the exfoliation of graphite has a single atomic layer with rich oxygen-containing functional groups on its surface.[41] The synthetic methodology of GO contains two main steps: oxidation and exfoliation (Figure 1.8). Due to these oxygen groups, GO has a better dispersibility in water than graphene.[42-43] Therefore, GO is often used for DNA adsorption. DNA-modified GO has found numerous applications in sensing, imaging, therapeutics, diagnostics, and drug delivery.[39, 44-45]

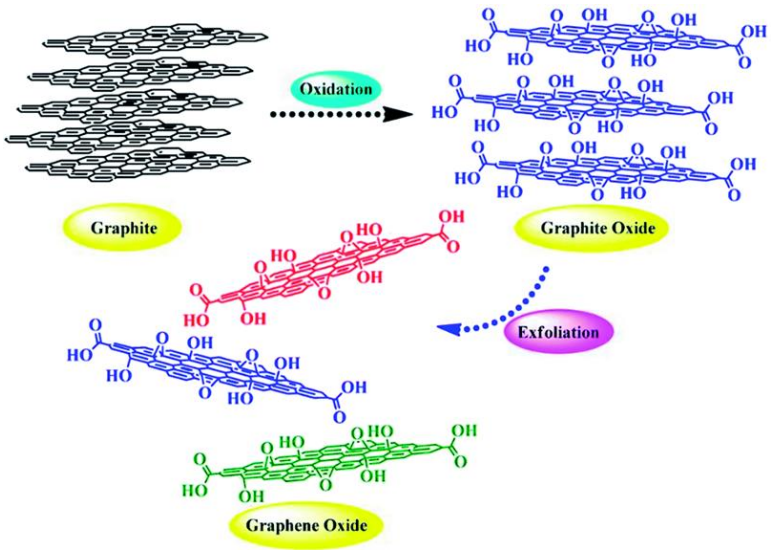

Figure 1.8 Schematic synthesis of graphene oxide. Reproduced with permission from ref ([41]) with open access.

1.2.1.2 The interactions between GO and DNA

The interactions between GO and DNA can be divided into two main types: non-covalent and covalent bindings. Under physiological environment, both DNA and GO are negatively charged. For non-

covalent modification, acidic conditions or addition of salts (e.g., NaCl) can promote the physisorption of DNA on GO.[46-47] Due to the negatively charged phosphate backbone, π-π stacking interactions between the nucleobases and GO's hydrophobic domains is believed to be critical for DNA adsorption. This can be used to explain the different binding performance of physisorption between ssDNA and dsDNA on GO (Figure 1.9A).[48] For dsDNA, all the nucleobases are burried by the phosphate backbone. As a result, ssDNA can be desorbed from GO by the complementary DNA (cDNA) when dsDNA is formed.[49] To increase the physisorption affinities and control the arrangements of DNA, a diblock DNA with a high surface affinity poly-cytosine (poly-C) sequence, serving as anchoring block, is widely used (Figure 1.9B). With increasing DNA concentration, the poly-C block gradually displaces the other probe block, leading to the upright conformation of the other block.[50] Therefore, cDNA can hybridize with the probe block and attach to GO. Besides these non-covalent binding, amino-modified DNA can also be covalently conjugated to GO by using N-(3-dimethylaminopropyl)-N′-ethylcarbodiimide hydrochloride (EDC) (Figrue 1.9C).[51] For the covalent modification, the adsorption of nucleobases of amino-modified DNA on GO cannot be avoided.

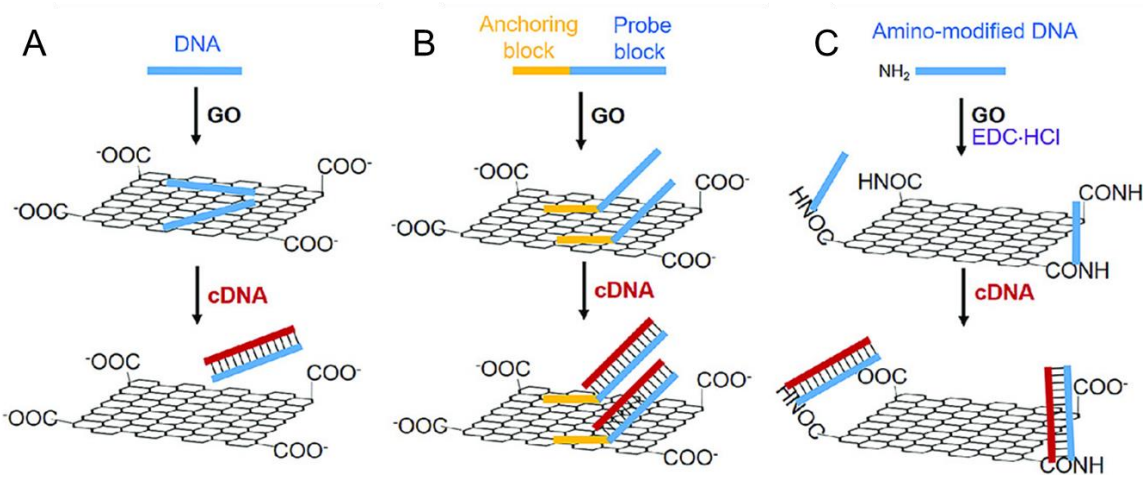

Figure 1.9 Schemes of (A) physisorption of ssDNA and dsDNA, and (B) a diblock DNA containing a poly-C anchoring block for adsorption on GO, and (C) covalently modification of amino-modified DNA on GO. Reproduced with permission from ref ([48]) with open access.

GO has unoxidized benzene rings (hydrophobic regions) and oxidized aliphatic rings (hydrophilic region), and the degree of oxidation determines the sizes of these regions. The detailed studies of the DNA adsorption on these two domains are important in illuminating the adsorption mechanisms. Both simulation studies and experimental results reveal that the GO with higher degree of oxidation can accommodate more DNA strands.[52-54] An interesting finding is that temperature can significantly affect the DNA adsorption

areas on GO.[55] Simply, heating can promote DNA adsorption on hydrophobic regions while freezing help DNA adsorption on hydrophilic regions (Figure 1.10).

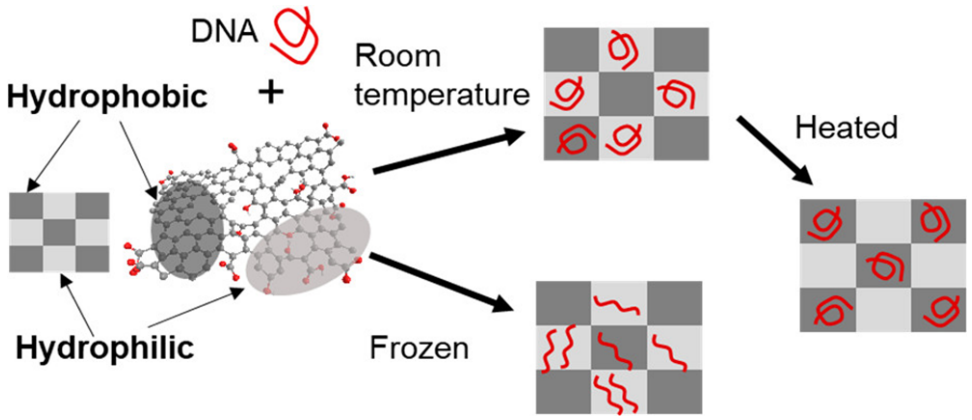

Figure 1.10 Schematic digram for the DNA adsorption on the hydrophobic and hydrophilic areas of GO regulated by temperature. Reproduced with permission from ref ([55]). Copyright © 2020 American Chemical Society.

1.2.1.3 **DNA-GO biosensors**

DNA/GO complexes are widely employed as novel biosensors for the detection of DNA, proteins, and other biomacromolecules.[56-58] Due to the fascinating light-absorption capability and electron transfer fluorescence-quenching properties of GO, most of these biosensors are designed with fluorescent probe DNA. In a typical sensor model, a fluorescent probe DNA is adsorbed on GO by physisorption leading to fluorescence quenching (Figure 1.11).[49] Then, a recovery of fluorescence is obtained by the addition of target reagents (e.g., cDNA) which can release the pre-adsorbed probe DNA from GO surface.

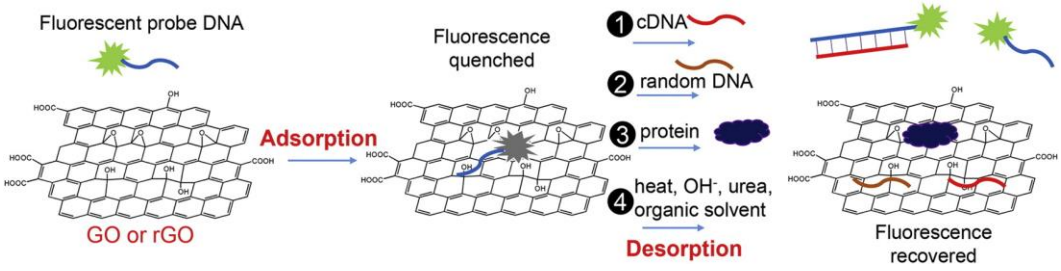

Figure 1.11 The graphical representation of fluorescence-based DNA/GO sensors by desorption. Reproduced with permission from ref ([49]). Copyright © 2016 Elsevier Ltd.

1.2.2 **DNA-modified Ti_2C MXene**

1.2.2.1 **Introduction to MXene**

MXene is a new group of two-dimensional (2D) nanomaterials containing transition metal and carbide/nitride. MXene sheets are usually exfoliated from MAX phases, where M is an early transition metal (e.g., Ti, V, and Nb), A is an A-group element such as Al, and X is carbide/nitride. Over 100 known MAX phases can be categorized by the numbers of the layers of M and X (Figure 1.12).[37-38, 59]

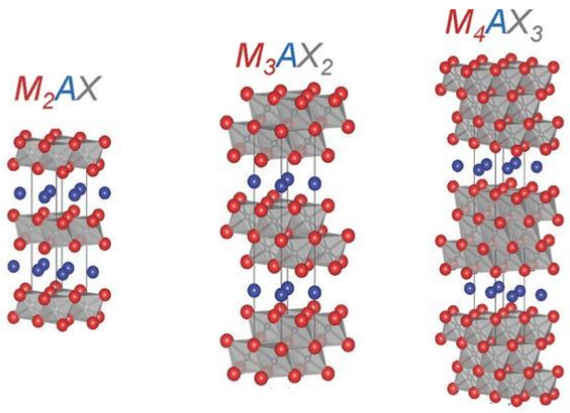

Figure 1.12 2D ball-and-stick models for M_2AX, M_3AX_2, and M_4AX_3-based MAXs. Reproduced with permission from ref ([37]). Copyright © 2013 WILEY-VCH Verlag GmbH & Co.

The strong bonds between M and X have a mixed covalent/metallic/ionic character, and the M-A bonds also have strong metallic interactions.[60-61] Therefore, in comparison with other 2D materials (e.g., MoS_2) with slidable layers, a strong acid is usually used to break the M-A bonds. The synthesis of MXene contains two main steps: etching and delamination.[62-63] Herein, the synthesis of Ti_3C_2 MXene is presented as an example (Figure 1.13A).[64] First, Al layers of the MAX phase are etched in HF. While A layers are removed, the exposed M surfaces are covered with terminal groups (-OH, -F, -O, etc.). Second, the loosely bonded multi-layered MXene sheets are delaminated to generate single-layered MXene sheets (Figure 1.13B), where the element maps also reflect the rich -F, -O, -OH groups on the MXene surface. These functional terminal groups make MXene surfaces highly negatively charged, which would inhibit their interactions with DNA.[38, 65]

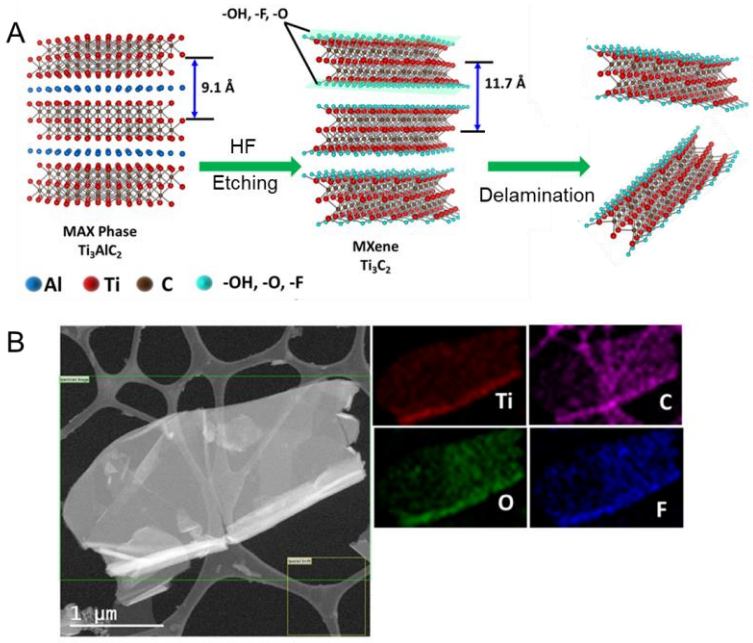

Figure 1.13 (A) Schematic synthesis of Ti_3C_2 MXene from Ti_3AlC_2 MAX by etching and delamination. (B) A TEM image of a single layer Ti_3C_2 MXene sheet and corresponding element maps. Figures adapted with permission from ref ([64]). Copyright © 2018 Elsevier B.V.

1.2.2.2 **The interactions between MXene and DNA**

The highly negatively charged surfaces limits the DNA adsorption on MXene sheets. The strategy of adding Na^+ or Mg^{2+}, which is widely used for DNA adsorption on GO and MoS_2, is no more effective for MXenes.[66] As showed in Figure 1.14, researchers utilize the surface modifications to improve the DNA loading capacities and increase the colloidal stabilities of MXene sheets in aqueous solutions. By now, surface coatings have been made using both polymers and inorganic materials. For polymers, a successful example is poly(acrylic acid) (PAA). An amino-modified DNA can be covalently linked to PAA chains by EDC/NHS coupling reactions.[67] For inorganic materials, both *in situ* reduction growth or post-adsorption of AuNPs are very popular.[68-69] After AuNP coating, SH-DNA or non-SH-DNA can be easily modified on the AuNPs, which indirectly functionalized the MXene sheets.

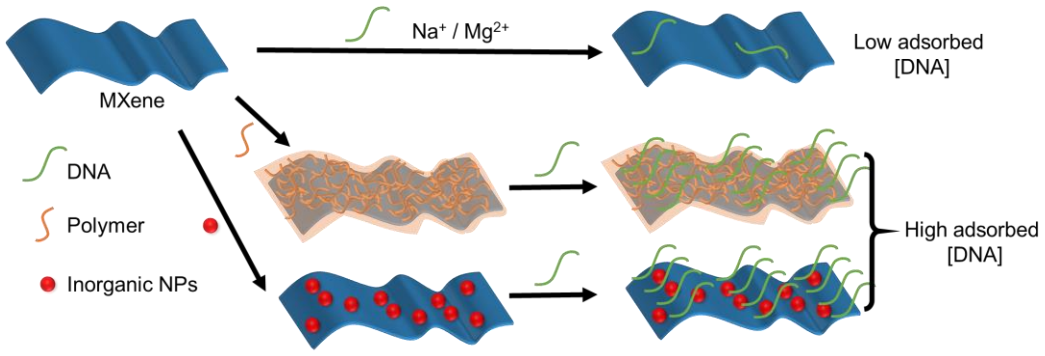

Figure 1.14 Schematics of DNA modifications on MXenes by the addition of salts (Na^+ or Mg^{2+}) and surface modifications. DNA adsorption density on MXene surfaces is much lower than that on polymer/nanoparticle-modified MXene surfaces.

1.2.3 **DNA-modified AuNPs**

1.2.3.1 **Introduction to DNA/AuNPs**

AuNPs have generated widespread interest because of their distinct physical and chemical properties. One of these fascinating properties is the localized surface plasmon resonance (LSPR), allowing extremely efficient absorption of light of certain wavelengths. The LSPR peak of AuNPs is dependent on surface morphology, size, and adsorbed ligand.[70-71] Therefore, many AuNP-based colorimetric sensors have been developed.[40, 72]

DNA-functionalized AuNPs (Au@DNA NPs) are very important agents in a broad range of applications from biosensing, DNA-directed assembly to drug delivery.[73] When DNA oligonucleotides are densely packed on AuNPs, in comparison with liner nucleic acids, such conjugates feature unique physicochemical properties such as sharper melting transitions, stronger binding to complementary DNA, and more efficient cellular uptake.[74] DNA modification also significantly changes the properties of AuNPs. For example, with DNA modification, the colloidal stability of AuNPs is dramatically improved in NaCl solution (Figure 1.15B).

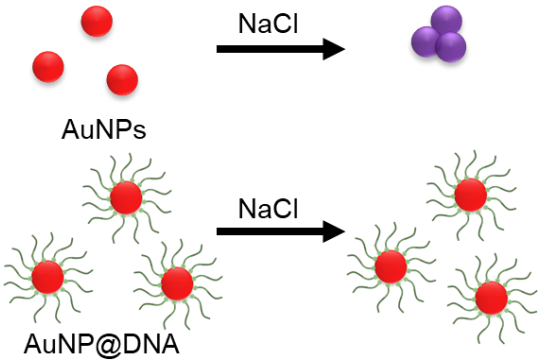

Figure 1.15 Schematics of DNA adsorption improves the colloidal stability of AuNPs in a NaCl solution.

1.2.3.2 The interactions between AuNP and DNA

For unmodified DNA, DNA adsorption is realized by the interactions between DNA nucleobases and AuNPs (Figure 1.16A). In many cases, the relative affinities of DNA nucleobases and gold surface follow the trend A > C > G > T.[9, 75] Such affinity difference can be amplified by using homo-DNA oligonucleotides (comprised of the same nucleobase).[76] Since poly-adenine (poly-A) DNA has the strongest affinity, the number of adsorbed DNA strands on each AuNP can be programmed by varying the lengths of poly-A DNA.[5]

Besides non-modified DNA, to get a high DNA adsorption density on AuNPs, SH-DNA is usually used. Due to the strong affinity between thiol and gold, unintended adsorption of nucleobases on gold surface can be gradually displaced by terminal thiol groups as the density of DNA is increased.[77] This replacement process forces DNA to be in an upright conformation. As a result, for each DNA sequence, its footprint area in stand-up adsorption model is much smaller than that in a lengthwise model (Figure 1.16B). Therefore, the upright model is essential for high DNA adsorption density. By now, the record-high DNA density reached nearly 400 strands on each 15 nm AuNP.[78]

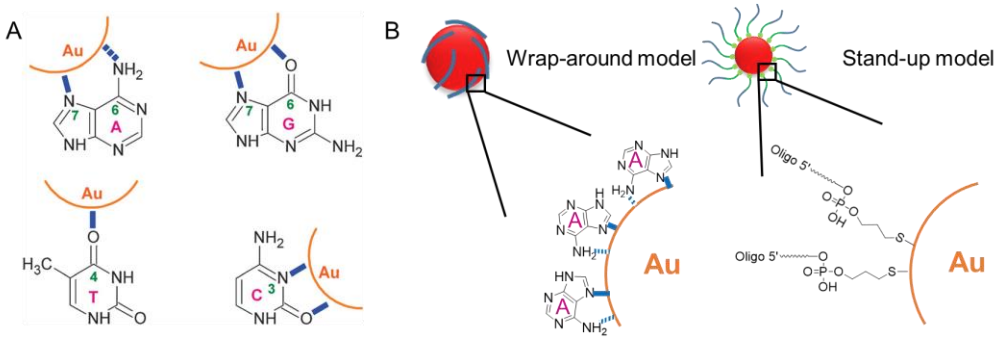

Figure 1.16 (A) The binding sites of four DNA nucleobases on gold surface. (B) Two different adsorption models for the thiolated and non-thiolated DNA adsorption on AuNPs. Figure A adapted with permission from ref ([9]). Copyright © 2012 Royal Society of Chemistry.

The function of Au@DNA NP has a lot to do with its preparation, where a SH-DNA is typically used. Despite the high affinity between thiol and gold, this conjugation reaction is complicated due to the charge repulsion between DNA and AuNPs, as well as the colloidal stability of the AuNPs.[79] The classic conjugation method is called salt-aging, in which NaCl is stepwise added to screen the charge repulsion and carefully avoid AuNP aggregation. The higher the final concentration of NaCl reached, the higher DNA loadings on AuNPs.[74] To maximize DNA loadings, the salt-aging process takes more than a day. To shorten the aging time, surfactants were used to stabilize AuNPs, which allowed DNA loading to finish within a few hours. In 2012, our group found that at pH 3, the reaction could be completed in minutes.[80] Later, a freezing-based method was developed for DNA attachment. Without additional reagents added, AuNP@DNA was prepared after freezing and thawing AuNP/DNA mixtures (Figure 1.17).[25] The high DNA adsorption densities were resulted from the stretching and alignment of DNA sequences under freezing.[81]

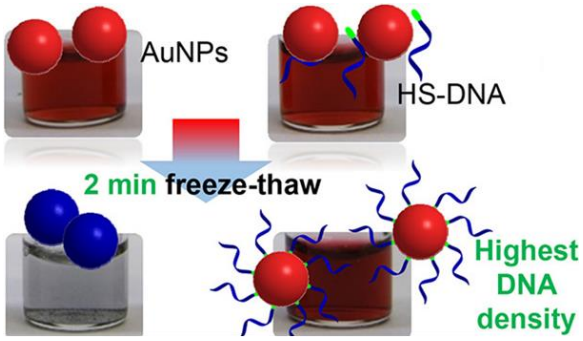

Figure 1.17 A Scheme of preparing Au@DNA NPs by the freezing method.[25] Figure adapted with permission from ref ([25]). Copyright © 2017 American Chemical Society.

1.3 Nanosized Coordination Polymers

Coordination-driven self-assembly of metal ions and organic molecules is an important method of producing coordination polymers (CPs). Extensively studied metal-organic frameworks can be considered as a type of crystalline CP, while CPs can also be amorphous.[82] These CPs have a wide range of applications in sensing, catalysis, drug delivery, and gas storage.[12, 83-87] In this section, CPs formed between metal ions and DNA nucleobases, nucleotides and DNA oligonucleotides are introduced.

1.3.1 DNA/metal CPs

1.3.1.1 DNA precipitation by metal ions

Polyanionic DNA sequences are capable of coordinating with a large number of metal ions. For a long time, CPs were only observed by using nucleobase/nucleosides/nucleotides as ligand, while the

formation of well-defined CPs with DNA oligonucleotides has been challenging.[88] It has now been observed that both relatively high nucleobase and metal ion concentrations (millimolar levels) are necessary.[89-90] In addition, metal/nucleobases bindings in grooves are also non-negligible. For example, Al^{3+} can precipitate calf thymus DNA completely at pH 6 to 7 through groove binding.[91] For long genomic DNA, the process of generating solid DNA/metal complexes is also known as "precipitation".[92] However, these metal-induced DNA precipitates are usually not nanosized, which limits their applications such as in drug delivery.

1.3.1.2 **Nucleotides/nucleosides for metal coordination**

Nucleotides and nucleosides are not only monomeric units of DNA biopolymers but also good ligands for constructing CPs with metal ions (Figure 1.18A). Different from DNA precipitates, stable and uniform nanosized coordination complex particles can be obtained with nucleotides/nucleobases.[88, 90] In addition, each type of nucleotide/nucleobase has its own metal binding preference. For example, adenine has a high affinity for gold binding.[93] Of course, a metal ion can be chelated by two or more than two sites in phosphates and nucleobases (Figure 1.18B). In the past decades, many useful and powerful nucleotides/nucleobases-based CPs have been developed and been applied in sensing, encapsulation, and drug delivery.[94-97]

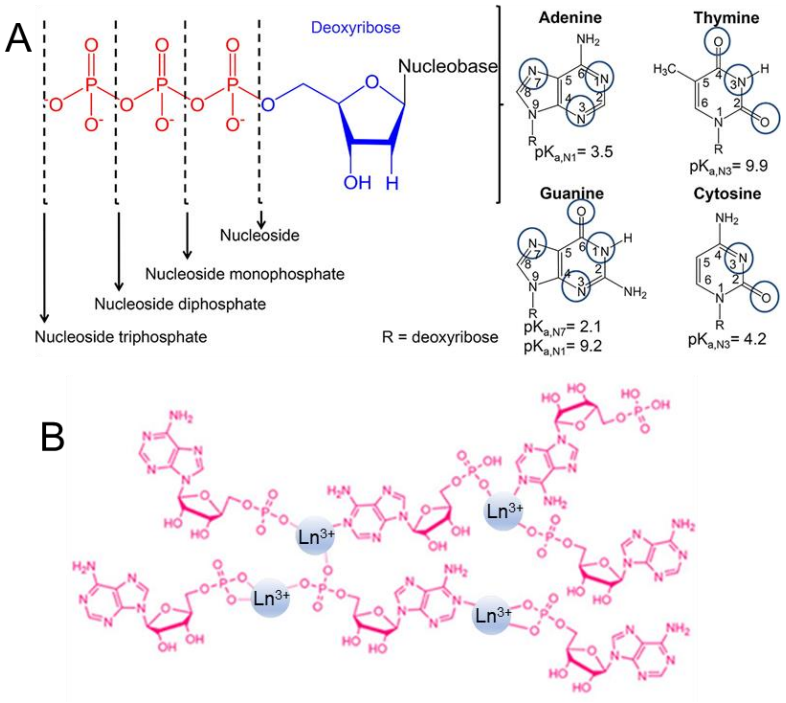

Figure 1.18 (A) Chemical structure of four nucleobases, nucleosides, and nucleotides. The potential sites for metal coordination and the pK_a values of four nucleobases were also labelled. (B) A scheme for the self-assembly of AMP and Ln^{3+}. Figure A adapted with permission from ref([88]). Copyright © 2019 Elsevier B.V.

1.3.1.3 **DNA/Fe CPs**

DNA/Fe CPs were first reported by Li's group in 2019.[89] This newly developed strategy of large-scale production of DNA/Fe CPs is achieved simply by one-pot reaction of DNA oligonucleotides and Fe^{2+} (Figure 1.19). Another feature of this technique is the small amount of DNA oligonucleotides needed, which dramatically lowers its cost. For example, the lowest concentration of 20-mer DNA oligonucleotides required to form stable DNA/Fe CPs can reach 25 μM. These DNA/Fe CPs showed excellent stability and great promises in drug delivery and bio-imaging.[87, 98] In comparison with Fe-nucleotide/nucleobase CPs, DNA/Fe CPs have inherent advantages in gene delivery. Both functional DNA and oligonucleotide drugs can be directly used to synthesize DNA/Fe CPs, and no other chemicals are needed. In addition, chemotherapeutic drug doxorubicin (DOX) molecules can also be co-assembled in DNA/Fe CPs.[98]

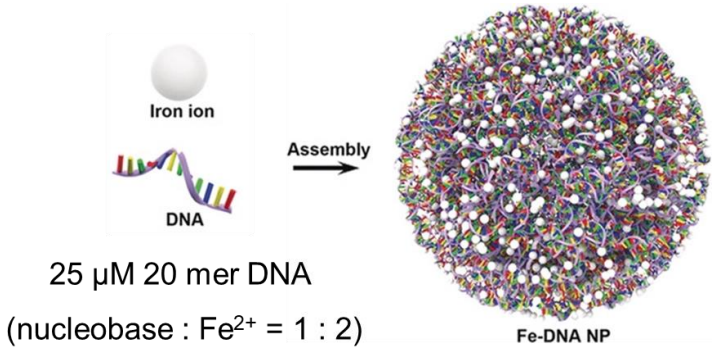

Figure 1.19 Schematic of coordination-driven self-assembly of Fe^{2+}, DOX molecules, and DNA oligonucleotides. Figure adapted with permission from ref ([89]). Copyright © 2006 WILEY-VCH Verlag GmbH & Co.

1.3.2 **Applications of metal/nucleotides, DNA/Fe CPs and metal phosphates as coatings**

The metal/nucleotides coatings on various nano-sized cores are powerful synthetic strategies for constructing abundant nanomaterials. One of the most straightforward advantages is that these coatings can improve the stabilities of soft cores. For example, negatively charged DOPS liposomes are so weak that cryo-TEM is required for morphology characterizations. After coating with Gd^{3+}/AMP CPs, the TEM images of DOPS liposomes can be easily obtained by normal TEM (Figure 1.20A).[99] In addition, the metal/nucleotides CP coatings may also bring new properties. Liang and coworkers demonstrated that the growth of Fe^{3+}/AMP shells on magnetite nanoparticles (Fe_3O_4NPs) could improve the peroxidase-like activity of the Fe_3O_4 core (Figure 1.20B).[100] Since the synthesis of DNA/Fe CPs was newly developed, there is still a lack of study, such as the growth of DNA/Fe CPs on different surfaces.

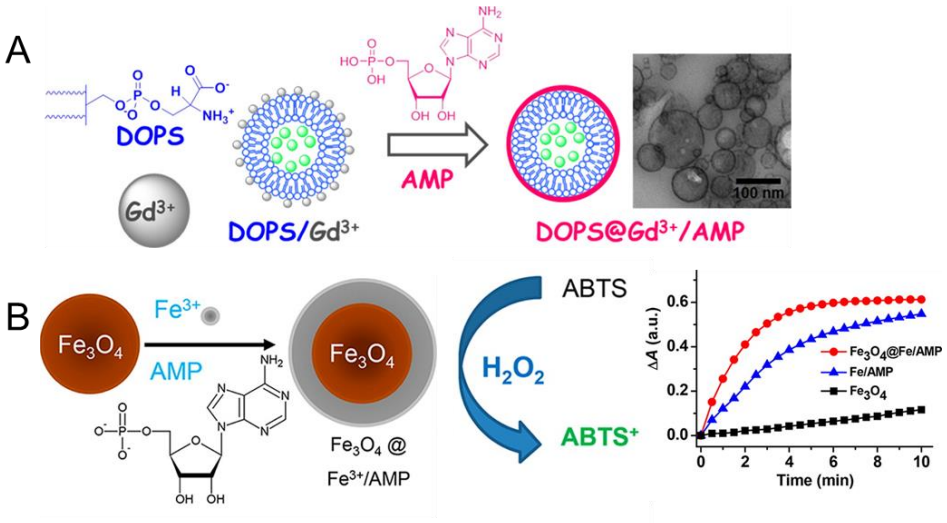

Figure 1.20 Schematic illustrations of (A) Gd^{3+}/AMP CPs on DOPS liposomes and (B) Fe^{3+}/AMP CPs on Fe_3O_4 NP. The Fe^{3+}/AMP shell on Fe_3O_4 NP can improve its peroxidase-like activity. Figure A adapted with permission from ref ([99]). Copyright © 2019 American Chemical Society. Figure B adapted with permission from ref ([100]). Copyright © 2016 American Chemical Society.

In addition to the CPs formed with DNA or nucleotides, the strong interactions between DNA phosphate backbone and metal ions are also very interesting. In terms of coatings, many interesting results may be generated when the CPs were simply generated by metal phosphates or a mixture of DNA and metal phosphates.[101-103] By now, the most well-studied nanoscale metal phosphate is calcium phosphate (CaP), since CaP is the most abundant biomineral in hard tissues.[104] CaP plays important roles in both metallizations of DNA and AuNPs surface coatings. In 2020, Fan et al. mineralized self-assembled DNA frameworks by CaP with precision and versatility.[105] After mineralization, DNA frameworks can keep their structures under harsh conditions. In this work, they revealed that amorphous CaP NPs were first formed near DNA followed by the crystallization process (Figure 1.21A). For gold surface coating, the direct growth of CaP shells is difficult. One feasible method is to grow a polydopamine (PDA) shell before CaP coating (Figure 1.21).[106] The metal chelating property of PDA offers strong binding affinities to CaP. Considering the successful synthesis of DNA/Fe CPs, the study of (iron phosphate)FeP coating with Fe^{2+} ions on both DNA and AuNPs becomes interesting topics.

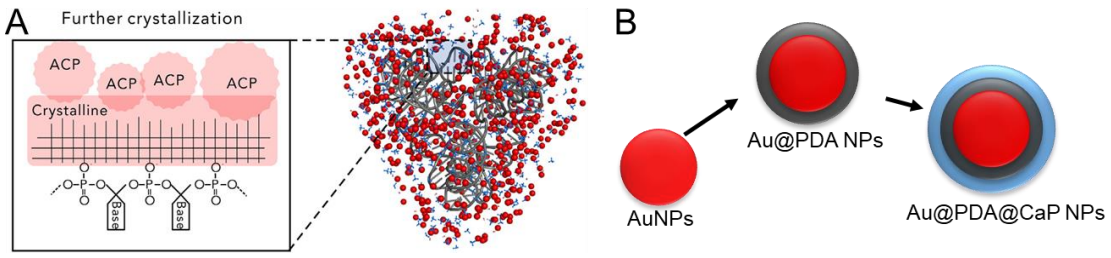

Figure 1.21 Schematic illustrations of (A) CaP growth on DNA origamis and (B) CaP growth on polydopamine coated AuNPs.[105] Figure A adapted with permission from ref ([105]). Copyright © 2019 Published by Elsevier Inc.

1.4 Gold Nanomaterial-Based Colorimetric Sensors

Over the past decades, gold nanomaterials were widely used for diverse colorimetric sensors.[107-111] The color changes were mainly from two sensing strategies: (a) morphology or aggregation state change of gold nanomaterials; and (b) catalysis of a chromogenic substrate (e.g., 3,3',5,5'-tetramethylbenzidine (TMB)).[112] In this section, these two sensing strategies are introduced. For the catalysis, we focused on the peroxidase-like activity of spherical AuNPs.

1.4.1 Morphology-dependent colorimetric sensors

AuNPs possess high extinction coefficients, which are usually serval orders of magnitude higher than typical organic dyes. Therefore, even low nanomolar AuNPs are easily observed by the naked eyes.[40] When the aggregation of dispersed AuNPs happened, the strong plasmon coupling between the nearby AuNPs would lead to a large red-shift in their absorption spectra (Figure 1.22A).[70, 113] Simultaneously, the color of solution shows an obvious color change from wine-red to purple or blue.[114-115] Similarly, color change and related colorimetric sensors can also be obtained with the reverse process of dis-aggregation. For example, DNA-assembled AuNPs can be redispersed by heating, or by the addition of the cDNA of the linker to disrupt the linkages, which was utilized for DNA detection.[116-117] Although the AuNP-aggregation-based sensors own high sensitivity and simplicity, they still have some disadvantages. First, nonresponse aggregations happen frequently. Second, extensive and uncontrolled aggregations may lead to very large aggregates, which are hard to be observed by the naked eyes.[112]

Colorimetric sensors can also be designed based on controlled growth of shells on gold cores.[118] The growth can be divided into two main categories based on the shell material: homoepitaxial growth and heteroepitaxial growth.[119] These growth modes could lead to changes in size, shape, or composition (Figure 1.22B). These changes not only significantly shift the LSPR peak but also change the surface-related

properties (e.g., surface-enhanced Raman scattering (SERS)). For example, with the heterophilic growth of silver shells, the core-shell Au@Ag structures can dramatically enhance the Raman intensity.[120]

As the reverse process of growth, the etching of gold nanomaterials usually needs harsh conditions.[111, 121] To make the etching process more easily, many etching-based sensors were designed with anisotropic nanostructures.[110] These anisotropic nanostructures usually have surfaces with high surface energies, suitable for the target molecules guided etching.[112] One well-known structure is gold nanorods (AuNRs), which can be etched along the longitudinal direction. As a result, a multicolor sensor is obtained (Figure 1.22C).

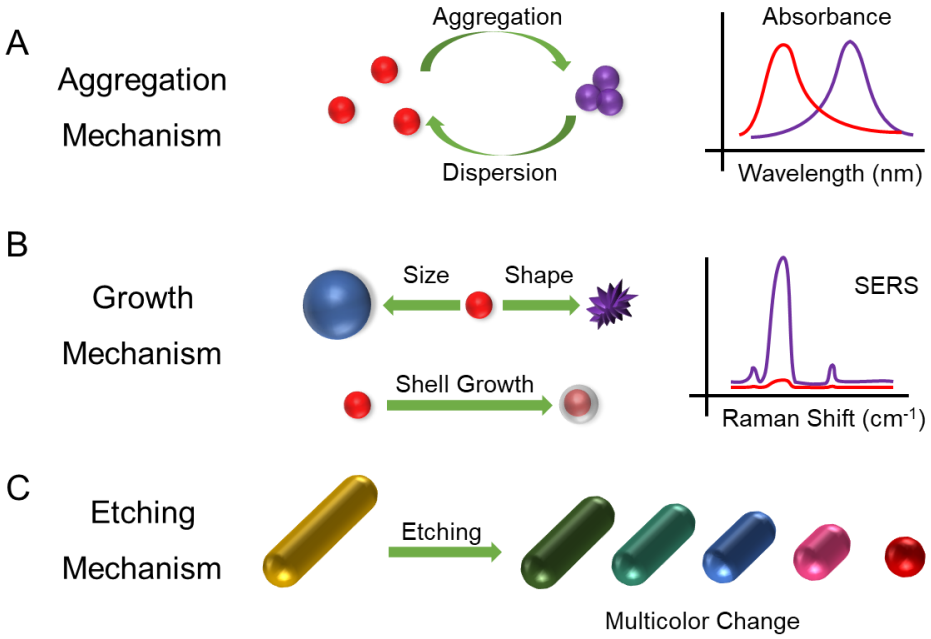

Figure 1.22 Schematic illustrations of three morphology change sensing mechanisms: (A) aggregation, (B) growth, and (C) etching.

1.4.2 **AuNPs for catalysis**

1.4.2.1 **Introduction to Au nanozymes**

During the last decade, more and more nanomaterials have been found with diverse enzyme-mimicking activities. These nanomaterials with enzyme-like activities are named nanozymes.[122-123] In 2004, Rossi et al. found that the naked AuNPs had glucose oxidase (GOx) like activity.[124] Three years later, Yan and co-workers reported that Fe_3O_4NPs possess peroxidase-like activity and applied them in an immunoassay.[125] This finding promoted the study of the peroxidase-like activity of AuNPs, which can catalyze some chromogenic substrates (e.g., TMB) in the presence of H_2O_2.[126-128] Therefore, an application

of AuNPs with peroxidase-like activities is the detection of H_2O_2. When glucose is added, under suitable conditions, AuNPs can show both GOx and peroxidase-like activities (Figure 1.23).[129-132] In this case, the amount of oxidized TMB also indicates the concentration of glucose.[133]

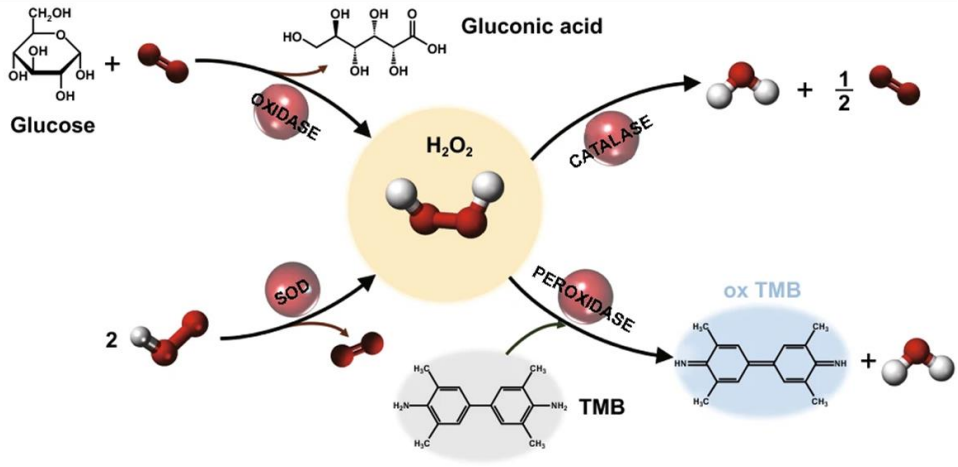

Figure 1.23 Schematics of three typical enzyme-like activities of AuNPs: GOx, SOD, and peroxidase. Small white and red balls are respectively hydrogen and oxygen atoms. Figure adapted with permission from ref ([134]) with open access.

1.4.2.2 **Enhancement of peroxidase-like activities of AuNPs**

The peroxidase-like activities of AuNPs are mainly dependent on two factors: size and surface coating. For spherical AuNPs, smaller AuNPs usually possess higher peroxidase-like activities.[135-136] Since most AuNPs were prepared by using citrate as a reducing agent, citrate-capped AuNPs have been extensively studied for the peroxidase-like activities. Due to the weak interactions between citrate molecules and gold surface, many other ligands, especially thiol-contained molecules, can replace citrate by ligand exchange.[137] It was reported that amino capped AuNPs could inhibit the catalytic activity of AuNPs.[138] Besides surface ligands, smaller metal ions can also alter the peroxidase-like activity of AuNPs. In 2011, Huang et al. found that Hg^{2+} can remarkably enhance the peroxidase-like activity of AuNPs.[139] In addition to organic ligands and metal ions, AuNPs can also be coated by inorganic shells. For example, the enhancement of peroxidase-like activities was realized by coating with a more active material such as Pt.[140]

1.5 Research Goals and Thesis Outline

The main goals of this thesis include two main parts (Figure 1.24). On one hand, DNA sequences and metal ions are screened to improve the DNA adsorption on two types of 2D nanomaterials. For GO, PS-modified DNA was used to improve DNA binding affinity. For Ti_2C MXene, by screening suitable

metal ions, I aimed to realize direct high DNA density adsorption. The forces of DNA adsorption and the roles of metal ions on GO and MXene were also studied. On the other hand, I synthesized new DNA/Fe/AuNPs composite nanomaterials to explore the applications of DNA/Fe CPs and FeP complexes. The optimization of synthetic conditions was also a research goal of the thesis. Finally, in the last year of my PhD research, I worked on a project related to developing plasmonic nanomaterials for the detection of SARS-CoV-2 virus. My goal was to understand the etching of gold nanomaterials using typical colorimetric products from immunoassays to obtain enhanced color change.

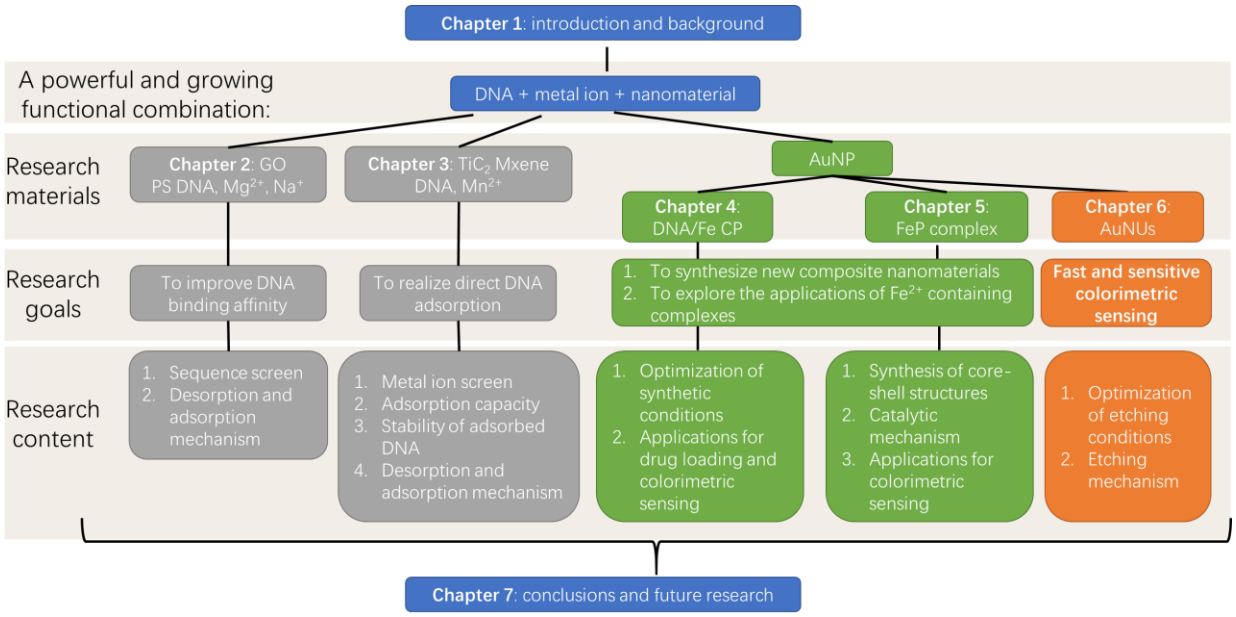

Figure 1.24 Thesis outline flow diagram.

Chapter 2 describes the adsorption of PS DNA PO DNA on GO. Mg^{2+} and Na^{+} salts were used to screen the charge repulsion between negatively charged DNA and GO. First, PS DNA adsorbs stronger on GO was confirmed by the displacement experiments. Then, the DNA adsorption mechanism was studied by both experimental studies and MD simulations. The results showed that PS DNA has stronger VDW forces than normal DNA. With this conclusion, PS poly-C was screened with the highest affinities to GO surfaces, which could be used as a stable anchor sequence.

Chapter 3 describes Mn^{2+}-mediated DNA adsorption on Ti_2C MXene. First, a group of metal ions was screened to confirm the unique performance for Mn^{2+}. In addition, Mn^{2+}-mediated DNA adsorptions on GO and MoS_2 were also studied side by side. Then, the kinetics and capacity of DNA adsorption on Ti_2C MXene were evaluated by fluorescence quenching. Lastly, the mechanisms of DNA adsorption and desorption on MXene were studied, including the adsorption of dsDNA.

Chapter 4 describes the synthesis of new Au@DNA/Fe core-shell NPs. The DNA/Fe CPs were formed with the high local DNA density on the AuNPs promoted and characterized by TEM and UV-vis spectrometry. More importantly, the sizes of Au@DNA/Fe NPs could be controlled by varying the DNA and Fe^{2+} concentrations. The selective removals of Au cores or DNA/Fe shells were utilized for drug loading and phosphate sensing.

Chapter 5 describes the FeP coatings on AuNPs and Au@DNA NPs. First, a series of Au@FeP core-shell structures with various shell thicknesses were synthesized and characterized by TEM and UV-vis spectrometry. The improvements in the stabilities and catalytic activities of Au@FeP NPs were also tested by NaCl and TMB substrate. Then, the enhancement in peroxidase-like activity was studied by substituting cores (AuNS and SiO_2) and adding capping MCH ligands. In addition, the catalytic performance reflected that the growth of crystalline FeP could be affected by the adsorbed DNA on AuNPs. In the end, a colorimetric sensor for detecting Fe^{2+} was developed based on the enhanced peroxidase-like activities of Au@FeP NPs.

Chapter 6 describes a new developed AuNU-etching-based colorimetric sensor for H_2O_2 detection. First, TMB^+-mediated etching of AuNUs was confirmed by TEM and UV-vis spectrometry. In addition, AuNUs were more easily etched than AuNRs, which was confirmed by conducting experiments side by side. Then, the effects of halides, surfactants, etching time, and pH on etching were systematically studied. Lastly, a sensitive H_2O_2 sensor based on AuNUs' etching was constructed.

Chapter 7 describes the conclusion in each chapter of this thesis, and recommendations for future studies.

Chapter 2 Stronger Adsorption of Phosphorothioate DNA on Graphene Oxide

The results presented in this chapter have been published as:

Zhicheng Huang, Yu Zhao, Biwu Liu, Shaokang Guan, and Juewen Liu, Stronger Adsorption of Phosphorothioate DNA Oligonucleotides on Graphene Oxide by van der Waals Forces. *Langmuir* 2020, 36 (45), 13708-13715.

2.1 Introduction

Functionalization of inorganic nanomaterials with DNA is of great interest for biosensor development,[7, 141-143] DNA-directed assembly,[144-145] and drug delivery.[31, 146] While covalent conjugation has been a popular method to achieve highly stable and directional linkages, simple physisorption is often used for its simplicity and cost-effectiveness.[48, 147-148] For example, fluorescently labeled DNA oligonucleotides were adsorbed on graphene oxide (GO) as biosensors,[149-152] taking advantage of the appropriate adsorption strength and fluorescence quenching properties of GO. For certain surfaces such as transition metal dichalcogenides, stable covalent linkages are difficult to achieve and physisorption has been the choice for most researchers.[153-155] Aside from covalent linking and random physisorption, a diblock DNA strategy was also used. One block is used to tightly adsorb on the surface while the other block performs functions such as hybridization.[5, 55, 156-157] This strategy enables both optimal function and simplicity. For this diblock strategy to work, a key requirement is a high-affinity DNA sequence to adsorb on intended surfaces.

Searching for DNA sequences that can tightly adsorb on inorganic surfaces has been a long-standing challenge. Typical aptamer selection procedures cannot be effectively applied to inorganic materials due to strong non-specific adsorption.[158] In this regard, screening of a smaller set of DNA could be more productive since it allows discrimination of more subtle differences between similar DNA sequences via competitive assays.[158] The most successful examples are probably the screen of DNA oligonucleotides for sorting carbon nanotubes by Zheng and coworkers.[159-161]

Regarding DNA sequence-dependent adsorption, some scattered information has been accumulated in the past few decades. For example, poly-adenosine (poly-A) DNA is known to bind more strongly to gold surfaces than other types of DNA.[75] Poly-A DNA has also been used for anchoring on GO.[58] We found that poly-C DNA has the highest affinity on a few carbon, metal oxide, metal phosphate, and metal dichalcogenide surfaces.[50, 156, 162-163] Recently, poly-C DNA was also reported to adsorb strongly on upconversion nanoparticles.[157]

To further enhance adsorption affinity, one method is to chemically modify DNA. While many modifications focused on DNA bases, DNA backbone modification is also quite interesting. For example, using peptide nucleic acids (PNA) and similar modifications, adsorption on GO was enhanced, likely due to their lack of charge repulsion on GO.[164-165] A phosphorothioate (PS) modification refers to replacing one of the non-bridging oxygen atoms in the DNA phosphodiester (PO) backbone by sulfur. Compared to PNA, PS modification is much more cost-effective. PS-modified DNA has been widely used as biochemical probes for ribozyme and DNAzyme research and related biosensor development.[166] Using PS DNA to modify AuNPs,[167] and quantum dots[22, 168] has also been carried out, taking advantage of the thiophilicity of their metal species.[169] An interesting question is whether PS DNA can adsorb more strongly on surfaces that do not contain thiophilic metals. We report in this work that PS DNA adsorbs more tightly than unmodified DNA of the same sequence on GO, and PS poly-C DNA is ideal for the preparation of more stably adsorbed DNA probes.

2.2 Materials and Methods

2.2.1 Chemicals

All of the DNA samples were purchased from Integrated DNA Technologies (IDT, Coralville, IA). Carboxyl graphene oxide (GO) was purchased from ACS Material LLC (Medford, MA). Sodium dodecyl sulfate (SDS), cetrimonium bromide (CTAB), Triton X-100, Tween 80, and bovine serum albumin (BSA) were from Sigma-Aldrich (St Louis, MO). Sodium chloride, sodium hydroxide, magnesium chloride, 4-(2-hydroxyethyl) piperazine-1-ethanesulfonate (HEPES), urea, and cytidine were from Mandel Scientific (Guelph, Ontario, Canada). Milli-Q water was used for preparing buffers and solutions.

2.2.2 Preparation of the DNA/GO complex

To adsorb DNA (PO and PS), all the samples were incubated in buffer A (5 mM HEPES, pH 7.5, 150 mM NaCl, 1 mM $MgCl_2$) at room temperature. The final concentrations were 2 μM PO or PS DNA, and they were incubated with 400 μg/mL GO. All the samples were stored at 4 °C for further use.

2.2.3 DNA displacement by DNA sequence

FAM-labeled DNA was adsorbed as described above. With 100 nM FAM-DNA on 20 μg/mL GO, almost all of the DNA was adsorbed and quenched by GO. For each sample, the fluorescence intensity of the free FAM-DNA in the same buffer but without GO was used to calculate the desorption percentage. Then, non-labeled PS or PO DNA was added to displace the adsorbed FAM-DNA in buffer A. 20 μg/mL DNA/GO complexes were used. The fluorescent intensity indicative of desorbed DNA was collected by a microplate reader (SpectraMax M3) with excitation at 490 nm and emission at 520 nm.

2.2.4 DNA displacement by polymers and surfactants

To probe the stability of DNA/GO complexes, 5 μL of concentrated competing agents (e.g. polymers, surfactants, and proteins) were respectively added to 95 μL DNA/GO complex (20 μg/mL) in buffer A. The amounts of the desorbed DNA were measured from the supernatants after centrifugation (15000 rpm, 15 min). For disruption of hydrogen bonding, concentrated DNA-GO complexes were added into 4 M urea solutions and incubated for 4 h. The final concentrations of the DNA/GO complexes were 20 μg/mL. After incubation, the supernatant of the mixture was used to measure fluorescence signal of the desorbed FAM-DNA.

2.2.5 DNA hybridization on GO surface

Two non-FAM labeled diblock DNA sequences containing PS-C_{15} or PO-C_{15} blocks were respectively adsorbed on GO in buffer A. The background fluorescence was measured for 95 μL 50 nM FAM-cDNA or FAM-rDNA in buffer A for 5 min. After this, 5 μL concentrated DNA/GO conjugates were added (final GO concentration was 10 μg/mL). For reactions containing competing molecules (BSA or Tween 80), they were added to the FAM-DNA samples before collecting the background fluorescence.

2.2.6 CD measurement

All the circular dichroism (CD) samples were prepared and kept at -20°C for one day before measurement. CD spectroscopy was performed in a 1 cm UV−vis quartz cuvette using a Jasco J-715 spectrophotometer. Citrate (pH 5.0, 5 mM) and HEPES buffers (pH 7.5, 5 mM) were measured as blanks. Each DNA sample (10 μM, 200 μL) was dissolved in 25 mM citrate or buffer A and was measured 5 times in continuous scanning mode (20 nm/min) from 220 nm to 320 nm.

2.2.7 MD simulations

GROMACS version 5.1.4 was used to perform the molecular dynamics (MD) simulations.[170] The simulation supercells were cuboid boxes of 60×60×50 $Å^3$, which consist of saline solution and a graphene oxide (GO) sheet at the bottom with a dimension of 50×50 $Å^2$. The initial ssDNA segment structure in the B-form was generated by the 3DNA.[171] The ssDNA segment was individually simulated for 100 ns until the conformation reached an equilibrium state. The GO model was based on $C_{10}O_1(OH)_1(COOH)_{0.5}$ which was reported by Yang et al.[172] In the simulations, the GO carbon atoms were constrained using position restraints, while the other oxygen and hydrogen atoms were free to move. The neutral solution environment consisted of a ssDNA strand, ~5100 water molecules, and Na^+ and Cl^- counterions, in which the optimized ssDNA was initially put at 30 Å above the GO sheet.

Amber14SB and TIP3P were respectively used to model DNA/ions and water molecules.[173-174] The force field parameters for the GO sheet, including partial charges of functional groups, were taken from Stauffer et al. and general force field.[175-176] The electrostatic interactions were evaluated using a particle-mesh Ewald (PME) summation, with the real space cutoff of 14 Å.[177] The Lennard-Jones (L-J) nonbonded interactions were smoothly tapered to zero when the two atoms were close to 14 Å. Three-dimensional periodic boundary conditions were applied in the simulations, and all the simulations were carried out with a time step of 2 fs. The temperature was maintained at 300 K under the NVT ensemble via the V-rescale thermostat. Each of PO-A_{15}, PS-A_{15}, PO-C_{15}, PS-C_{15} DNA was relaxed for 1 ns at ambient temperature of 300K. They were heated to a target temperature of 550 K and equilibrated for 10 ns. Then, the systems were cooled to 300 K with a stepped cooling pattern at a speed of 100 K/10 ns. Finally, the systems were equilibrated at 300 K for 100 ns to obtain their binding energies.

Table 2.1 DNA sequences and modifications used in this work. The PS modifications are denoted by the asterisks. FAM: carboxyfluorescein.

ID	DNA Names	Sequences 5′-3′
1	FAM-12mer DNA	FAM-TCACAGATGCGT
2	FAM-cDNA	FAM-ACGCATCTGTGA
3	FAM-rDNA	FAM-AGAGAACCTGGG
4	PS-C_{15}-12mer	TCACAGATGCGTC*C*C*C*C*C*C*C*C*C*C*C*C*C*C*C
5	PO-C_{15}-12mer	TCACAGATGCGTCCCCCCCCCCCCCC
6	FAM-PO-C_5	FAM-CCCCC
7	FAM-PO-A_5	FAM-AAAAA
8	PS-C_5	C*C*C*C*C
9	PO-C_5	CCCCC
10	PS-A_5	A*A*A*A*A
11	PO-A_5	AAAAA
12	FAM-PS-C_{15}	FAM-C*C*C*C*C*C*C*C*C*C*C*C*C*C*C
13	FAM-PO-C_{15}	FAM-CCCCCCCCCCCCCCC
14	FAM-PS-A_{15}	FAM-A*A*A*A*A*A*A*A*A*A*A*A*A*A*A
15	FAM-PO-A_{15}	FAM-AAAAAAAAAAAAAAA

16	FAM-PS-T_{15}	FAM-T*T*T*T*T*T*T*T*T*T*T*T*T*T*T
17	FAM-PO-T_{15}	FAM-TTTTTTTTTTTTTTT
18	PS-C_{15}	C*C*C*C*C*C*C*C*C*C*C*C*C*C*C
19	PO-C_{15}	CCCCCCCCCCCCCCC
20	PS-A_{15}	A*A*A*A*A*A*A*A*A*A*A*A*A*A*A
21	PO-A_{15}	AAAAAAAAAAAAAAA
22	PS-T_{15}	T*T*T*T*T*T*T*T*T*T*T*T*T*T*T
23	PO-T_{15}	TTTTTTTTTTTTTTT

2.3 Results and Discussion

2.3.1 PS DNA and GO

The structure of a normal DNA dinucleotide (called PO for phosphodiester linkages) is shown in Figure 2.1A, and its PS modification is shown in Figure 2.1B. The slightly larger sulfur does not significantly perturb DNA duplex structure, although the stability is slightly lower than a normal PO duplex.[169, 178] PS modifications are attractive for practical applications since they can be made in tandem at a low cost. In this work, we systematically compared PO and PS DNA of the same sequence for adsorption on GO. A TEM micrograph of our GO sample is shown in Figure 2.1C. The carboxylic groups on GO led to a negatively charged surface. Since DNA is also negatively charged, long-ranged electrostatic repulsion needs to be overcome before adsorption.[49] Therefore, we used a relatively high salt concentration to screen the charge repulsion.

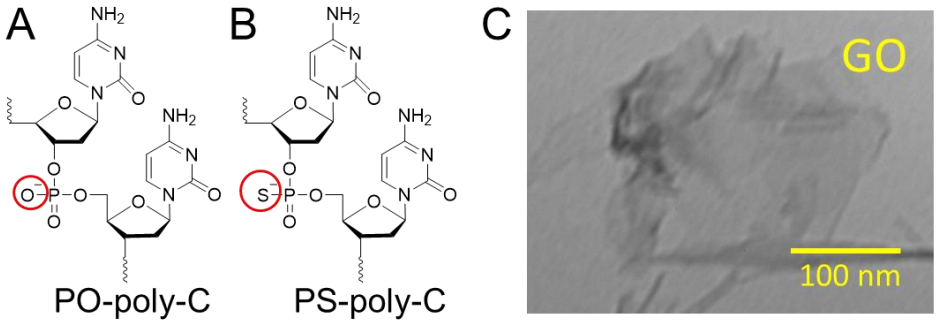

Figure 2.1 Chemical structures of (A) a normal poly-cytosine DNA with phosphodiester (PO) linkages, and (B) its PS modification. (C) A TEM micrograph of the GO used in this work.

2.3.2 **PS DNA adsorbs stronger on GO**

Poly-C DNA was recently found to strongly adsorb on many surfaces, while poly-A DNA ranked the next for GO.[156] Since we were interested in searching for strongly adsorbing sequences, poly-A and poly-C DNAs were tested. To compare the affinity between PS and PO DNA on GO, we designed the following experiments (Figure 2.2A). We adsorbed a FAM-labeled DNA (e.g. FAM-C_5) on GO, resulting in quenched fluorescence. Then, a non-labeled DNA (PO or PS C_5) was added to displace the adsorbed probe, which was monitored by fluorescence increase. Interestingly, adding PS-C_5 produced a ~40% stronger final fluorescence than adding PO-C_5 (Figure 2.2B). Adding PS-A_5 also produced 50% higher fluorescence than PO-A_5 when FAM-A_5 was adsorbed on GO (Figure 2.2C). Therefore, PS DNA appeared to adsorb more strongly than PO DNA of the same sequence. To confirm this observation, the displacement experiment was carried out with different concentrations of the competing DNA. The PS DNA displaced more FAM-labeled DNA from GO than the PO DNA did when the DNA was more than 100 nM (Figure 2.2D and E). At low DNA concentrations, there was sufficient free space on the GO, and the displacement reaction could not take place effectively.

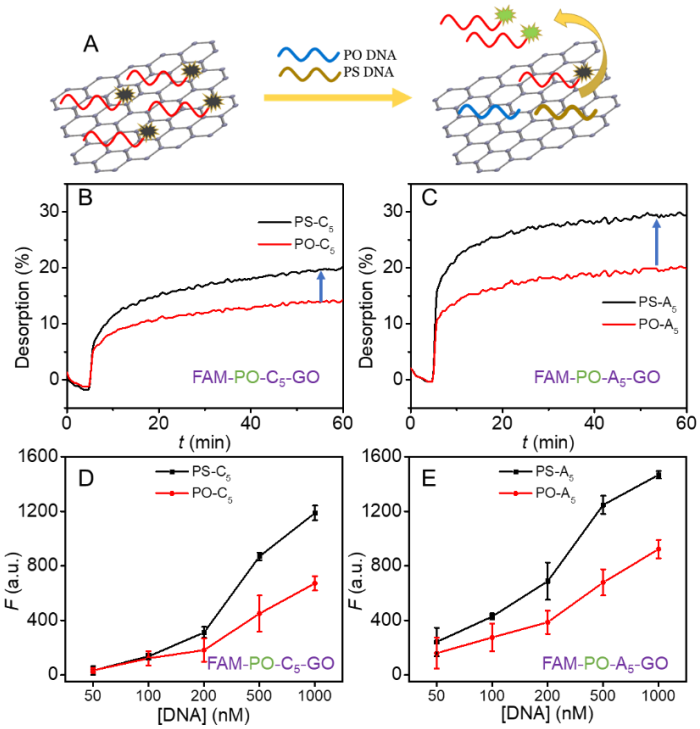

Figure 2.2 (A) A scheme showing the displacement experiment. Adding non-labeled PO or PS DNA to displace the adsorbed FAM-labeled DNA, resulting in fluorescence enhancement. Kinetics of fluorescence increase due to displacement of (B) FAM-C_5 and (C) FAM-A_5 DNA from GO by 500 nM non-labeled 5-mer PO or PS DNA in buffer A. The desorption of (D) FAM-C_5 (E) FAM-A_5 from GO by various concentrations of non-labeled DNA.

2.3.3 **High-affinity DNA sequences**

The above study used short 5-mer DNA, which cannot form a stable duplex or internal secondary structures. We intentionally chose 5-mer DNA to simplify our analysis and to ensure that we only probed the displacement reaction. For practical applications, DNA sequences are likely to be longer. Therefore, we also tested FAM-labeled A_{15} and C_{15} PO and PS DNA (a total of four sequences). These DNAs were respectively adsorbed onto GO, and then the same four DNAs but without the FAM labeled were added to induce desorption (Figure 2.3A). The data were plotted in four groups and each group was for a FAM-labeled DNA. In each group, the red bar is always the highest, indicating that PS-C_{15} was the most potent in terms of displacement. When FAM-PS-C_{15} was adsorbed as a probe, it was least desorbed by the other DNA (e.g. the last set of bars are the shortest). PS-A_{15} was also adsorbed more strongly than PO-A_{15}. Therefore, PS DNA was adsorbed more strongly than PO DNA of the same sequence, true for both 5-mer and 15-mer DNA. Among this group of DNA, PS-C_{15} had the highest adsorption affinity on GO.[156]

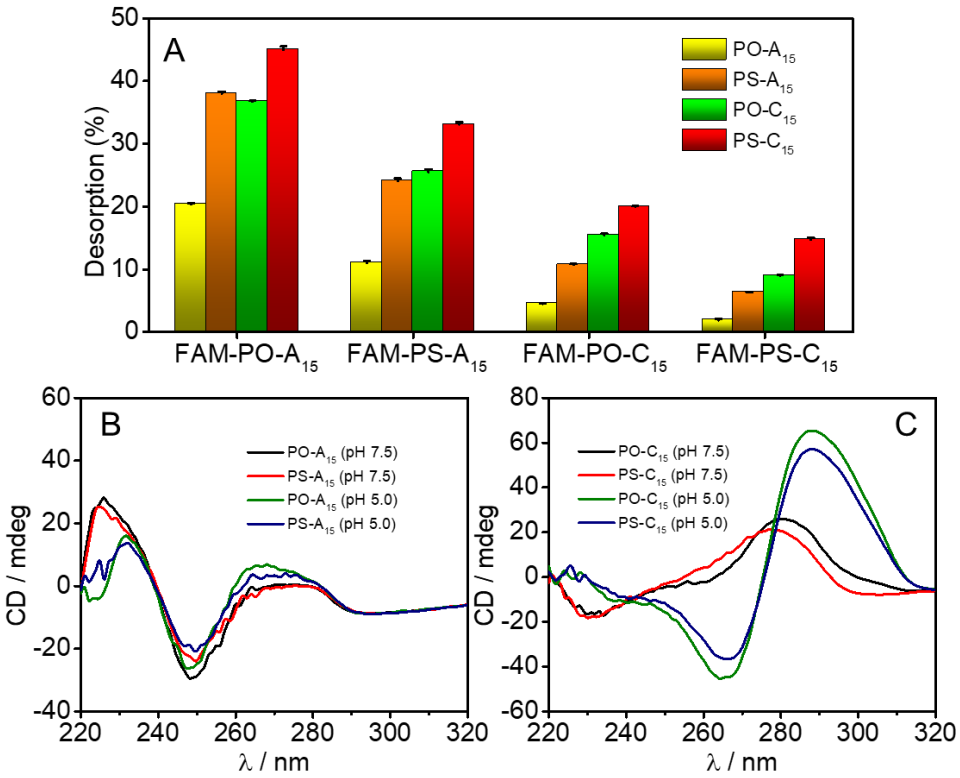

Figure 2.3 (A) Percentage of desorption of various 15-mer FAM-labeled DNA homopolymers from GO induced by four 500 nM non-labeled DNAs in buffer A (5 mM HEPES, pH 7.5, 150 mM NaCl, 1 mM $MgCl_2$) after 4 h incubation. CD spectra of 10 µM PO and PS (B) A_{15} and (C) C_{15} in buffer A (pH 7.5) and 25 mM citrate buffer (pH 5.0).

Since DNA conformation may also influence adsorption affinity, we then performed CD spectroscopy to probe DNA conformation. Since our experiments were mainly performed at neutral pH, we measured the CD signal at pH 5.0 and pH 7.5, with the acidic samples serving as controls. Under acidic conditions, both poly-A and poly-C DNA can fold into specific secondary structures, which may influence the interaction between DNA and nanomaterials.[108, 179] No difference was observed in the CD spectra between PO-A_{15} and PS-A_{15} at both pH 7.5 and 5.0 (Figure 2.3B). Therefore, the possibility of forming the parallel poly-A duplex (A-motif) structure was excluded.[180-181] Since adenine has a pK_a of ~3.5, its protonation and forming A-motif requires an even lower pH. Makino and coworkers showed that PS poly-C DNA could also form four-stranded quadruplex (i-motif) structures similar to the PO poly-C DNA, although with a lower stability.[182-183] Our CD data supported the formation of an i-motif in both PO- and PS-poly-C at pH 5.0 (Figure 2.3C). From the CD data, the conformations of the PO and PS DNA appeared to be quite similar, and the higher affinity of the PS DNA may not be explained by their different conformations.

2.3.4 **Hybridization and desorption**

In addition to the displacement reaction, we also studied DNA hybridization. By introducing PS DNA, a total of four combinations are possible to form duplex DNA (e.g. PO/PO, PO/PS, PS/PO, and PS/PS). Although they have the same sequence, the duplex stability is different. In general, PO/PO has the highest melting temperature (T_m), while the PS/PS duplex is the least stable.[184-185] DNA tends to form a duplex if the duplex has a high T_m.

We picked FAM-A_{15} and FAM-T_{15}, since poly-C and poly-G DNA can form various secondary structures and complicate data analysis. When FAM-A_{15} PO DNA (Figure 2.4A) and PS DNA (Figure 2.4B) were adsorbed on GO as probes, PO T_{15} produced stronger signals in both cases. This is different from the displacement reaction seen above, and thus hybridization might take place. We attributed the stronger signal with the PO DNA to the difference in duplex stability between the PS and PO DNA. Duplex formed by PO DNA is more stable than that by PS DNA (e.g. higher T_m).[184-185]

The opposite, however, was observed when we adsorbed FAM-T_{15} DNA on GO and then added non-labeled A_{15} DNA (Figure 2.4C and D). In these two samples, the PS DNA produced stronger signals. Previous research showed that poly-A DNA is adsorbed much more tightly than poly-T DNA on GO.[46] In this case, non-specific displacement by the stronger poly-A DNA outcompeted the effect of hybridization. In particular, the PS A_{15} DNA adsorbed even more strongly than the PO A_{15}, yielding the observed results.

For all these samples, when a PS DNA was adsorbed, desorption by its complementary DNA is in general less than when a PO DNA was adsorbed. The fact that PS DNA hybridizes more weakly with its

PO counterpart could be useful for bioconjugation, since it might form a more stable adsorption complex on GO and is less affected by the complementary DNA. At the same time, its stronger affinity also makes it resistant to displacement by non-complementary DNA. Overall, these hybridization experiments indicated a quite complicated interplay between adsorption affinity and hybridization affinity for PS and PO DNA on GO, but the overall results favor the use of PS DNA as an anchoring block.

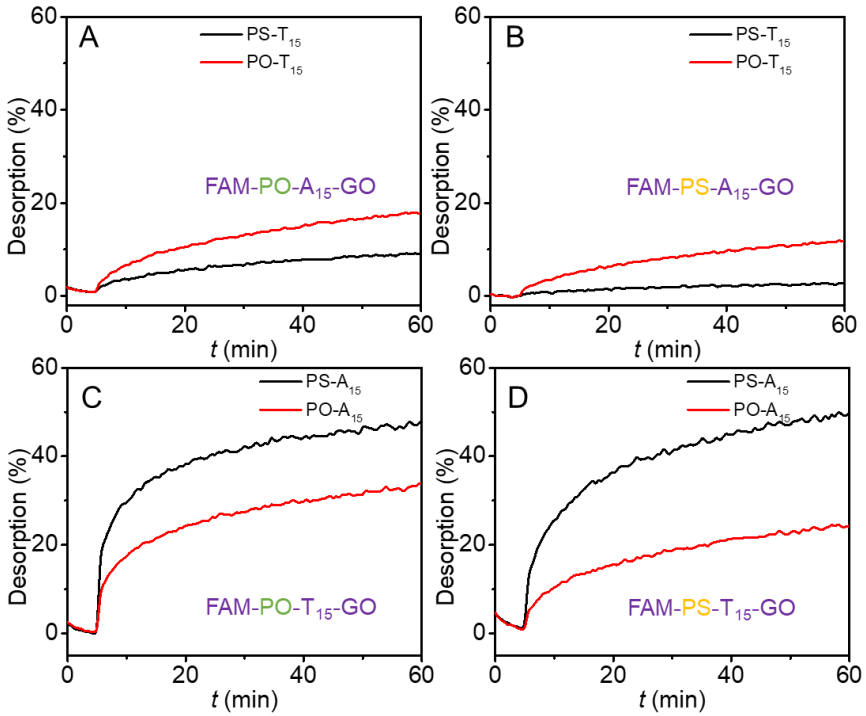

Figure 2.4 Kinetics of desorption of FAM-labeled DNA from GO induced by non-labeled complementary DNA. In this set of experiments, the following four FAM-labeled DNAs were used: (A) FAM-PO-A_{15}, (B) FAM-PS-A_{15}, (C) FAM-PO-T_{15}, and (D) FAM-PS-T_{15}. The reaction was in 5 mM HEPES buffer, pH 7.5, with 150 mM NaCl, 1 mM $MgCl_2$. Desorption was induced by adding 500 nM DNA.

2.3.5 **Desorption and adsorption mechanism**

The above studies used only DNA to probe the adsorption strength. To gain insights into adsorption mechanism, we also challenged the adsorbed DNA with a few denaturing agents. Urea is a hydrogen bond disruptor, and hydrogen bonding is known to be important for DNA adsorption on GO.[186] Among the four DNA sequences, PS-C_{15} DNA appeared to be the most resistant to urea-induced desorption (Figure 2.5). Only 19.2±2.4% of the PS-C_{15} DNA desorbed by 4 M urea, while 29.8±0.4% of the PO-C_{15} desorbed under the same condition. A similar trend was also observed for A_{15} DNA. Therefore, PS DNA was also adsorbed more strongly when challenged by urea. We reason that when hydrogen bonding was disrupted by urea, the remaining forces were still strong for the PS DNA to allow its adsorption.

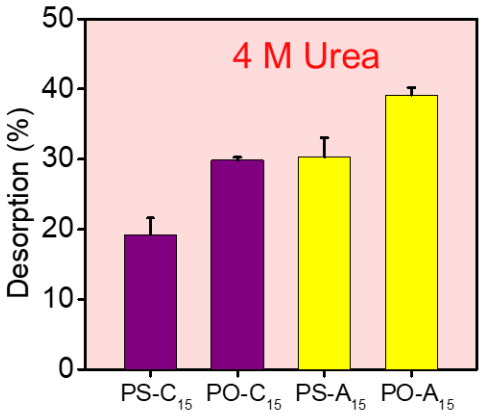

Figure 2.5 FAM-labeled DNA desorption induced by 4 M urea in buffer after 4 h incubation.

We then compared the PO- and PS-C_{15} DNA when challenged by other chemicals (Figure 2.6B). Four surfactants with different molecular weights, charge, and hydrophobicity were tested (Figure 2.6A). SDS, CTAB and Triton X-100 had almost no effects on the adsorbed DNA on GO,[187] but Tween 80 desorbed both DNA strands from GO (with less desorption of FAM-PS-C_{15}). Based on the HLB (hydrophilic-lipophilic balance) values of Tween 80 (15) and Triton X-100 (13.4), Tween 80 is slightly more hydrophilic than Triton X-100. Moreover, Tween 80 has a higher molecular weight than the other surfactants. Its combined hydrophobicity and molecular weight might make Tween 80 a strongly adsorbing molecule on GO. We further added a protein, BSA (the last set of bars in Figure 2.6B), and again, more FAM-PO-C_{15} was desorbed than FAM-PS-C_{15}.

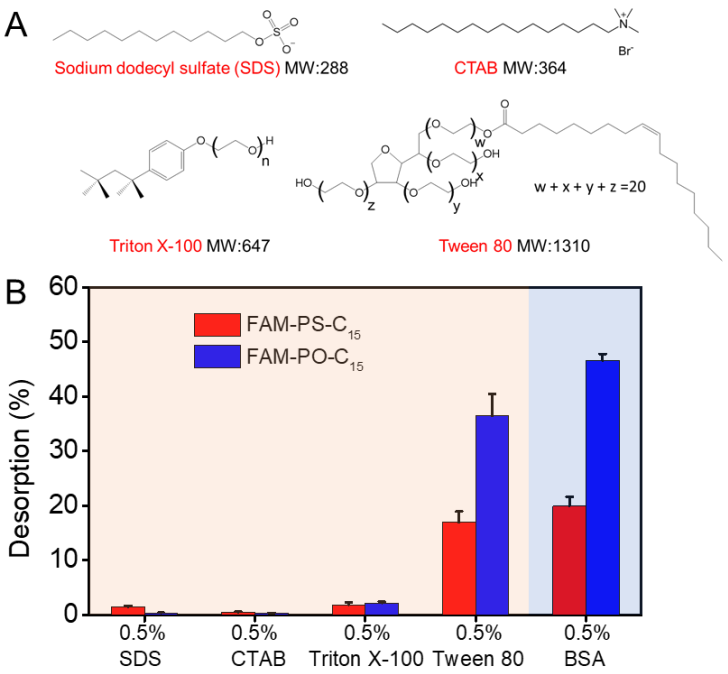

Figure 2.6 (A) Molecular structures of three surfactants (SDS, CTAB, Triton X-100, and Tween 80). (B) Desorption of FAM-labeled DNA from GO by various surfactants and BSA protein after 1 h incubation in buffer A. All the samples contained 20 μg/mL GO with pre-adsorbed FAM-labeled DNA.

DNA can interact with surfaces via its nucleobases and/or the phosphate backbone.[49] After PS modifications, the interactions with soft metals (e.g. Au, Cu^{2+}, Cd^{2+}) is expected to increase, while the interactions with hard metals (e.g. Mg^{2+}) are weakened (Figure 2.7A).[188] Since GO does not have metal species, this type of interaction is not important for GO. Another potential interaction force is hydrogen bonding. The oxygen on the phosphate can be a hydrogen bond acceptor ($pK_a < 2$ and thus unlikely to be a hydrogen bond donor). Since sulfur is a weaker hydrogen bond acceptor, PS DNA is at a disadvantage for hydrogen bonding too (Figure 2.7B).[189] PS modifications still retain the negative charge, and electrostatic interaction is not expected to change much either (Figure 2.7C). Finally, van der Waals (VDW) forces are ubiquitous. Compared with oxygen, due to the larger atomic radius and easier to polarize, sulfur might support a stronger VDW interaction (Figure 2.7D). For other forces from the DNA bases, such as π-π stacking and DNA base related hydrogen bonding, PO and PS DNA should be similar and thus are not discussed here.

Based on our data and this surface force discussion, the only force that may explain the stronger adsorption of PS DNA is the VDW force. To further understand the VDW force between DNA and GO, we used molecular dynamics (MD) simulations to calculate the adsorption energies of PO-A_{15}, PS-A_{15}, PO-C_{15}, and PS-C_{15} on GO (20% oxygen content) in neutral solutions (Figure 2.7E). MD is a powerful method

to understand DNA adsorption.[190] The simulation results showed that, with the same sequences, PS DNA can adsorb on GO more tightly than the PO DNA of the same sequence, which was consistent with our experimental results. The adsorption energies were split into VDW and electrostatic energies. In terms of electrostatic energies, the differences were very small (within 1.3%) between PO-C_{15} and PS-C_{15}, consistent with our discussion above. However, obvious increases in the VDW energies for both PS DNA strands were observed (8.3-14.7%) due to the PS modifications. To observe the adsorbed geometry visually, we captured the steadily adsorbed state conformation of PS-C_{15} at the end of the simulation (Figure 2.7F).

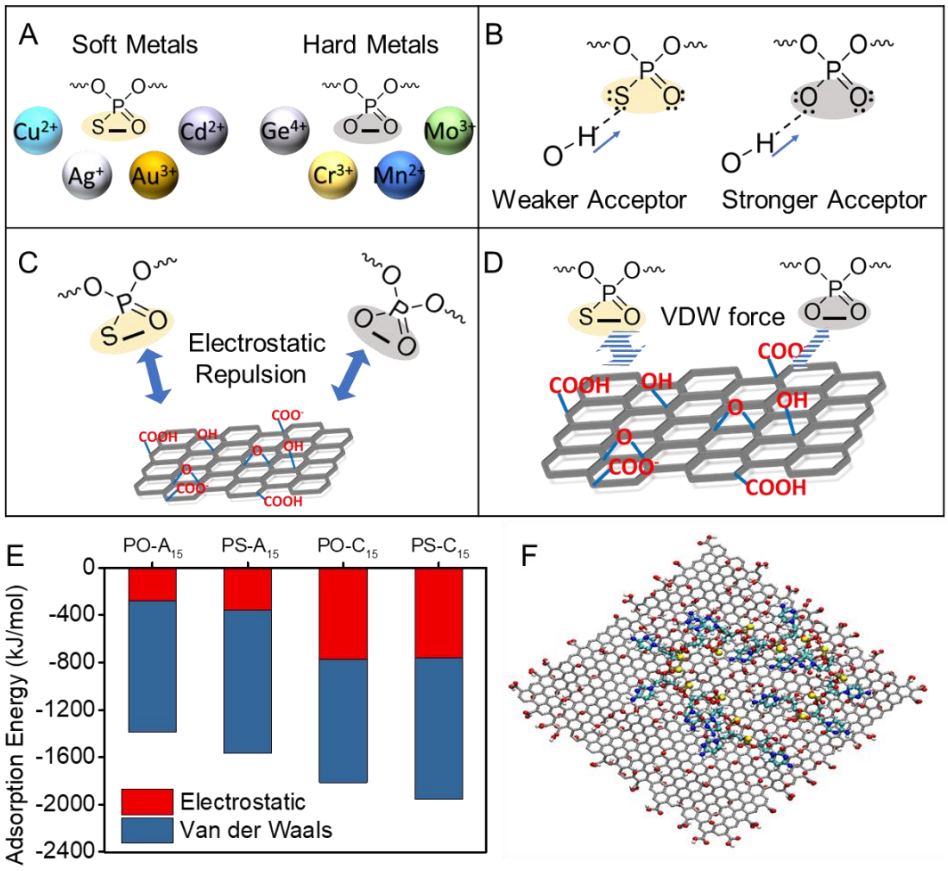

Figure 2.7 Schemes of the differences between PO-DNA and PS-DNA in four main possible interactions: (A) Lewis acid and base interaction; (B) hydrogen bonding; (C) electrostatic repulsion; and (D) VDW force. (E) MD simulation calculated adsorption energies of PO-A_{15}/GO, PS-A_{15}/GO, PO-C_{15}/GO and PS-C_{15}/GO conjugates in neutral solutions, consist of electrostatic and VDW energies. (F) The steadily adsorbed state conformation of PS-C_{15} on GO.

2.3.6 **Highly stable PS DNA anchors**

The stronger affinity of PS poly-C DNA may allow it to act as a stable anchoring sequence on GO. For example, we can design a diblock DNA with one block being PS-poly-C and the other block for hybridization with the target DNA. Since the anchoring block has a stronger affinity, it can displace the adsorbed probe block to force the probe block to be away from the GO surface and become available for hybridization (Figure 2.8A). To test this, we respectively adsorbed two diblock DNAs with C_{15}-PO and C_{15}-PS next to the same probe sequence. After adding the GO/diblock DNA conjugates to a FAM-labeled target DNA, the quenching efficiency (i.e., due to DNA hybridization) was about 40% higher with the PS-C_{15} anchor compared to the PO-C_{15} anchor (Figure 2.8B and C).

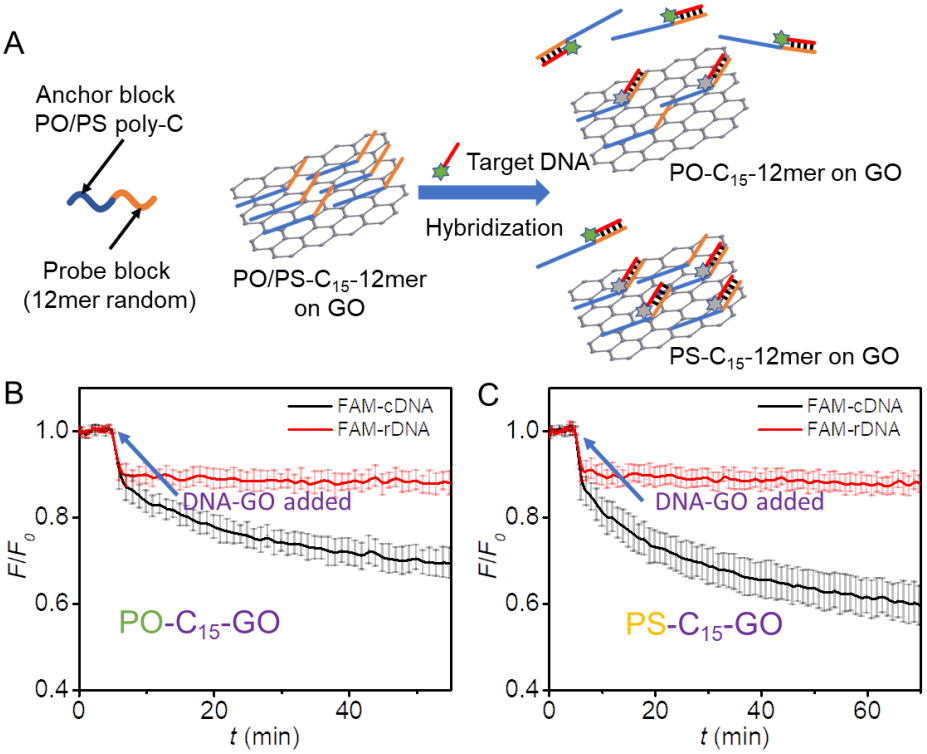

Figure 2.8 (A) A scheme showing adsorption of diblock DNAs containing a PO or PS poly-C anchoring block and a probe block. The PO anchor is less stable and more prone to desorb. Hybridization of a FAM-labeled target DNA can be followed by fluorescence quenching. Kinetics of specific hybridization with the FAM-cDNA and non-specific adsorption of the FAM-rDNA on (B) PO-C_{15} and (C) PS-C_{15} anchored probes on GO.

We further challenged the system by adding BSA and Tween 80, which may displace the adsorbed probe DNA (Figure 2.9). In these systems, the PS-C_{15} anchored probe still showed better hybridization, since it was more resistant to such displacement.

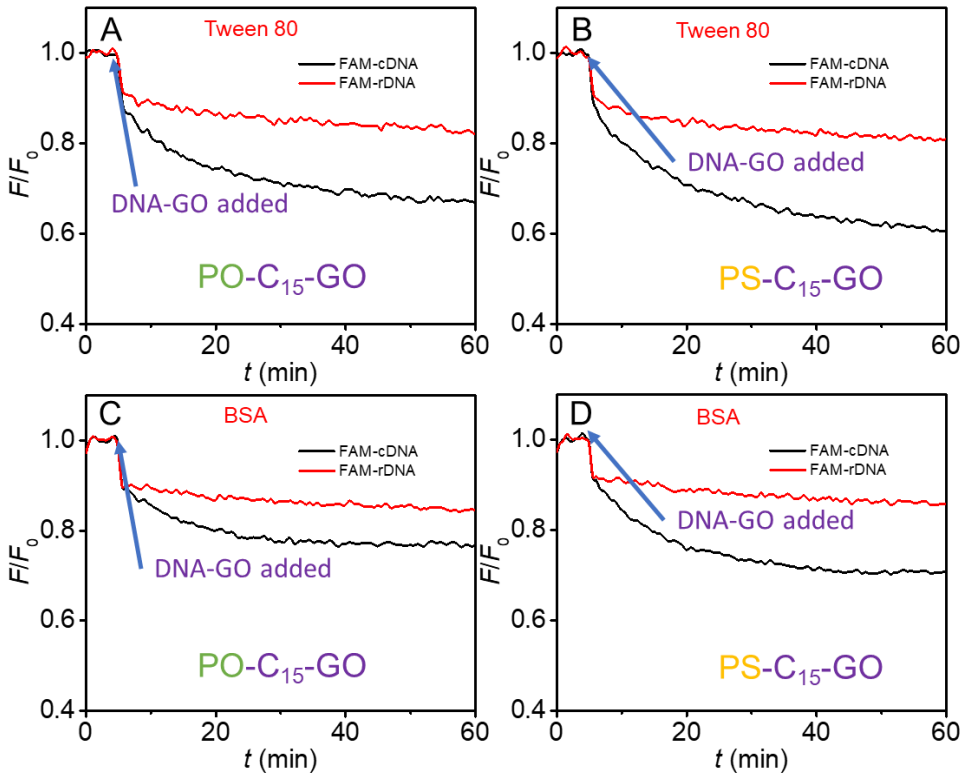

Figure 2.9 Kinetics of specific hybridization by adding FAM-cDNA and non-specific adsorption by adding FAM-rDNA on PO-C_{15}-12mer and PS-C_{15}-12mer pre-modified GO with the existence of 0.5% Tween 80 (A and B) and 0.25 mg/mL BSA (C and D). The arrowheads point to the addition of the GO conjugates.

2.4 Conclusion

In summary, we systematically compared PS and PO DNA for adsorption on GO. PS DNA is known to have stronger affinity to nanomaterials containing thiophilic metals such as AuNPs and quantum dots. Despite its lack of thiophilic metals, GO still adsorbs PS DNA more strongly than the PO DNA of the same sequence. Based on the washing experiments and MD simulations, we attributed this to the stronger VDW force brought by the sulfur atom. By comparing different DNA sequences, we concluded that poly-C DNA with PS modifications has the highest affinity among the sequences we tested so far. This discovery allowed us to construct a more stable diblock DNA. A PS poly-C DNA block can tightly adsorb on the GO surface, allowing the other block to hybridize with the cDNA under various buffer conditions. This study allowed a convenient noncovalent method for modifying GO with DNA. At the same time, it has discovered interesting biointerfacial forces brought by a single atom substitution in DNA. We expect more work to be carried out using modified DNA to interact with inorganic surfaces for developing biosensors and hybrid nanomaterials.

Chapter 3 Mn^{2+}-Assisted DNA Adsorption on Ti_2C MXene Nanosheets

The results presented in this chapter have been published as:

Zhicheng Huang, Biwu Liu and Juewen Liu, Mn^{2+}-Assisted DNA Oligonucleotide Adsorption on Ti_2C MXene Nanosheets. *Langmuir* 2019, 35 (30), 9858-9866.

3.1 Introduction

Inspired by research on graphene,[45, 191] a suite of other 2D nanomaterials have been synthesized such as graphitic-C_3N_4, MoS_2, and WS_2.[192-195] A recent example is 2D transition metal carbide/nitride (MXene).[37] MXene sheets are sheared from the MAX phase, where M is a transition metal, A is an A-group element such as Al, and X is carbon or nitrogen. The M layer is closely packed by carbon or nitrogen, and these packed layers are inserted by the A metal layers. After etching the A layers, 2D MXene can be isolated.[37] Since the etching process always involves HF, the final MXene surface is rich in –F along with –OH and −O− groups. These groups make MXene an interesting platform for surface modification and adsorption. MXene shows promises in catalysis,[60-61, 196] nanomedicine,[197-198] sensing,[63-64, 199-200] and energy conversion.[38, 201] In addition, MXene has excellent adsorption properties for metal ions and small molecules.[59, 65]

Interfacing 2D nanomaterials with DNA has yielded many new hybrids for biosensing applications.[153, 195, 202-204] The best-known example is the adsorption of fluorescently labelled DNA oligonucleotides on graphene oxide (GO) for the detection of complementary DNA or RNA.[46, 49, 149, 205-206] Similar reaction schemes have also been realized on MoS_2,[153, 207] and WS_2.[155, 187] DNA-MXene hybrids were also successfully prepared and used in biosensors.[64, 66-67, 199] For example, Yao and coworkers covalently linked an amino-modified DNA to polyacrylic acid modified Ti_3C_2 MXene for detection of cancer biomarkers.[64, 67] However, no work was performed to explore the fundamental mechanism of DNA interaction with MXene.

Different 2D materials have different surface properties. GO mainly uses π-π stacking and hydrogen bonding to adsorb DNA.[56-57, 206, 208] MoS_2 and WS_2 rely on van der Waals interactions.[154, 187] Given the very different surface chemistry of MXene, it would be interesting to compare these materials with MXene for their adsorption of DNA. In this work, we systematically studied adsorption of DNA oligonucleotides by the Ti_2C MXene and found a unique role of Mn^{2+}. Mn^{2+} ions can help DNA adsorption via its phosphate backbone. In addition, interesting delayed DNA desorption was observed when inorganic phosphate competitively bind to the Mn^{2+} ions in the system. Finally, DNA-induced desorption of DNA was also found to be different on MXene and GO.

3.2 Materials and Methods

3.2.1 **Chemicals**

All the DNA samples were purchased from Integrated DNA Technologies (IDT, Coralville, IA). Carboxyl graphene oxide (GO) and monolayer molybdenum disulfide (MoS_2) were purchased from ACS Material (Medford, MA). All the metal chloride salts were purchased from Sigma-Aldrich (St Louis, MO), or Mandel Scientific (Guelph, ON, Canada). 4-(2-hydroxyethyl) piperazine-1-ethane sulfonate (HEPES), urea, and four nucleosides were from Mandel Scientific. Ethylenediaminetetraacetic acid (EDTA), sodium phosphate monobasic, reduced GSH, Tween 80, and albumin-fluorescein isothiocyanate conjugate (FITC-BSA) were from Sigma-Aldrich. The Ti_2C MXene was supplied by Dr. L. Xiao from Hunan University (Changsha, China) following the published protocols.[209] Milli-Q water was used for preparing buffers and solutions.

Table 3.1 DNA sequences and modifications used in this work.

ID	DNA Names	Sequences 5′-3′
1	FAM-12mer DNA	FAM-TCACAGATGCGT
2	cDNA	ACGCATCTGTGA
3	rDNA	AGAGAACCTGGG
4	FAM-A_5	FAM-AAAAA
5	FAM-A_{10}	FAM-AAAAAAAAAA
6	FAM-A_{15}	FAM-AAAAAAAAAAAAAAA
7	FAM-A_{30}	FAM-AAAAAAAAAAAAAAAAAAAAAAAAAAAAAA
8	FAM-A_{45}	FAM-AAAAAAAAAAAAAAAAAAAAA AAAAAAAAAAAAAAAAAAAAAAAAA
9	FAM-C_5	FAM-CCCCC
10	FAM-C_{10}	FAM-CCCCCCCCCC
11	FAM-C_{15}	FAM-CCCCCCCCCCCCCCC
12	FAM-C_{30}	FAM-CCCCCCCCCCCCCCCCCCCCCCCCCCCCCC
13	FAM-T_5	FAM-TTTTT
14	FAM-T_{10}	FAM-TTTTTTTTTT
15	FAM-T_{15}	FAM-TTTTTTTTTTTTTTT

16	FAM-T_{30}	FAM-TTTTTTTTTTTTTTTTTTTTTTTTTTTTTT
17	A_5	AAAAA
18	A_{10}	AAAAAAAAAA
19	A_{15}	AAAAAAAAAAAAAAA

3.2.2 ζ-Potential measurement

ζ-potential was measured using dynamic light scattering (Zetasizer Nano 90, Malvern). In a typical experiment, GO, Ti_2C MXene (final concentration of 20 μg/mL), and MoS_2 (final concentration of 200 μg/mL) were respectively dispersed in 1 mL buffer (5 mM HEPES, pH 7.5). The ζ-potential values were measured in the presence of various salt concentrations at 25 °C.

3.2.3 Methods for XRD and TEM

XRD measurements were conducted at room temperature on a PANalytical Empyrean diffractometer with Cu-Kα radiation equipped with a PIXcel bidimensional detector. TEM images were taken by Phillips CM10 100 kV transmission electron microscope.

3.2.4 DNA adsorption kinetics and capacity

To measure DNA adsorption kinetics, the background fluorescence was collected from 95 μL FAM-DNA and metal ions mixture in 5 mM HEPES buffer (pH 7.5) for 5 min. Then, 5 μL concentrated material solution was added. The final concentrations for the three 2D nanomaterials were different (20 μg/mL GO, 200 μg/mL Ti_2C MXene, and 200 μg/mL MoS_2 for NaCl assisted DNA adsorption; 20 μg/mL Ti_2C MXene, 20 μg/mL GO, and 200 μg/mL MoS_2 for Mn^{2+} and Mg^{2+} assisted DNA adsorption). The fluorescent intensity was collected by a microplate reader (SpectraMax M3) with excitation at 490 nm and emission at 520 nm. For DNA adsorption capacity study, 20 μg/mL Ti_2C MXene was dispersed in 5 mM HEPES buffer (pH 7.5) followed by sonication for 5 min. Then 1 mM Mn^{2+} and different concentrations of FAM-DNA were added and the samples were incubated at room temperature overnight. At last, the DNA capacity was calculated based on the fluorescence of supernatant in the sample after centrifugation ((F_{total}-$F_{supernatant}$)/F_{total}*$[DNA]_{total}$).

3.2.5 DNA desorption

Several competing or denaturing agents were added to induce DNA desorption. For each sample, a small volume of concentrated agents (less than 5% of the total final volume) was added into DNA-MXene samples (100 nM DNA adsorbed on 20 μg/mL Ti_2C MXene with the help of 1 mM Mn^{2+}) in 5 mM HEPES

buffer, pH 7.5. After 4 h incubation at room temperature, the fluorescence from the desorbed DNA in supernatant after centrifugation was measured by the microplate reader.

3.2.6 **Adsorption of duplex DNA**

The double-strand DNA (dsDNA) was prepared by incubating FAM-12mer DNA (100 nM) with its non-labelled complementary DNA (cDNA) (100 nM) in 300 mM NaCl (5 mM buffer, pH 7.5). In addition, a control sample was prepared by mixing the FAM-12mer DNA with a random sequenced DNA (rDNA). These samples were annealed by heating to 90 °C for 5 min followed by slow cooling to room temperature. The adsorption experiments were conducted in 5 mM HEPES buffer, pH 7.5 with 300 mM NaCl, 1 mM Mn^{2+} and monitored by the microplate reader.

3.2.7 **DNA hybridization**

DNA hybridization experiments were carried out by directly adding cDNA/rDNA into FAM-DNA-nanosheet solutions (5 mM HEPES, pH 7.5, 1 mM Mn^{2+}). No additional salt was added during the hybridization process. The ratio of the concentration of the added DNA to that of the adsorbed DNA on GO/MXene was 15:1.

3.3 Results and Discussion

3.3.1 **Na^+-mediated DNA adsorption**

Our starting material for preparing the Ti_2C MXene was Ti_2AlC, and it had a thick MAX phase (Figure 3.1A). After exfoliation by HF and delamination in DMSO, thin Ti_2C MXene sheets were successfully synthesized as characterized by TEM (Figure 3.1B) and XRD (Figure 3.1C).[210] The detailed preparation steps could be found in the previous paper.[209] The most significant change in the XRD pattern of the Ti_2C MXene phase compared with that of the MAX phase is the presence of a broad (0002) peak at around 10 degrees.[59, 209, 211] A weak (103) peak at ~40 degrees was still observed, suggesting that a small fraction of the MAX phase remained in the sample. Its EDS spectrum also indicates successful removal of the Al layers with only ~2% Al left in the final sample (Figure 3.1D), while the original MAX phase has 20% Al. Depending on the condition of etching, this level of remaining Al is quite common in the literature.[42] Part of the residual Al was in the MAX phase, and the Al atoms associated with the MXene were even less. Overall, TEM and XRD confirmed the 2D layered Ti_2C MXene used for this study.

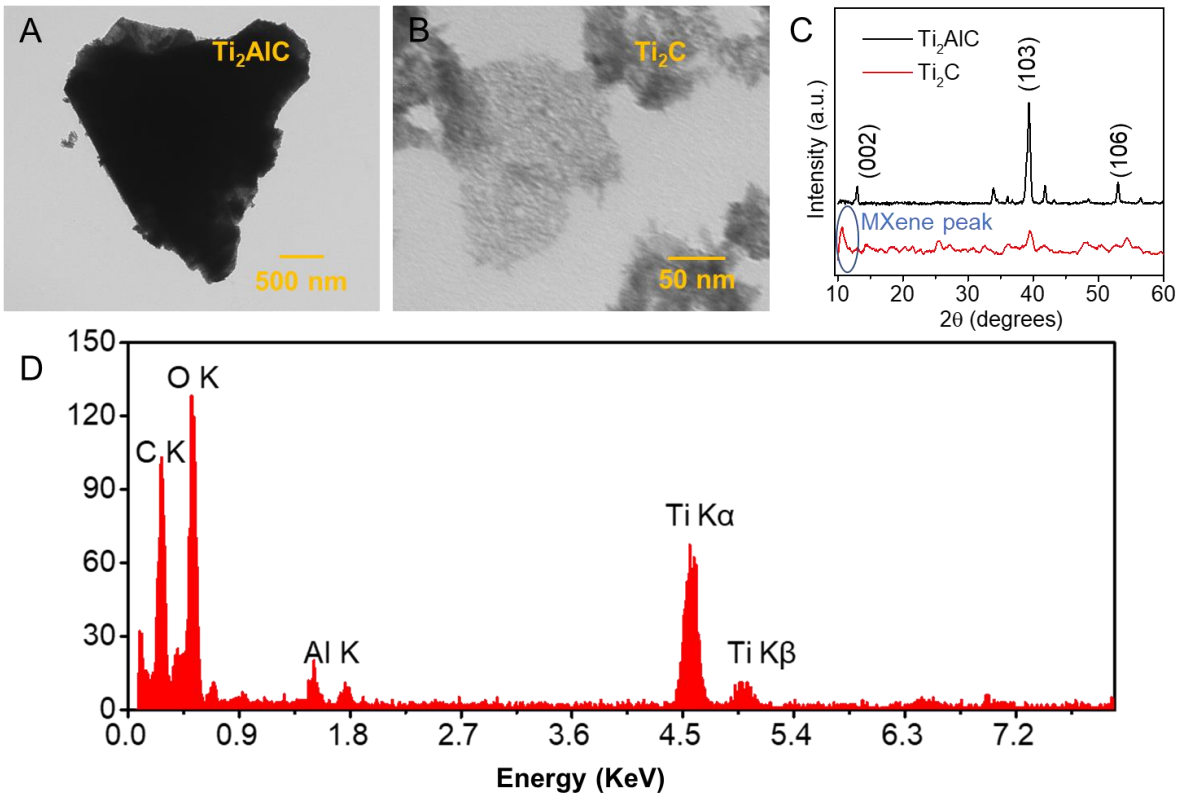

Figure 3.1 TEM micrographs of the (A) Ti_2AlC MAX phase, and (B) Ti_2C MXene nanosheets. (C) XRD spectral changes before (black line) and after (red line) exfoliation of the Ti_2AlC MAX sample (the MXene peak circled in blue). (D) The EDS spectrum of the Ti_2C MXene nanosheets showing the abundant -O groups on MXene surface and the Al layers in Ti_2AlC were successfully etched.[209]

For comparison, GO and MoS_2 were also included in this study. Both materials showed the expected 2D features (Figure 3.2A and B). Another similarity between the three materials is that they are all negatively charged in a pH 7.5 HEPES buffer (Figure 3.2C). The Ti_2C MXene displays an abundance of Ti-O-Ti, Ti-C, and Ti-O according to the XPS characterizations in the former paper.[209] The high electronegativity oxygen atoms make the Ti_2C surface negatively charged at neutral pH.[62, 2124] Since DNA is also strongly negatively charged, the electrostatic repulsion needs to be overcome before DNA adsorption can occur.

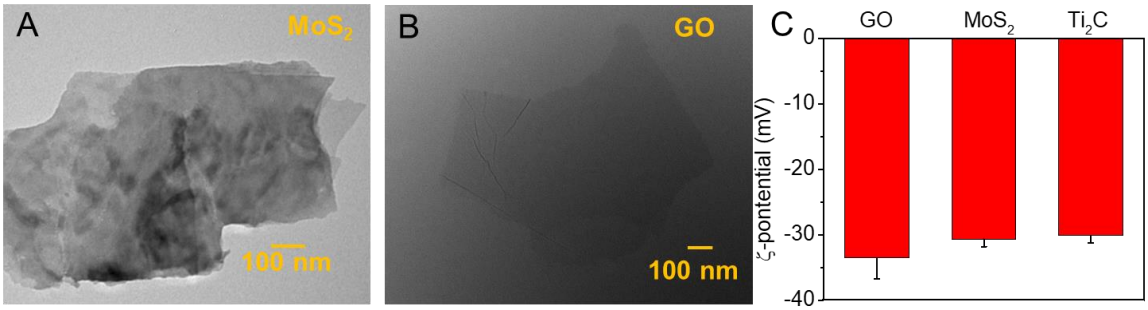

Figure 3.2 TEM micrographs of the (A) MoS_2, and (B) GO used in this work. (C) ζ-potentials of the three 2D nanosheets measured in 5 mM HEPES buffer, pH 7.5.

To study DNA adsorption, the scheme in Figure 3.3A was followed using fluorescently labelled DNA oligonucleotides. Since these 2D nanomaterials are often good fluorescent quenchers,[50, 187] adsorption of DNA was expected to be accompanied with fluorescence quenching. With denaturing or competing molecules, the adsorbed DNA might desorb to yield fluorescence enhancement. Studying DNA desorption can provide insights into the surface forces responsible for DNA adsorption.

When the Ti_2C MXene was added to a FAM-labeled DNA in a salt-free buffer, no fluorescence quenching was observed due to electrostatic repulsion (Figure 3.3B, the black trace). Usually, salt is required to screen charge repulsion between DNA and negatively charged nanomaterials.[9, 2137] The concentration of NaCl was then gradually increased to 300 mM, but still, little fluorescence quenching was observed. Since the Ti_2C MXene is a strong fluorescence quencher,[66] this indicated that NaCl did not promote DNA adsorption. In contrast, NaCl promoted DNA adsorption on both GO and MoS_2 (Figure 3.3C and D). In addition, a high salt concentration might lead to aggregation of nanomaterials, and aggregated MXene might hinder DNA adsorption.

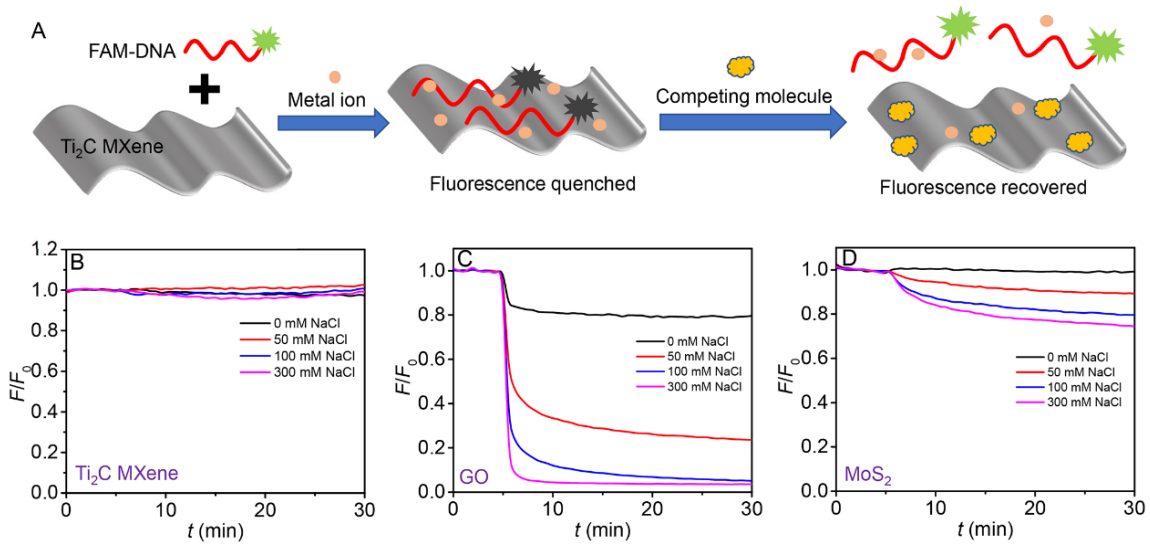

Figure 3.3 (A) A scheme of adsorption of a FAM-labeled DNA on the Ti_2C MXene with quenched fluorescence, and its subsequent desorption induced by competing molecules with fluorescence recovery. Kinetics of adsorption of the FAM-12mer DNA (100 nM) on (B) 200 µg/mL Ti_2C MXene, (C) 20 µg/mL GO, and (D) 200 µg/mL MoS_2 in the presence of different concentrations of NaCl in 5 mM HEPES buffer (pH 7.5).

In order to evaluate the effect of aggregation, we first compared the colloidal stability of our materials in 5 mM HEPES buffer without and with 300 mM NaCl (Figure 3.4A). All the samples were stable within 30 min. After 6 h incubation, sedimentation occurred, but no obvious difference in the speed of sedimentation was observed. Furthermore, we either pre-incubated each material with 300 mM NaCl for 6 h, or freshly dispersed them in 300 mM NaCl, and then measured DNA adsorption. Potential salt-induced aggregation of these nanomaterials did not affect DNA adsorption (Figure 3.4B). Therefore, we can focus on the effect of salt on electrostatic interactions and the potential effect on aggregation can be neglected.

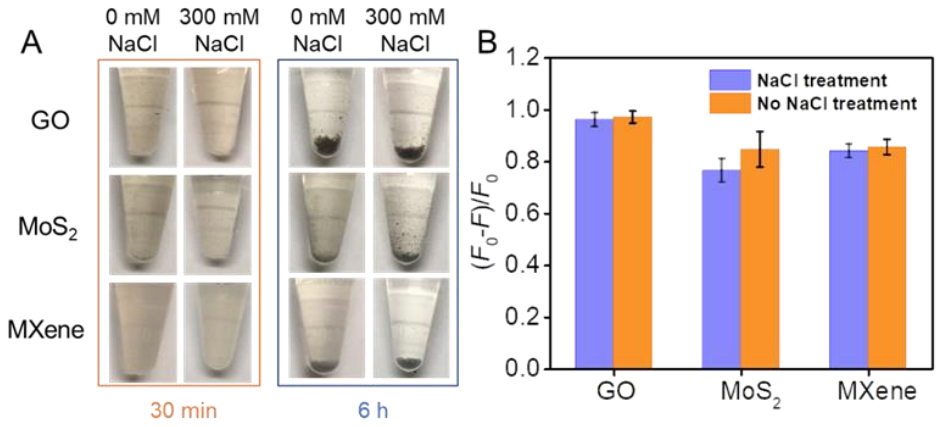

Figure 3.4 (A) Photographs of the three nanomaterials (200 μg/mL for MoS_2 and MXene, 20 μg/mL for GO) without and with 300 mM NaCl after 30 min and 6 h standing at room temperature. Adding 300 mM NaCl had little effect on the aggregation state of the materials. (B) 100 nM FAM-12 mer DNA adsorption on the three nanomaterials (200 μg/mL for MoS_2, 20 μg/mL for GO and MXene) without (orange bars) and with (blue bars) pre-incubation of the materials with 300 mM NaCl. All of the samples were added with 1 mM Mn^{2+} to promote DNA adsorption.

Since 300 mM NaCl did not help DNA adsorption, screening charge repulsion alone was not enough for Ti_2C MXene, which might be due to a lack of strong attraction forces. GO can attract DNA via π-π stacking and hydrogen bonding.[49] WS_2 and MoS_2 can adsorb DNA via van der Waals (VDW) forces.[187] Although VDW forces should also exist for the Ti_2C MXene, the lack of DNA adsorption indicates this force is weaker for the MXene. The surface groups (e.g. -OH) might prevent the DNA from contacting the heavy atoms on the Ti_2C surface (thus lower VDW force).

3.3.2 **Mn^{2+}-mediated DNA adsorption**

With high electronegativity surface groups on the Ti_2C MXene, we reasoned that adding polyvalent metal ions might promote DNA adsorption. For example, Ca^{2+} promotes DNA adsorption on polydopamine nanoparticles,[214] and on lipid bilayers.[2159] To test this hypothesis, various monovalent, divalent, and trivalent metal ions were screened. These metal ions were first mixed with the FAM-labelled DNA. Except for Mn^{2+}, strong quenching was observed with most of the first-row transition metals (Figure 3.5A, the top row). In addition, Sc^{3+} seemed to precipitate the DNA, but the precipitant remained strongly fluorescent. To these metal/DNA mixtures, the Ti_2C MXene was then added (the bottom row). After centrifugation, to precipitate the adsorbed DNA, the effect of adsorption by MXene was most obvious with Mn^{2+}, Ni^{2+}, and Ca^{2+}. Therefore, these metal ions might promote DNA adsorption. The adsorption efficiencies were quantified (Figure 3.5B), and Mn^{2+} was the most effective metal (nearly 90% DNA adsorbed). Ni^{2+} was excluded in further studies since it quenched the fluorescence of the DNA (Figure 3.5C).

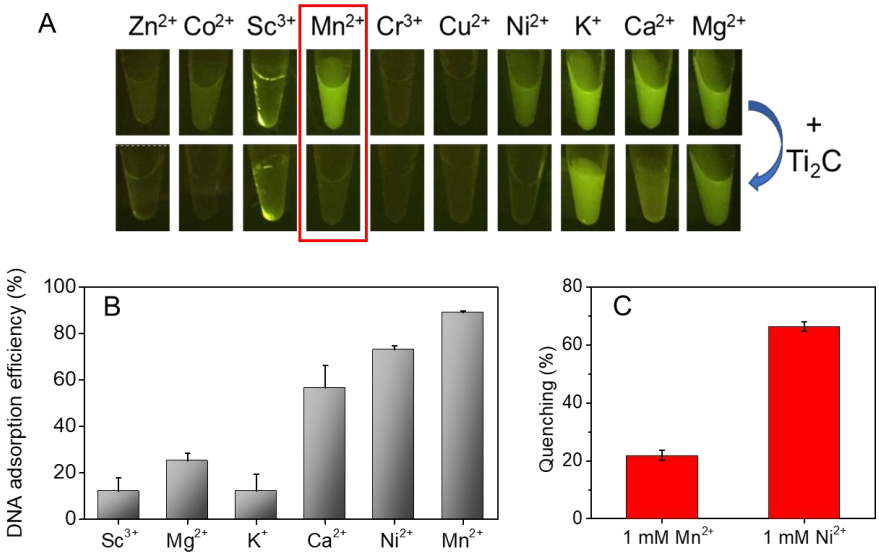

Figure 3.5 (A) Fluorescent photographs of 100 nM FAM-12mer DNA mixed with 1 mM different metal ions without or with 20 μg/mL Ti_2C MXene. (B) Percentage of DNA adsorbed on the Ti_2C MXene in the presence of different metal ions (1 mM each). (C) Fluorescence quenching efficiency of the FAM-12mer DNA (100 nM) by 1 mM Mn^{2+} or Ni^{2+}. Ni^{2+} is a much stronger quencher. The measurement was performed in 5 mM HEPES, pH 7.5.

A few interesting observations were made from this experiment. Firstly, Mn^{2+} and Ni^{2+} both promoted DNA adsorption, and thus transition metals might be effective in general. Other metals, such as Zn^{2+}, Co^{2+}, and Cu^{2+} might also promote DNA adsorption, but they strongly quenched the fluorescence of FAM, and their promoting effects were less obvious. Secondly, for group 2A metals, Ca^{2+} was more effective than Mg^{2+}. Similar observations were also made with DNA adsorption by polydopamine nanoparticles.[214] Finally, trivalent Sc^{3+} precipitated the DNA in the buffer, while adding the Ti_2C MXene did not have much further quenching. For practical applications, Mn^{2+} appears to be most useful since it minimally interfered with the fluorescence, yet still significantly boosted DNA adsorption.

To understand the role of Mn^{2+}, the ζ-potentials of these 2D materials were measured after adding various metal ions. With 20 μg/mL Ti_2C MXene (Figure 3.6A), 1 mM Mn^{2+} fully neutralized its surface charge. While the sample remained negatively charged with 1 mM Mg^{2+} or Ca^{2+}. In contrast, Mn^{2+}, Ca^{2+}, and Mg^{2+} were similar in screening the charges on GO and MoS_2. Adding more Mn^{2+} (e.g. 2 mM) turned the surface of Ti_2C MXene to positive (Figure 3.6B). Thus, Mn^{2+} adsorbed Ti_2C MXene to significantly decrease charge repulsion between DNA and Ti_2C MXene. With a high concentration of Mn^{2+}, DNA can interact with the MXene via electrostatic attraction.

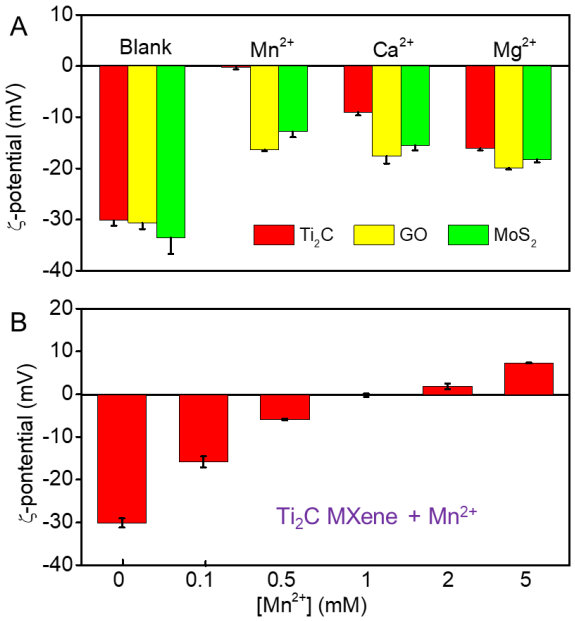

Figure 3.6 (A) The ζ-potentials of the three 2D nanosheets in the presence of 1 mM Mn^{2+}, Ca^{2+}, or Mg^{2+}, where Mn^{2+} fully neutralized the MXene surface. (B) The ζ-potential of the Ti_2C MXene as a function of Mn^{2+} concentration. All the ζ-potentials were measured in 5 mM HEPES buffer, pH 7.5.

3.3.3 **Effect of Mn^{2+} on DNA adsorption kinetics**

After identifying that Mn^{2+} can promote DNA adsorption, the kinetics of DNA adsorption were studied (Figure 3.7). Mg^{2+} was also tested to compare with Mn^{2+}. The background fluorescence of the FAM-12mer DNA was first monitored for 5 min, and then various nanomaterials were added. For all these materials, Mn^{2+} was more effective than Mg^{2+} to promote DNA adsorption. The relative difference between Mn^{2+} and Mg^{2+} was the largest on the Ti_2C MXene. This might be due to the neutralized or even inversed surface charge of Ti_2C with Mn^{2+} converting electrostatic repulsion to attraction.

Mn is a typical siderophile element, meaning Mn^{2+} has a higher affinity for oxygen than to sulfur. GO and the Ti_2C MXene are both rich in surface oxygen groups. As a result, Mn^{2+} effectively promoted DNA adsorption on them (Figure 3.7A and B). On the other hand, MoS_2 has sulfur on the surface. The fastest DNA adsorption kinetics and efficiency were observed on GO in the presence of Mn^{2+} (despite the surface of GO remaining negatively charged under this condition), and this suggested very strong attraction forces. The π-π stacking between DNA nucleobases and GO might be the reason (Figure 3.7B), and this interaction is not available for MoS_2 or the Ti_2C MXene.

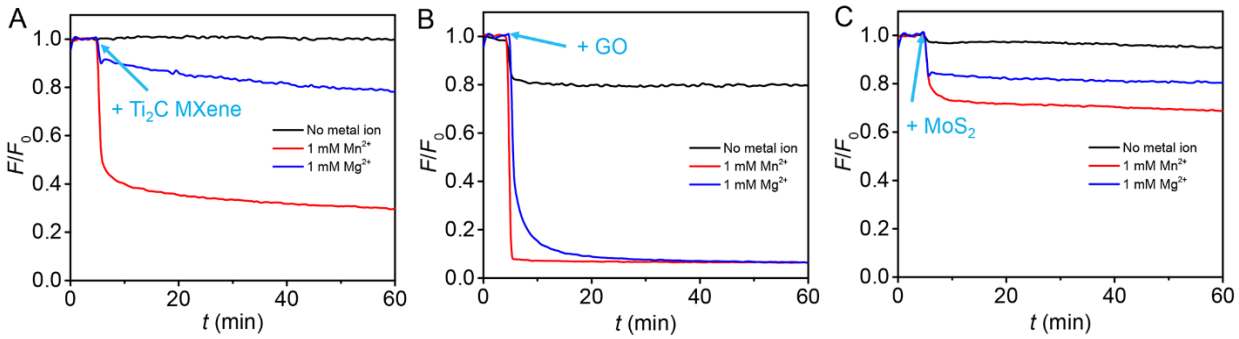

Figure 3.7 Adsorption kinetics of 100 nM of the FAM-12mer DNA on (A) 20 μg/mL Ti_2C MXene, (B) 20 μg/mL GO, and (C) 200 μg/mL MoS_2 in the presence of 1 mM Mn^{2+} or 1 mM Mg^{2+} in 5 mM HEPES buffer pH 7.5.

3.3.4 **DNA adsorption capacity**

After understanding adsorption kinetics, we then studied DNA adsorption capacity. The adsorption capacity was measured using the FAM-12mer DNA. The adsorbed DNA was quantified after centrifugation and measurement of the fluorescence in the supernatants. With 20 μg/mL Ti_2C MXene and 1 mM Mn^{2+}, the DNA was nearly fully adsorbed when its concentration was below 150 nM (Figure 3.8A inset). The data was fitted to a Langmuir adsorption isotherm and the saturated DNA adsorption concentration was 298 nM (Figure 3.8A). This capacity is much higher than that from a previous report (< 0.2 nM DNA per 20 μg/mL Ti_3C_2 MXene).[66] In that paper, DNA adsorption was performed without salt, and the higher capacity here was attributed to Mn^{2+}. The Langmuir isotherm here suggests that DNA adsorption was monolayer.

The effect of Mn^{2+} concentration on DNA adsorption was then studied (Figure 3.8B). Excess FAM-12mer DNA (500 nM) was mixed with 20 μg/mL Ti_2C MXene in the presence of various concentrations of Mn^{2+}. The amount of adsorbed DNA increased roughly linearly with up to 0.5 mM Mn^{2+}, after which, DNA adsorption was less dependent on Mn^{2+}. The data was fitted to a binding curve with an apparent dissociate constant (K_d) of 0.074 mM Mn^{2+}. Overall, 1 mM Mn^{2+} was sufficient to help DNA adsorption and was used for most of the experiments in this work.

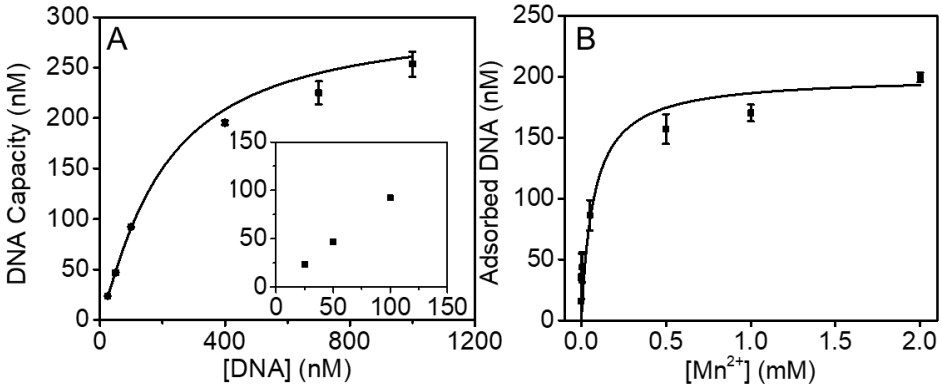

Figure 3.8 (A) An adsorption isotherm of the FAM-12mer DNA on 20 μg/mL Ti_2C MXene in the presence of 1 mM Mn^{2+} (inset: DNA nearly fully adsorbed at low DNA concentrations). (B) DNA adsorption capacity in the presence of various concentrations of Mn^{2+}.

After understanding the role of Mn^{2+}, the effect of DNA length was studied. A series FAM-labeled poly-A oligonucleotides were used (Figure 3.9A). DNA adsorption capacity increased with DNA length when the DNA was shorter than 15-mer. Since longer DNA was likely to occupy more footprint on the surface, its higher capacity indicated that longer DNA had a stronger affinity to the Ti_2C MXene. Further elongating the DNA to A_{30} and A_{45} decreased the capacity, suggesting that the adsorption stability was sufficient for the 15-mer DNA. Using even longer DNA only occupied more space on the surface. A similar drop in DNA adsorption density was also observed for poly-C and poly-T DNA (Figure 3.9B and C).

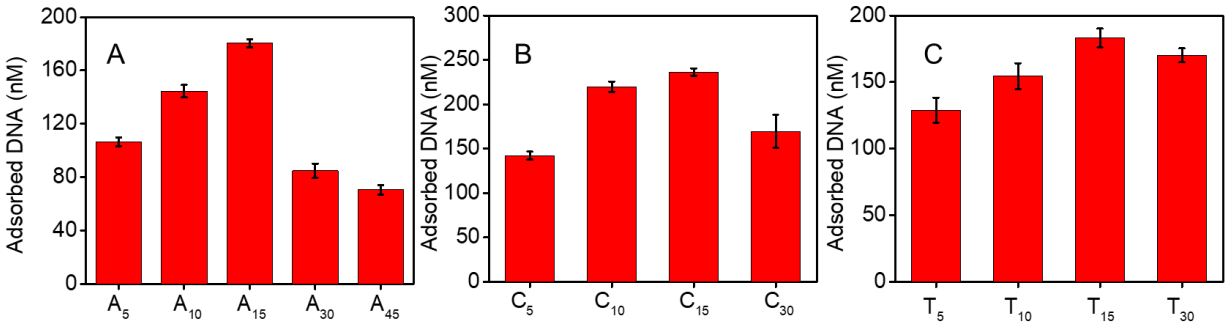

Figure 3.9 DNA adsorption capacity as a function of the length of (A) poly-A, (B) poly-C, and (C) poly-T oligonucleotides on 20 μg/mL Ti_2C MXene in 5 mM HEPES buffer, pH 7.5, and 1 mM Mn^{2+}.

The stronger affinity of longer DNA to Ti_2C MXene was tested by a desorption experiment. We pre-adsorbed 100 nM FAM-A_{15} DNA on 20 μg/mL Ti_2C MXene, and non-labeled poly-A DNA of different lengths were added. More FAM-DNA was displaced by longer poly-A DNA, confirming higher affinity of

longer DNA (Figure 3.10). In addition, it indicated that the DNA likely adsorbed lengthwise on the surface instead of standing up perpendicularly.

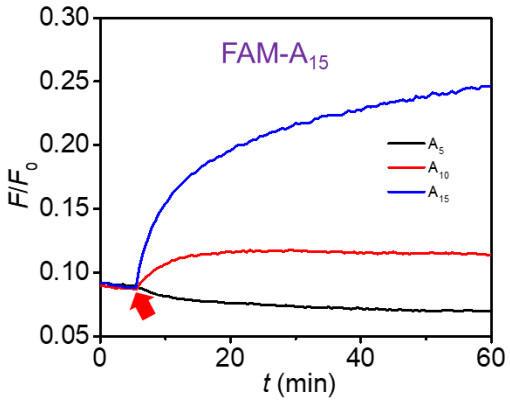

Figure 3.10 Kinetics of FAM-A_{15} DNA adsorption from Ti_2C MXene by poly-A oligonucleotides of different lengths (1 μM each). The red arrow points the addition of the non-labeled poly-A DNA.

3.3.5 **DNA desorption**

Thus far, the importance of Mn^{2+} has been confirmed. We then wanted to understand its chemical role for DNA adsorption. For this purpose, desorption of DNA was studied. First, inorganic phosphate was used as a competitor to perturb the interaction between DNA phosphate backbone and the Ti_2C MXene. Nearly 90% of the adsorbed DNA desorbed from the Ti_2C MXene with 5 mM phosphate in 30 min (Figure 3.11B). This suggests that Mn^{2+} might be interacting with the phosphate backbone of the DNA. In contrast, little DNA desorbed from GO (Figure 3.11C) or MoS_2 (Figure 3.11D) by phosphate, since their main interactions were independent of the phosphate backbone of DNA.[150, 187]

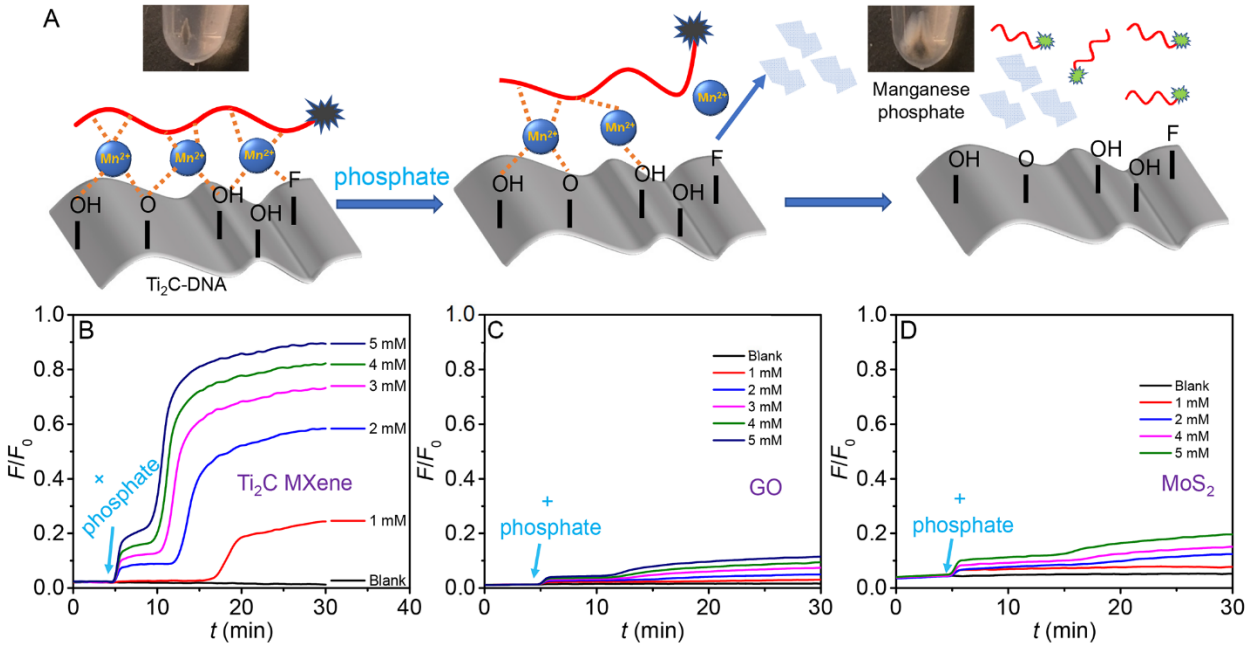

Figure 3.11 (A) A model showing inorganic phosphate induced delayed release of DNA from the Ti_2C Mxene by extracting Mn^{2+} and forming manganese phosphate. The photograph on the left shows the sample before adding phosphate, and the one on the right shows the precipitated manganese phosphate. Kinetics of the FAM-12mer DNA desorption from (B) Ti_2C MXene, (C) GO, and (D) MoS_2 induced by 1-5 mM phosphate (the arrows point the addition of phosphate).

For all these materials, a delay between fluorescence recovery and the addition of phosphate was noticed. This delay was particularly obvious for the Ti_2C MXene sample (Figure 3.11A). The lower the phosphate concentration, the longer the delay time. For GO and MoS_2, such delays were not observed previously. Since this study included 1 mM Mn^{2+}, while previous studies mainly used Na^+ or Mg^{2+}, we suspected that the reaction between phosphate and Mn^{2+} might be responsible for the delay. To test this hypothesis, we did a few control experiments. If the DNA-nanosheets were washed to remove the free Mn^{2+}, the delay no longer occurred (Figure 3.12A-C). The delays did not occur with other ions (e.g., Ni^{2+} and Ca^{2+} in Figure 3.12D and E). Therefore, the delays were indeed related to Mn^{2+}.

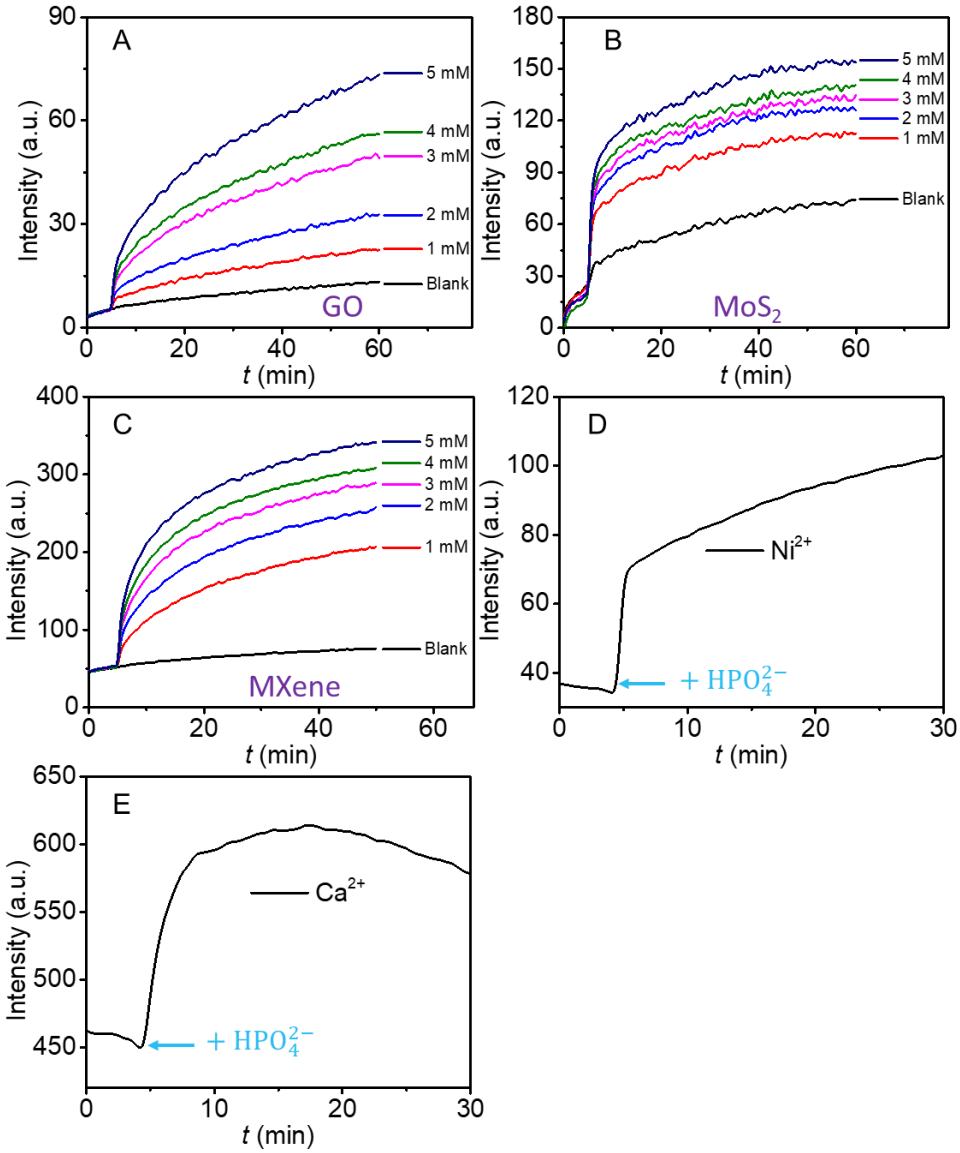

Figure 3.12 DNA desorption kinetics on washed (A) GO, (B) MoS_2, and (C) MXene 2D nanosheets induced by 1-5 mM phosphate. The washing step was performed by centrifugation (once), removal of the supernatant and redispersing the precipitants in 5 mM HEPES, pH 7.5. Kinetics of desorption of the FAM-12mer DNA from the Ti_2C MXene induced by 5 mM phosphate. The FAM-12mer DNA (100 nM) was adsorbed on the Ti_2C MXene (20 μg/mL) by in the presence of (D) 1 mM Ni^{2+} or (E) 1 mM Ca^{2+}.

After adding phosphate, white precipitants were observed in the test tubes (see the photographs in Figure 3.11A). From TEM images, a new type of material was observed, which was identified to be manganese phosphate from XRD (Figure 3.13).[216] Together, the delay was due to the formation of manganese phosphate nanocrystals. However, DNA has a very weak affinity to manganese phosphate,[217] and it is unlikely that the DNA was adsorbed on the newly formed manganese phosphate.

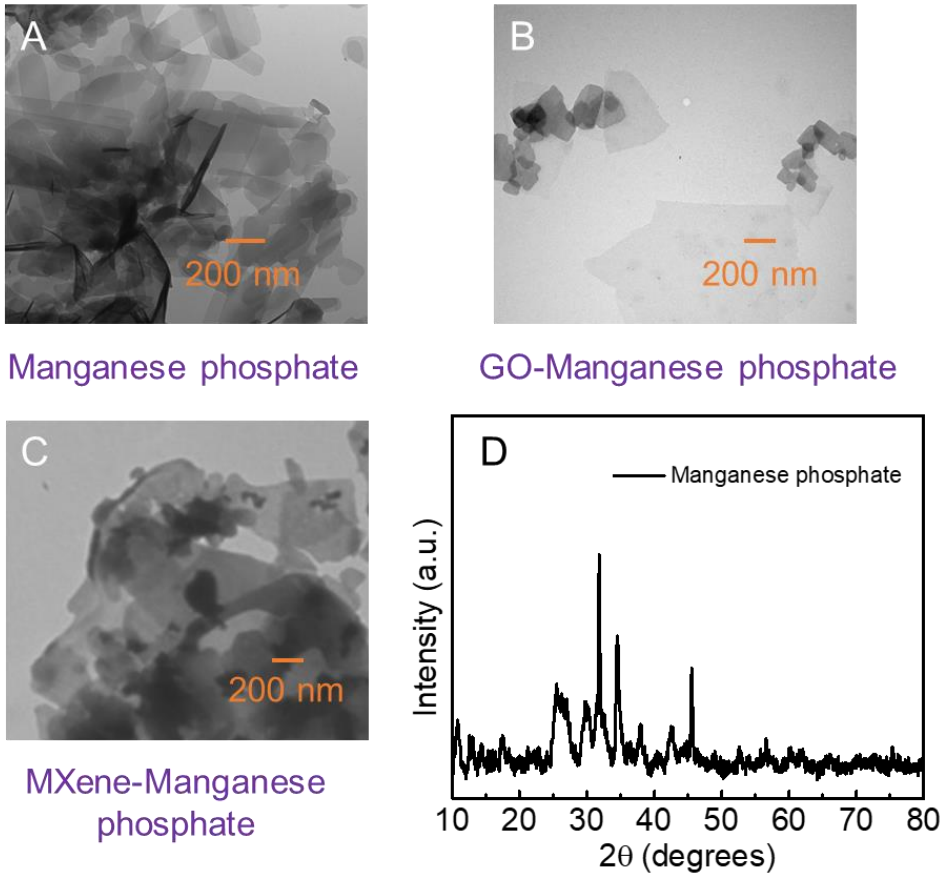

Figure 3.13 TEM micrographs of (A) manganese phosphate, (B) GO-manganese phosphate, and (C) MXene-manganese phosphate. (D) XRD pattern of the precipitant after adding 50 mM phosphate to the 10 mM Mn^{2+} containing MXene sample. The positions of the four peaks located between 25 and 35 degrees match well with the literature.[216]

Mn^{2+} is critical for DNA adsorption on these nanomaterials, especially for the MXene. When Mn^{2+} was washed away, the DNA could not be stably adsorbed on the Ti_2C MXene (Figure 3.14). Formation of manganese phosphate can take away Mn^{2+} from the system, and the delay time reflected the formation of manganese phosphate.

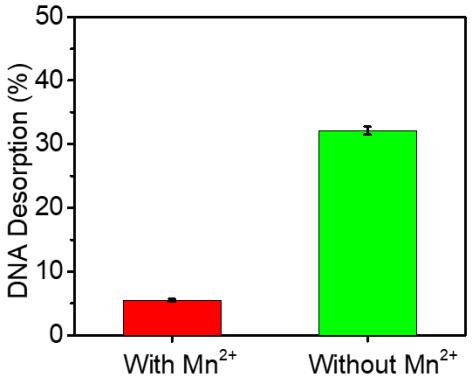

Figure 3.14 More DNA was released from the washed Ti_2C MXene samples in 5 mM HEPES buffer without Mn^{2+} (green bar) after overnight standing. Red bar represented the DNA released from the washed Ti_2C MXene samples which were redispersed in 5 mM HEPES, pH 7.5, and 1 mM Mn^{2+}.

Based on the above data, a model is presented to show DNA desorption from Ti_2C MXene induced by phosphate (Figure 3.11A). Manganese phosphate crystals were formed on the surface of Ti_2C MXene or in solution, and this process gradually extracted Mn^{2+} from the DNA. The more phosphate added, the faster formation of the crystals, and the shorter the delay time. For GO and MoS_2, Mn^{2+} acts as a general electrolyte for charge screening, and the decrease of Mn^{2+} concentration in solution can also adversely affect DNA adsorption. However, for these two surfaces, Mn^{2+} was less critical for DNA adsorption, and much less DNA desorbed.

Apart from the phosphate backbone, DNA may also use its nucleobases for adsorption. To probe its effect, 1 mM of the four nucleosides were added, but almost no DNA was desorbed by guanosine, cytidine, and thymidine from the Ti_2C MXene (Figure 3.15). Very little adsorbed DNA can be released by 1 mM adenosine. Therefore, the effect of Mn^{2+} is mainly between DNA phosphate backbone and Ti_2C MXene.

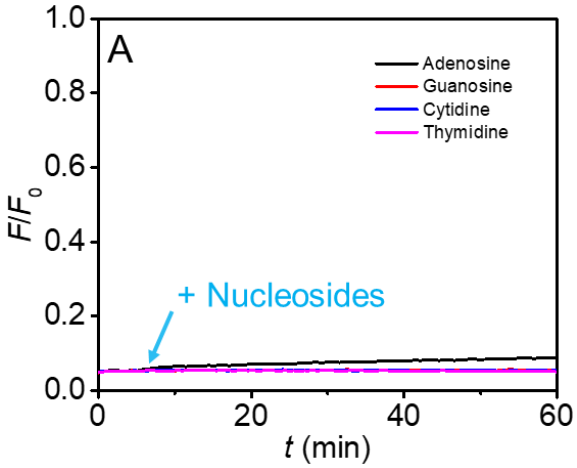

Figure 3.15 FAM-12mer DNA desorption kinetics induced by 1 mM four nucleosides.

3.3.6 **Stability of DNA adsorption**

For most applications, the stability of DNA adsorption is important. The above studies probe DNA adsorption in the presence of phosphate and nucleosides. To further understand the stability of our Mn^{2+} mediated adsorption, a few other chemicals were also added to desorb the FAM-12mer DNA from the Ti_2C MXene (Figure 3.16). A surfactant, Tween 80, was chosen to probe VDW forces between DNA and Ti_2C MXene. Less than 20% of the DNA desorbed by 0.2% Tween 80 indicated that VDW forces may not be important. With 4 M urea, only around 10% of the DNA was released, suggesting that hydrogen bonding was not important either. Finally, GSH and EDTA were added. It was reported that the GSH has moderate interactions with Mn^{2+},[218] but only less than 10% of the DNA was released with 10 mM GSH. On the other hand, EDTA can more strongly chelate Mn^{2+}, and nearly 60% of the DNA desorbed by 10 mM EDTA. Therefore, the Mn^{2+} mediated DNA adsorption can survive GSH but not stronger ligands such as EDTA and phosphate.

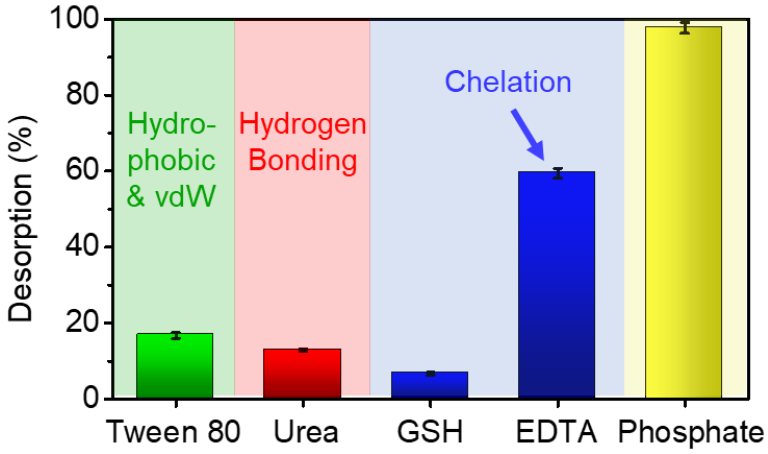

Figure 3.16 Desorption of the DNA from the Ti_2C MXene in 5 mM HEPES buffer with 1 mM Mn^{2+} induced by various competing molecules (0.2% Tween 80, 4 M urea, 10 mM GSH, 10 mM EDTA, or 5 mM phosphate with 4 h incubation).

3.3.7 **DNA-induced DNA desorption**

We then tested DNA-induced desorption. Based on the scheme in Figure 3.3A, if the adsorbed DNA can be selectively desorbed in the presence of its complementary DNA (cDNA), this method might be used to detect the cDNA. Such a detection scheme has been realized on many materials, and the most well-known example is on GO.[46, 49, 149, 205-206] To test this, the cDNA or a random DNA (rDNA) was added to displace the adsorbed FAM-12mer DNA from the Ti_2C MXene. Surprisingly, the cDNA and rDNA desorbed a similar amount of the FAM-12mer DNA (Figure 3.17). In contrast, the cDNA desorbed more DNA from GO, consistent with the literature report.[46] The data in Figure 3.17 indicate that the unmodified MXene might not be a good surface for direct detection of DNA.

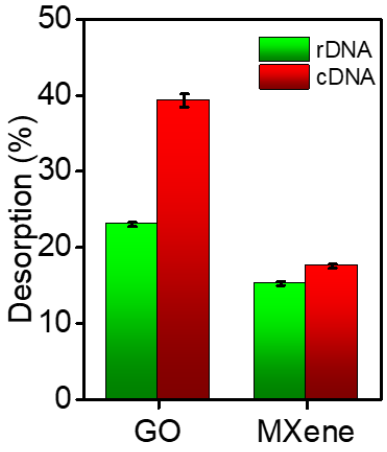

Figure 3.17 The FAM-12mer DNA desorption on GO and Ti_2C MXene induced by 1.5 μM rDNA or cDNA.

3.3.8 **Adsorption of double-stranded DNA**

To understand why the cDNA and rDNA showed little difference in desorbing the FAM-12mer DNA above, we compared adsorption of single- and double-stranded DNA. The FAM-12mer DNA was hybridized with its complementary DNA (cDNA) to form a double-stranded DNA (dsDNA). As a control, another sample was prepared by adding a non-complementary (rDNA), and we called it ssDNA. The adsorption kinetics of the three DNA samples (FAM-12mer DNA, dsDNA, and ssDNA) on the Ti_2C MXene were followed in the presence of 1 mM Mn^{2+} (Figure 3.18). Interestingly, the FAM-12mer DNA and dsDNA samples showed similar adsorption kinetics, while adsorption of the ssDNA sample was about 50% less. In this experiment, the concentration of the FAM-12mer DNA was the same.

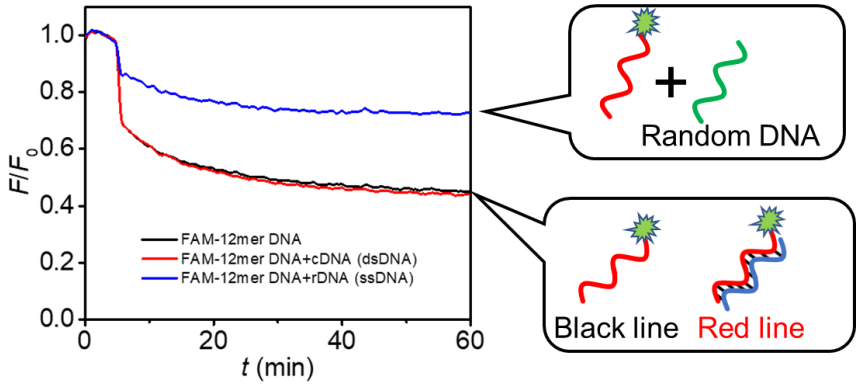

Figure 3.18 The adsorption kinetics of FAM-12mer DNA, dsDNA, and ssDNA on 20 μg/mL Ti_2C MXene in the presence of 1 mM Mn^{2+}. The concentration was 100 nM for the FAM-12mer DNA, and 100 nM for the cDNA or the ssDNA.

In a dsDNA, its bases are shielded in the duplex, but the phosphate backbone is exposed. As a result, the dsDNA could still adsorb on Ti_2C MXene. The similar adsorption kinetics between the dsDNA and the ssDNA indicated the importance of its phosphate backbone for adsorption. Many other surfaces such as GO and AuNPs can achieve this since they rely on DNA base for adsorption.[46, 49, 149, 205-206] Although many metal oxide nanoparticles also adsorb DNA phosphate backbone, they can still tell the difference between single and double-stranded DNA.[49] This MXene is a rare example that can hardly distinguish single and double stranded DNA. The 2D surface feature of MXene, its unique Mn^{2+}-mediated adsorption for neutralizing charge repulsion may contribute to this difference.

This experiment also indicates that we cannot use the Ti_2C MXene to distinguish single-stranded from double-stranded DNA. Although a few studies employed DNA-functionalized MXene, none of them mentioned the application of sequence-specific DNA or RNA detection on unmodified MXene.[66,67] The similar adsorption of single and double stranded DNA on MXene could make it difficult for such applications.

3.4 Conclusion

In summary, Mn^{2+} was identified to promote DNA adsorption onto unmodified Ti_2C MXene nanosheets, and its non-quenching property also makes it attractive for applications. Among Mn^{2+}, Ca^{2+}, and Mg^{2+}, only Mn^{2+} could neutralize the negative charges on the Ti_2C MXene, while none of these metal ions neutralized the charge on GO or MoS_2, indicating unique strong interactions between Mn^{2+} and the MXene. With a higher concentration of Mn^{2+}, the ζ-potential of Ti_2C MXene could be positive, which permits electrostatic interactions between DNA and Ti_2C MXene. A high DNA adoption capacity (298 nM) on 20 μg/mL Ti_2C MXene was reached with Mn^{2+}, much higher than the previously reported Mn^{2+}-free samples.[66] Inorganic phosphate ions can desorb DNA from the Ti_2C MXene with an interesting delayed response. The delay in DNA desorption was attributable to the formation of manganese phosphate crystals. This indicates that Mn^{2+} mediates DNA adsorption via its phosphate backbone, while neither VDW forces nor hydrogen bonding contributed much for DNA adsorption. Finally, the cDNA and random DNA induced similar desorption of the adsorbed DNA, suggesting that unmodified MXene might not be directly useful for DNA detection. Overall, MXene has many interesting surface properties for interfacing with DNA, and it is distinctly different from GO and MoS_2 when it comes to interactions with DNA.

Chapter 4 A High Local DNA Concentration for Nucleating a DNA/Fe Coordination Shell on Gold Nanoparticles

The results presented in this chapter have been published as:

Zhicheng Huang, Biwu Liu and Juewen Liu, A High Local DNA Concentration for Nucleating a DNA/Fe Coordination Shell on Gold Nanoparticles. *Chem. Commun.* 2020, 56 (30), 4208-4211.

4.1 Introduction

Metal coordination with biomolecules is an interesting and convenient way to build biocompatible materials under mild conditions.[88, 90, 219-223] A classic example is to mix trivalent lanthanides with nucleotides forming coordination nanoparticles.[97] Over the last decade, various metal ions have been used such as Ag^{+},[224] Au^{3+},[93] Zn^{2+},[225-226] Cu^{2+},[227] and Fe^{3+}.[100] They form nanoparticles,[228-230] hydrogels,[86, 226, 231] and fibers[94, 231-232] with various nucleobases and nucleotides, and were used for luminescent materials,[95, 97, 233-235] nanozymes,[236-237] encapsulation,[225, 238] and drug delivery.[239-240]

Recently, individual nucleotides have been extended to DNA, and DNA/Fe hybrid nanoparticles were synthesized taking advantage of Fe^{2+} coordination with the DNA.[87, 89, 241] These DNA/Fe nanoparticles showed excellent stability and great promises in drug delivery and bio-imaging.[89, 98, 241-242] However, this reaction required a high concentration of DNA (e.g. 25 μM of DNA oligonucleotides and 1 mM Fe^{2+}). Since the reaction took place in a homogeneous solution, it is difficult to control the growth process, such as the size of the nanoparticles.

Since 1996, DNA-functionalized nanomaterials,[6, 18, 44, 79, 141, 145] especially DNA-functionalized gold nanoparticles (AuNPs) have been widely applied in drug delivery, sensing, catalysis, and directed assembly.[18, 117, 214, 243-245] We reason that growing a DNA/Fe shell on DNA-AuNP conjugates might solve some of the above problems and bring in additional advantages. First, DNA-functionalized AuNPs have a very high localized DNA density, which may favor the local growth of a shell even with an overall low average concentration of DNA. Second, the DNA/Fe shell might be more tunable. Third, the optical properties of AuNPs could extend potential applications in colorimetric sensing. Herein, we communicate that an overall nanomolar of DNA was sufficient and the thickness of the DNA/Fe shell could be tuned from 5 nm to 40 nm. The product showed redshifted plasmon peaks of the AuNPs, which can shift back with the addition of phosphate to etch the shell for colorimetric sensing.

4.2 Materials and Methods

4.2.1 Chemicals

The SH-DNA (5'-TCACAGATGCGTAAAAA-SH-3') was purchased from Integrated DNA Technologies (IDT, Coralville, IA). $FeCl_2 \cdot 4H_2O$ was purchased from Alpha Aesar. Ethylenediaminetetraacetic acid (EDTA), sodium phosphate monobasic, doxorubicin hydrochloride (DOX), $HAuCl_4$, and KCN were purchased from Sigma-Aldrich. AuNPs (13 nm diameter) were synthesized following the procedure in the literature.[213] Based on an extinction coefficient of 2.7×10^8 liter $mol^{-1} \cdot cm^{-1}$ at $\lambda = 520$ nm for 13 nm AuNP, the stock concentration of 13 nm AuNP was 9.67 nM.[246]

4.2.2 AuNP@DNA preparation

The SH-DNA (final concentration 4 μM) was mixed with the AuNP solution (9.67 nM) and incubated under room temperature for 1 h. Then, the DNA-AuNP mixture was incubated in a -20 °C refrigerator for 12 h to freeze. No salt or additional buffer was added for attaching the DNA onto the AuNPs by the freezing method.[25] The obtained conjugate was named AuNP@DNA. For most experiments, the free DNA strands that were not attached were not removed. In some control experiments, to remove the free DNA, the frozen sample was thawed at room temperature and centrifuged at 10000 rpm for 10 min. The supernatant was removed and the pellet was re-dispersed in the same volume of Milli-Q water.

4.2.3 Quantification of the adsorbed DNA on AuNP

In our experiments, the DNA adsorption densities were mainly determined by fluorescent signal. AuNPs are excellent fluorescence quenchers, yielding a large change in fluorescence signal upon fluorescently labeled DNA (FAM-DNA) adsorption/desorption. For FAM-labeled DNA, the quantification was performed by determining the fluorescence intensity of the diluted KCN-treated sample with a plate reader (Infinite F200 Pro, Tecan). The adsorption capacities of DNAs in our experiments will be given by comparing the fluorescence intensity of samples with a standard curve following literature reported procedures.[247]

4.2.4 AuNP@DNA/Fe preparation

The above prepared AuNP@DNA was used. A Fe^{2+} solution was prepared freshly with Milli-Q water at a concentration of 100 mM. To avoid the oxidation of Fe^{2+}, the Milli-Q water was treated with N_2 gas. In a typical experiment, 1 mL AuNP@DNA was added into 9 mL H_2O in a round-bottom flask. Then, concentrated Fe^{2+} (100 mM) was added to a final concentration of 1 mM into the mixture under stirring. After this, the mixture was heated to 95°C for 3 h. For AuNP@DNA/Fe formed with different DNA concentrations, PCR tubes were used for the reactions with a total volume of 100 μL and the temperature

was controlled using a PCR thermocycler. In all these reactions, the final AuNP concentration was 1 nM during the heating process.

4.2.5 **DOX adsorption and release**

Before mixing with DOX, all nanoparticles were washed with water by centrifugation. To load DOX, 1 μM DOX was mixed with 0.2 nM AuNPs with a total volume of 500 μL in water and incubated at room temperature for 4 h. The adsorption capacity of DOX was determined by the fluorescent intensity of the free DOX remained in the supernatant. For DOX release, AuNP@DNA/Fe/DOX was incubated with 1× PBS. Fluorescent spectra were measured before and after 4 h incubation with excitation at 500 nm.

4.3 Results and Discussion

4.3.1 **Au@DNA/Fe core-shell nanoparticles formation**

We first attached a dense layer of DNA to AuNPs using the freezing method.[25, 80, 247] The DNA (400 nM) and 13 nm AuNPs (1 nM) were mixed at a ratio of 400:1. After freezing and thawing, the AuNPs remained well dispersed (Figure 4.1A), and around 72 DNA strands were attached to each AuNP. Therefore, the concentration of the free DNA was around 328 nM, which remained in the sample and were not removed. This conjugate was named AuNP@DNA. We then heated the sample with 1 mM Fe^{2+} at 95°C for 3 h following the reported protocol.[89] A well-dispersed purple product was obtained after a brief sonication. From the TEM image in Figure 4.2A, a shell was formed. Control experiments without Fe^{2+} showed no shell (Figure 4.1B). Since the thickness of the shell was around 5 nm, we approximate it as the thickness of the DNA layer. Thus, the local DNA concentration on the AuNP reached 23 μM, comparable to the typical concentration of DNA (25 μM) used in the AuNP-free work.[89] The overall DNA concentration was only 400 nM averaged to the whole solution. Thus, the AuNPs concentrated the DNA by nearly 60-fold.

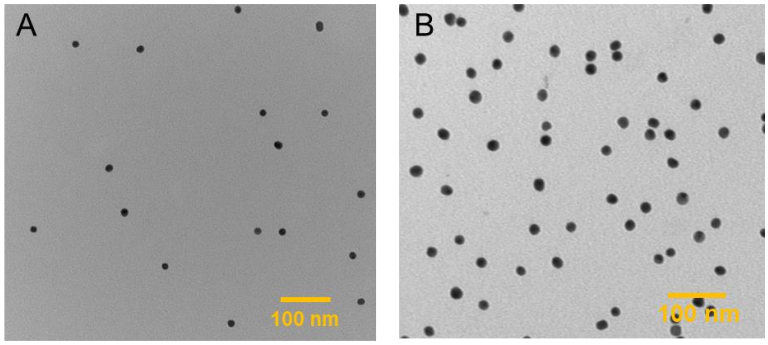

Figure 4.1 (A) A TEM micrograph of the AuNP@DNA used in this work. (B) A TEM image of the AuNP@DNA with the existence of excess free DNA incubated under 95°C for 3 h without Fe^{2+}.

Without the AuNP core, no DNA/Fe nanoparticles were observed after heating 400 nM DNA and 1 mM Fe^{2+} mixture (Figure 4.2B). Note that in the above synthesis, 82% of the DNA strands were free in solution (not attached to the AuNPs). When we removed the free DNA by centrifugation, no shell was formed on AuNPs either (Figure 4.2C). Therefore, the AuNP@DNA served as a nucleation point to recruit the free DNA to form the shell.

We also prepared a control sample by simply mixing the AuNPs and the SH-DNA without freezing. In this case, only around five DNA strands were on each AuNP and thus nearly 99% of the DNA strands were free in solution. After heating with 1 mM Fe^{2+}, no shell was observed (Figure 4.2D). Therefore, a high local DNA concentration on the AuNPs along with some free DNA in solution was required for the growing the DNA/Fe shell.

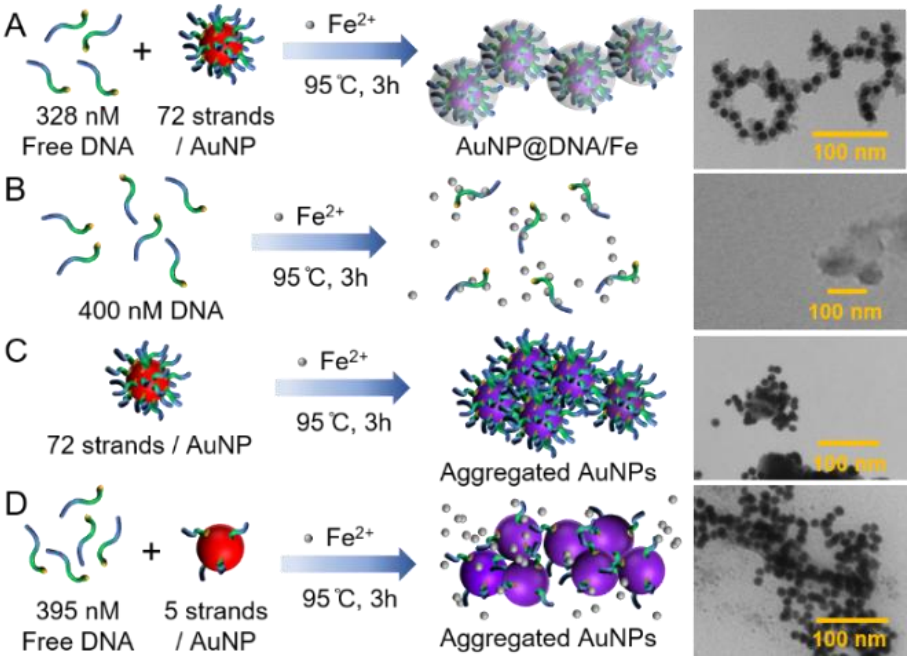

Figure 4.2 Schemes and TEM micrographs showing the products synthesized with different reactants: (A) AuNP@DNA (high DNA density) and free DNA; (B) 400 nM free DNA; (C) AuNP@DNA (high DNA density) with free DNA removed; and (D) AuNP@DNA (low DNA density) and free DNA. All samples were heated with 1 mM Fe^{2+} under 95 °C for 3 h.

After the formation of the DNA/Fe shell, the localized surface plasmon resonance (LSPR) peak of the AuNP (blue line in Figure 4.3) red shifted, which can be attributed to the increased refractive index near the AuNPs. In addition, the aggregation of the AuNPs can also cause the red shifted extinction peak. For the samples in Figure 4.2D, although no shell formed, the UV-vis peak also shifted due to aggregation of the AuNPs (black line, Figure 4.3).

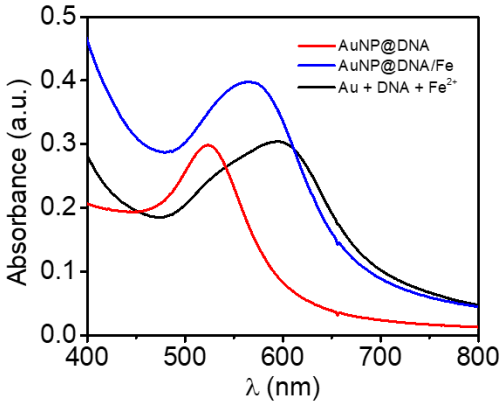

Figure 4.3 UV-vis absorption spectra of different AuNP-DNA complexes: red line: AuNP@DNA; blue line: the sample in (Figure 4.2A); black line: the sample in (Figure 4.2D).

4.3.2 **Control of the DNA/Fe shell thickness**

After confirming the growth of the DNA/Fe shell, we then attempted to control the thickness of the shell. Since a thicker shell would require more DNA, aside from the AuNP@DNA conjugate, we also added various concentrations of the free DNA. The total DNA concentration ranged from 0.4 μM to 58.8 μM. Indeed, DNA/Fe shells with different thicknesses were generated (Figure 4.4A). The nanoparticle size distribution histograms show that the diameter of core-shell NP increased from 22 ± 3 to 95 ±33 nm (Figure 4.4B and C). Controlling the size of the DNA/Fe nanoparticles has yet to be demonstrated, and we herein solved this problem taking advantage of the localized growth around the AuNP core.

Interestingly, the LSPR peak of the AuNPs shifted to shorter wavelengths, though the thickness of DNA/Fe shell increased as more DNA was added (Figure 4.4D). This reflected that the change in refractive index brought by the DNA/Fe shell was not the main factor for the redshift of LSPR peak. From the TEM (Figure 4.4A), the distance between the AuNPs increased as more DNA was added. This observation indicated that the aggregation of the AuNPs was the main factor for the red-shifted UV-vis peak.

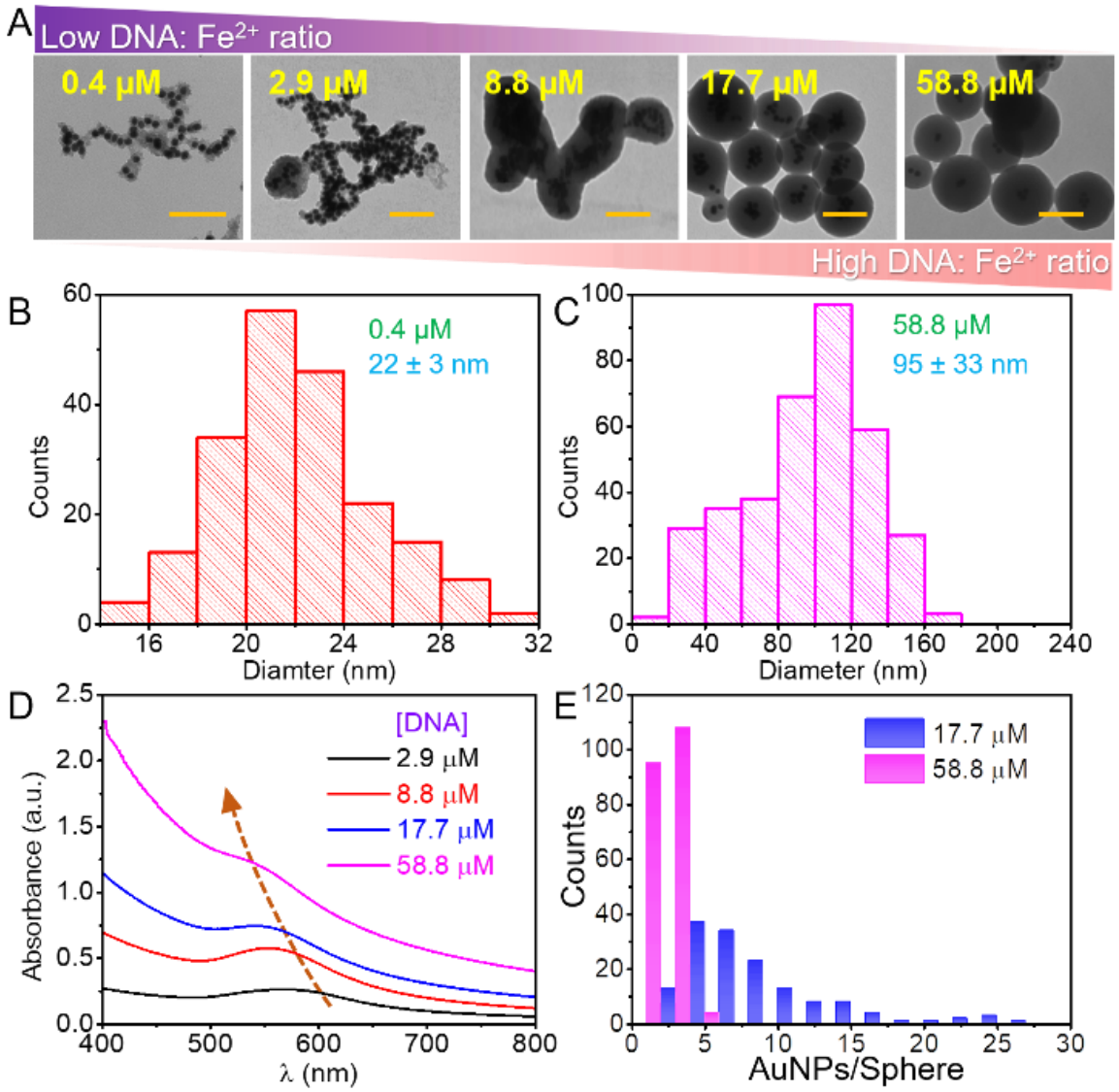

Figure 4.4 (A) TEM images of AuNP@DNA/Fe formed with various DNA concentrations. In all samples, 1 mM Fe^{2+} was used. The scale bars in TEM images are 100 nm. AuNP@DNA/Fe formed with a higher DNA concentration had a thicker DNA/Fe shell. Size distribution histograms of AuNP@DNA/Fe formed with (B) 0.4 μM and (C) 58.8 μM DNA and 1 mM Fe^{2+}. (D) UV-vis spectra of AuNP@DNA/Fe NPs formed with various concentrations of DNA. (E) The distribution histograms of the number of AuNP cores in each AuNP@DNA/Fe sphere.

In Figure 4.4A, the samples formed with different DNA concentrations appeared quite different. For example, when the DNA concentration was 8.8 μM, many AuNPs were trapped in merged shells. With 17.7 and 58.8 μM DNA, spherical shapes were obtained. From the histogram in Figure 4.4E, more AuNPs were individually dispersed when more DNA was added. For the sample formed with a total of 58.8 μM

DNA, over 90% AuNP@DNA/Fe had only one or two AuNP cores. Larger TEM micrographs are shown in Figure 4.5A-C, where these features are more clearly presented. We reason that before the formation of DNA/Fe hybrids, the interactions between the DNA and Fe^{2+} were necessary. To help explain it, we used the ratio of nucleobase:Fe^{2+} to replace DNA concentration. When a low DNA concentration was used (e.g. 0.4 μM and 2.9 μM), many free Fe^{2+} ions were present since the ratio of nucleobase: Fe^{2+} was less than 5:100. The free Fe^{2+} ions can screen the charge repulsions between AuNP@DNA and lead to their aggregation (Figure 4.5D).

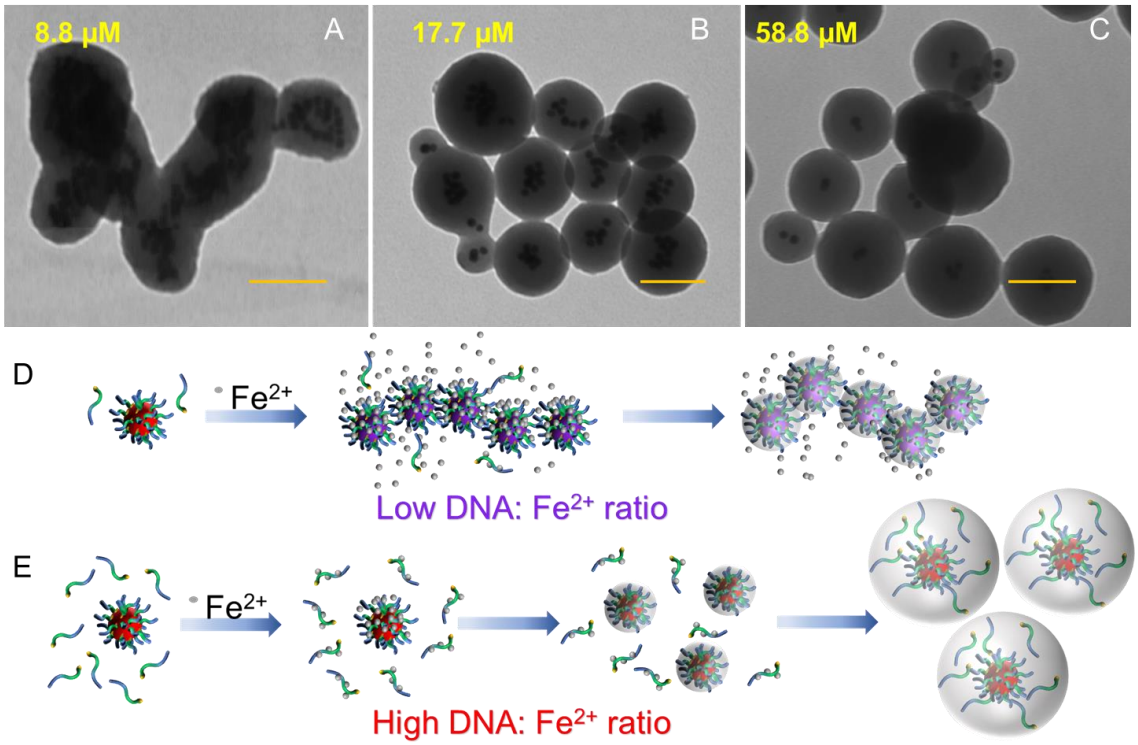

Figure 4.5 (A-C) TEM micrographs of AuNP@DNA/Fe formed with various DNA concentrations. In all samples, 1 mM Fe^{2+} was used. In these TEM images, the number of AuNPs in each sphere decreased as the DNA concentration increased. Scale bars: 100 nm. Schemes show the growing processes of DNA/Fe shells on AuNPs with a (D) low DNA and (E) high DNA concentration.

When 58.8 μM DNA was used, the nucleobase:Fe^{2+} ratio was 1:1. Most of the Fe^{2+} ions were involved in interacting with DNA and few free Fe^{2+} ions were available to aggregate the AuNP@DNA. As a result, the AuNP@DNA conjugates were individually dispersed (Figure 4.5E). Therefore, the concentration of the free Fe^{2+} and DNA in the system are the key factors of controlling the final product. When free Fe^{2+} dominated, the AuNP@DNA would aggregate despite the thin DNA/Fe shell. When DNA dominated, Fe^{2+} ions were all recruited to the AuNP surface to grow a thicker shell.

4.3.3 **Rhodamine 6G (Rh6G) fluorescein loading**

Now that we prepared a core/shell material with tunable shell thickness, we then studied whether we can achieve selective control of each component. When KCN was added, we found that the AuNP core disappeared while the shell remained intact, suggesting that CN^- could diffuse this shell layer and dissolve the AuNP core (Figure 4.6A, left). In addition, when phosphate buffer was added, the shell structure was disrupted (Figure 4.6A, right). Therefore, the core or shell of AuNP@DNA/Fe could be selectively etched (Figure 4.6B).

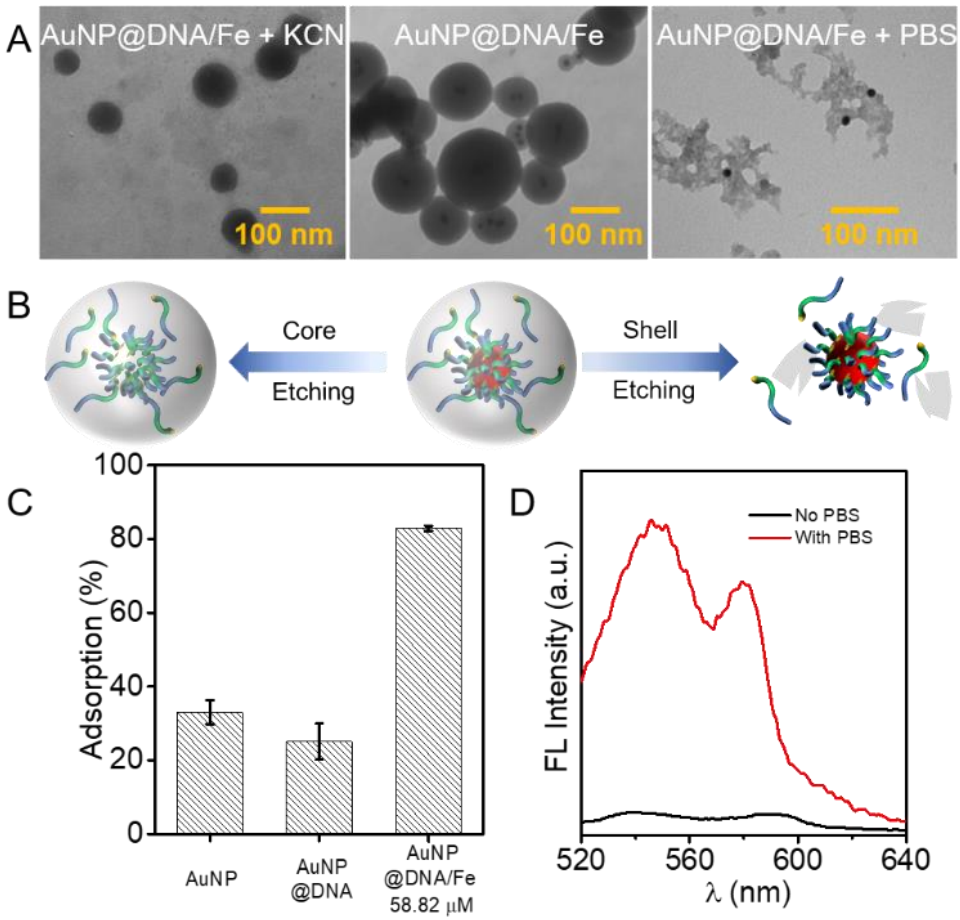

Figure 4.6 (A) The TEM images showing the products after selectively etching the AuNP core or the DNA/Fe shell. (B) A scheme showing the selective etching of shell or core of AuNP@DNA/Fe NPs. (C) DOX loading capacity on AuNPs, AuNP@DNA, and AuNP@DNA/Fe nanoparticles. (D) Fluorescence emission spectra of DOX molecule released from AuNP@DNA/Fe with and without 1X PBS. Excitation: 500 nm.

After knowing that the shell is porous and allows molecular diffusion, we then tested it for molecular containment. The core-shell AuNP@DNA/Fe NPs with a thicker shell might offer a high drug

loading capacity, and here we used doxorubicin (DOX) as a model drug. We mixed 1 μM DOX directly with 0.2 nM nanoparticles and incubated the sample at room temperature for 4 h. For the AuNP@DNA/Fe NPs formed with 58.8 μM DNA (a thick shell), over 80% DOX was adsorbed, and this high loading capacity was attributed to the thick shell. For comparison, the free AuNP and AuNP@DNA loaded only ~ 30% and 25% DOX, respectively (Figure 4.6C). The loading capacity of AuNP was slightly higher than that of AuNP@DNA can be attributed to that there were more sites on free AuNPs available for the cation-π interaction and coordination chemistry between AuNP's cationic surface and DOX molecules.[248] After incubating the DOX-loaded AuNP@DNA/Fe sample with 1X PBS, the DOX drug was released as the shell dissolved (Figure 4.6D).

4.3.4 **Colorimetric sensing**

Based on the optical properties of AuNPs, the potential application of AuNP@DNA/Fe NPs in colorimetric sensing was also studied. Since both aggregation and LSPR can redshift the plasmon peak and thus cause a much larger color change than those solely based on the LSPR effect, and the DNA layer can prevent AuNPs from irreversible aggregation, when we dissolve the shell, we may achieve a large color change. Because the AuNP@DNA/Fe NPs with thinner shells had a larger redshift, the AuNP@DNA/Fe formed with 0.4 μM and 1 mM Fe^{2+} was used to explore colorimetric sensing. We utilized competing molecules such as phosphate, which had a strong interaction with Fe^{2+} than DNA did, to dissolve the shell (Figure 4.7A).

When the shell was etched by phosphate, a clear color change from purple to red can be observed with the naked eyes (Figure 4.7B). A careful titration of LSPR shift as a function of phosphate concentration was conducted and a higher phosphate concentration produced more color change (Figure 4.7C). From the calibration curve, a detection limit of 0.78 mM (3σ/slope) was obtained. We can make an analog to the typical DNA-directed assembly for colorimetric sensing. In those cases, the AuNPs were brought together by a linker DNA to produce a large color change. Here, the AuNPs were brought together by aggregation by Fe^{2+}.

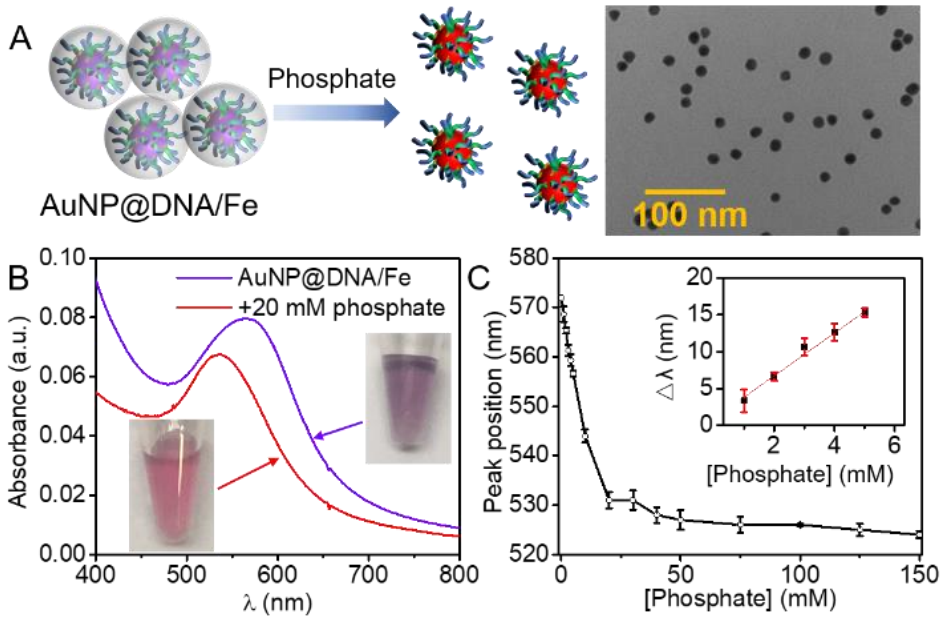

Figure 4.7 (A) A scheme showing the etching of the shell of AuNP@DNA/Fe NPs by phosphate. A TEM micrograph on the right showing the individual AuNPs after etching the DNA/Fe shell by phosphate. (B) A blue shift in the plasmon absorption peak for AuNP@DNA/Fe in 20 mM phosphate buffer before (purple line) and after (red line) 4-hour incubation. (C) LSPR shifts of AuNP@DNA/Fe NPs as a function of phosphate concentration. Inset: the curve at a low concentration range. Δλ was calculated based on the peak position shifts.

4.4 Conclusion

In summary, we have utilized the high local DNA density on AuNP to form DNA/Fe hybrids with a controllable shell thickness. The concentration of DNA oligonucleotides required to form DNA/Fe dropped from micromolar to nanomolar levels. The DNA:Fe^{2+} ratio determined the final morphologies of AuNP@DNA/Fe core-shell structures. A higher DNA concentration not only led to a thicker shell on the AuNPs but also prevented the aggregation of the AuNPs. Both the core and the shell can be selectively dissolved. Finally, owing to the selective etching of DNA/Fe shell, the potential applications of AuNP@DNA/Fe for drug delivery and colorimetric sensing were explored.

Chapter 5 Enhancing the Peroxidase-like Activity and Stability of Gold Nanoparticles by Coating a Partial Iron Phosphate Shell

The results presented in this chapter have been published as:

Zhicheng Huang, Biwu Liu and Juewen Liu, Enhancing the Peroxidase-like Activity and Stability of Gold Nanoparticles by Coating a Partial Iron Phosphate Shell. *Nanoscale* 2020, 12 (44), 22467-22472.

5.1 Introduction

Gold nanoparticles (AuNPs) are one of the most used materials in nanotechnology.[5, 40, 79, 249-250] Aside from their excellent optical properties and biocompatibility needed for biosensing,[251] drug delivery,[30] and materials assembly,[252] their enzyme-like catalytic activities have also caught interest in recent years.[253-256] For example, AuNPs possess glucose oxidase like activity and can convert glucose to gluconic acid and hydrogen peroxide.[124, 257] Many glucose or H_2O_2 sensors were developed based on AuNPs.[124, 131, 258] We recently found dehydrogenase activity of AuNPs using estradiol (E2) as a substrate.[259] What's more used is the peroxidase-like activity of AuNPs, since peroxidase nanozymes might replace horseradish peroxidase in immunoassays and other bioanalytical and environmental applications.[122, 260-263]

Two main challenges of using peroxidase AuNPs include low activity and poor colloidal stability, resulting in poor signals with large variations. The most often used citrate-capped AuNPs are irreversibly aggregated upon adding even a moderate concentration of NaCl (e.g. 20 mM). We were interested in performing surface modifications to improve nanozymes.[264] AuNPs can be readily modified by a diverse range of ligands, and most of the ligands contain a thiol group. In addition, it has been shown that Hg^{2+},[139] Ce^{3+},[128] I^-,[265] and DNA[137] can all increase the peroxidase-like activity of AuNPs. Many works have also been done on coating AuNPs with an inorganic shell, such as silica,[266-268] metal oxides,[269] and noble metals.[270-272]

Iron phosphate is composed of cost-effective and biocompatible components, and this material has been used for energy storage,[273] biosensing,[274-275] and catalysis.[276-277] Iron containing materials are also likely to have peroxidase-like activities.[278-279] In this work, we controlled the growth of an iron phosphate shell on AuNPs and this core/shell structure showed drastically enhanced nanozyme activity and colloidal stability. However, to achieve optimal activity, the shell cannot fully cover the AuNPs, suggesting interesting interfacial catalysis.

5.2 Materials and Methods

5.2.1 Chemicals

All the DNA samples were purchased from Integrated DNA Technologies (IDT, Coralville, IA). Gold (III) chloride trihydrate ($HAuCl_4 \cdot 3H_2O$), 6-mercapto-1-hexanol (mercaptohexanol or MCH), H_2O_2 (30 wt%), 3,3′,5,5′-tetramethylbenzidine (TMB), and all the metal chloride salts were purchased from Sigma-Aldrich (St Louis, MO). Sodium acetate, sodium phosphate monobasic, and 4-(2-hydroxyethyl) piperazine-1-ethane sulfonate (HEPES) were from Mandel Scientific (Guelph, ON, Canada). Silica microspheres were from Polyscience, Inc (Warrington, PA, USA). 50 nm citrate-capped AuNPs were from Cytodiagnotics (Burlington, ON, Canada). Milli-Q water was used for preparing buffers and solutions.

5.2.2 Synthesis of citrate-capped AuNP and HEPES-capped Au NS

The 13 nm citrate-capped AuNPs were synthesized as previously reported.[213] Based on an extinction coefficient of $2.7 \times 10^8\ M^{-1} \cdot cm^{-1}$ at 520 nm, the stock concentration of the 13 nm AuNP was 9.8 nM.[246] To synthesize HEPES-capped gold nanostars (AuNSs), 200 μL 20 μM $HAuCl_4$ was added into freshly prepared 20 mL HEPES solution (pH 7.4, 50 mM).[280] Then, this mixture was incubated in a dark room. After 1 h, the solution started to become blue. Both the citrate-capped AuNPs and HEPES-capped AuNSs were store at 4°C for further use.

5.2.3 Au@FeP preparation

To form Au@FeP of various thickness, different concentrations of Fe^{2+} were respectively added into AuNPs dispersed in phosphate buffer. Taking Au@1 mM FeP as an example, first, 1 nM AuNPs were stirred in phosphate buffer (10 mL, 1 mM, pH 7.1) for 3 min at room temperature. Then, 200 μL of 50 mM Fe^{2+} was added into the solution under high-speed stirring in five additions. The time between each addition was 3 min. Finally, the Fe^{2+} concentration reached 1 mM and the sample was further reacted for 15 min. Finally, all the nanoparticles were washed with Milli-Q water by centrifugation for 3 times (10000 rpm, 20 min). The growth of FeP on HEPES-capped AuNS was performed in the same way.

5.2.4 ζ-potential measurement

ζ-potentials were measured using dynamic light scattering (Zetasizer Nano 90, Malvern). In a typical experiment, 0.1 nM AuNPs and Au@FeP NPs were respectively dispersed in 1 mL buffer (20 mM acetate buffer, pH 5). The ζ-potential values were measured at 25°C.

5.2.5 **TMB oxidation kinetics**

For a typical peroxidation reaction, TMB substrate (0.5 mM) was mixed with 0.1 nM NPs in 100 µL 20 mM pH 5 acetate buffer. Then, 2.5 µL 200 mM H_2O_2 was added to initiate the reaction. The final volume of each sample was 100 µL. The absorbance at 652 nm for TMB was monitored by using a microplate reader (SpectraMax M3). The oxidized TMB spectra were measured by a microplate reader (Tecan Spark).

5.2.6 **Methods for TEM and XRD**

TEM images were taken by a Phillips CM10 100 kV transmission electron microscope. XRD measurements were conducted at room temperature on a PANalytical Empyrean diffractometer with Cu Kα radiation equipped with a PIXcel bidimensional detector.

5.3 Results and Discussion

5.3.1 **FeP-coated AuNPs with enhanced colloidal stability**

Our synthesis was performed as showed in Figure 5.1A. Freshly prepared $FeCl_2$ was added into 1 nM citrate-capped 13 nm AuNPs dispersed in 1 mM pH 7.1 phosphate buffer. The AuNPs remained well dispersed in this process. The TEM images (Figure 5.1B) show a core shell structure, and the thicknesses of the shell can be controlled by varying the concentration of $FeCl_2$ from an incomplete shell with 0.05 mM $FeCl_2$ to a full 6 nm shell with 1 mM FeP. The shell can also be coated on 50 nm citrate-capped AuNP and HEPES-capped Au nanostar (AuNS) by the same method (Figure 5.1C and D). To characterize the composition of the shell, we performed X-ray diffraction (XRD, Figure 5.1E, black spectrum), which indicated that the shell on the AuNPs was crystalline.[281] The diffraction peaks marked by the blue squares were assigned to $Na_{4.55}Fe(PO_4)_2$-$H_{0.45}O$ (JCPDS card No. 52-1393),[275] whereas the ones marked by the green dots were from the AuNP core. This means the dominant redox state of Fe in the shell was +2, consistent with the salt we added. For simplicity, we named the shell FeP in this work, and the AuNPs coated with iron phosphate are called Au@FeP NPs.

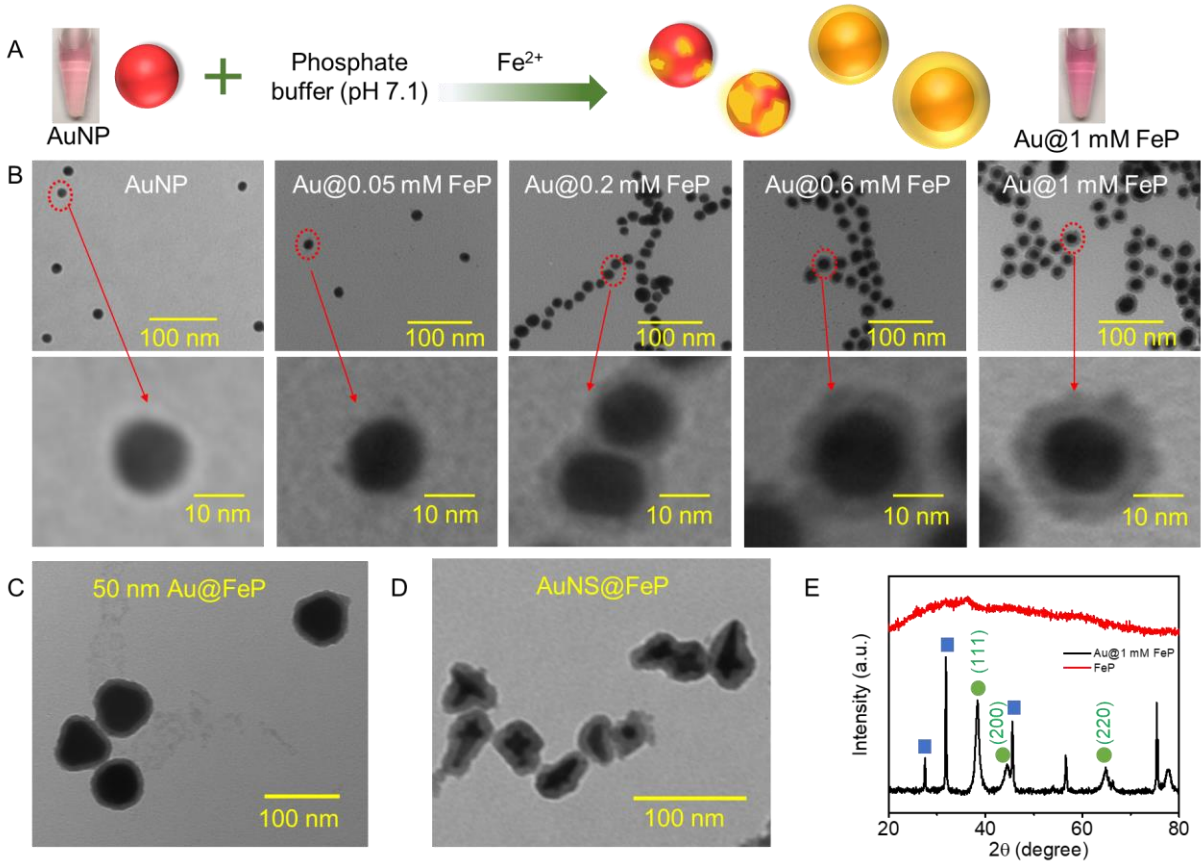

Figure 5.1 (A) A diagram showed the growth of a FeP shell on AuNPs. The shell thicknesses are dependent on the concentration of Fe^{2+} added. The photographs of AuNP and Au@1 mM FeP solution are also shown. (B) TEM images of AuNP and Au@FeP NPs with various FeP shell thicknesses. The red circled areas in are enlarged in the lower row. TEM images of (C) 50 nm citrate-capped AuNPs and (D) HEPES-capped AuNSs coated by FeP. (E) The XRD pattern of FeP synthesized in solution (red line) and on the AuNPs (black line). The three peaks marked with green dots are from the *fcc* gold lattice.

We named the materials prepared with 1 mM Fe^{2+} to be Au@1 mM FeP. Compared to the original AuNPs, the Au@FeP NPs had higher extinction coefficients and showed a red shift in the UV-vis spectra (Figure 5.2A). The sharp peaks confirmed the Au@FeP NPs were well dispersed. With the FeP shell, the AuNP could withstand freezing/thaw (-20°C) and a high salt concentration without aggregation (100 mM NaCl, Figure 5.2B). For comparison, the citrate-capped AuNPs aggregated after these treatments. This experiment also confirmed coating of a stabilizing shell. These core/shell particles could be useful for exploiting the application of AuNPs under exotic conditions.[25, 282] While a silica shell can be coated on AuNPs,[283-284] the chemistry of coating FeP is quite simple without the need of a sol-gel process.[268] Besides this, the rapid hydrolysis and bulk precipitation of silica precursor (e.g. tetraethyl orthosilicate (TEOS)) make it hard to form a thin silica shell on citrate-capped AuNPs.[267]

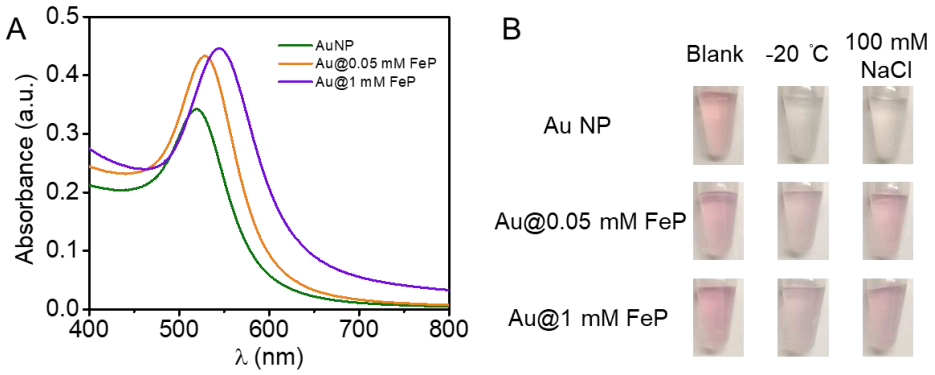

Figure 5.2 (A) UV-vis spectra of the AuNP, Au@0.05 mM FeP, and Au@1mM FeP. (B) Photographs of the AuNP and Au@FeP NPs after treated with various conditions.

5.3.2 Peroxidase-like activity of FeP-coated AuNPs

After preparing the Au@FeP NPs with controllable shell thickness, we then investigated their peroxidase-like activity using 3,3,5,5-tetramethylbenzidine (TMB) as the substrate. The one-electron peroxidation product of TMB has blue color. First, we studied the effect of pH. We took Au@0.1 mM FeP NP as our sample and 0.5 mM free FeP (no AuNPs) as a control. The free FeP control here was prepared by directly adding 0.5 mM Fe^{2+} into the phosphate buffer. We used 5 times higher Fe^{2+} concentration for the control to ensure our results. As shown in Figure 5.3B, the FeP control only showed a weak activity at pH 4, while Au@0.1 mM FeP showed 2.4-fold higher activity at both pH 4 and 5 (Figure 5.3A).

We then centrifuged the samples and measured the peroxidase-like activity from the supernatants (Figure 5.3C). In this assay, the free FeP and Au@0.1 mM FeP NP were respectively incubated in acetate buffer (pH 4 or pH 5) for one hour. No activity was observed from the supernatants of Au@0.1 mM NPs, suggesting that this particle was quite stable, and no dissolution took place. Non-centrifuged Au@0.1 mM FeP showed activities at both pH 4 and 5, which indicated that the peroxidase activities were mainly from the NPs. On the other hand, activity was observed in the supernatants of the FeP control. From XRD (Figure 5.1E, red spectrum), amorphous FeP particles were synthesized in the control without the AuNP cores. Compared to the crystalline FeP on the AuNPs, amorphous FeP has much higher solubility.[285] Based on this, the amorphous FeP might be partially dissolved at pH 4, and Fe^{2+} ions were released, which contributed to the peroxidase-like activities of controls.

Inspired by the high peroxidase-like activity of Au@0.1 mM, we then tested the effect of shell thickness (Figure 5.3D). Initially, the activity increased with increase of Fe^{2+} concentration. After peaking at 0.1 mM Fe^{2+}, the activity then started to drop with more Fe^{2+} added. Compared to citrate-capped AuNP, the absorbance intensity of oxidized TMB was ~20-fold higher with Au@0.1 mM FeP. The catalytic

activity of Au@1 mM FeP was similar to that of citrate-capped AuNP. Therefore, the FeP shell thicknesses was critical in determining the peroxidase-mimic activities of Au@FeP NPs. This trend is summarized in a diagram showed in Figure 5.3E.

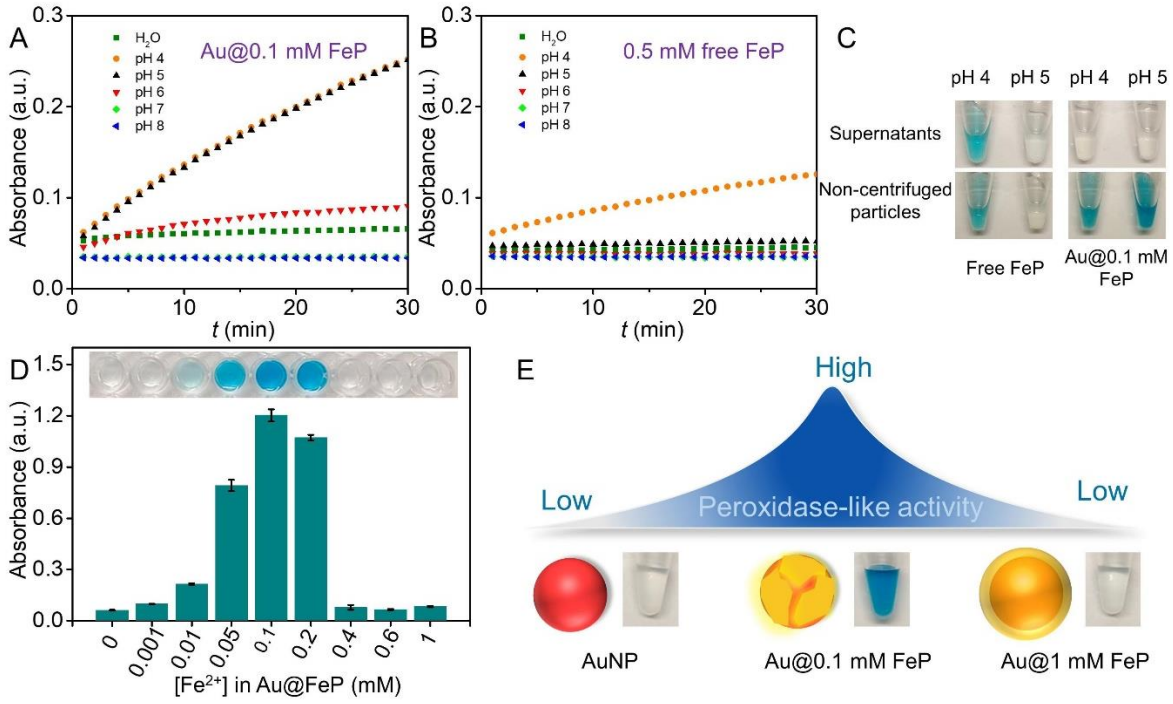

Figure 5.3 The effect of pH on the peroxidase-like activities of (A) Au@0.1 mM FeP and (B) free FeP in 20 mM buffer, 5 mM H_2O_2, and 0.5 mM TMB. Acetate buffer was used for pH 4 and 5; phosphate buffer was used for pH 6-8. (C) The photographs of the TMB substrate oxidized by the supernatants and non-centrifuged particles of free FeP and Au@0.1 mM FeP after 20 min reaction. Before reactions, the free FeP and Au@0.1 mM FeP had been respectively incubated at pH 4 and 5 acetate buffer for 1 h. (D) The absorbance of oxidized TMB at 652 nm catalyzed by Au@FeP NPs prepared with different Fe^{2+} concentrations. 0.1 nM AuNPs, 5 mM H_2O_2, 0.5 mM TMB substrate, and 20 mM pH 5 acetate buffer was used. (E) A diagram showing the change in the peroxidase-like activity as a function of FeP shell thickness.

5.3.3 Mechanism study

To understand the mechanism of FeP-enhanced TMB oxidation activity, we used SiO_2 nanoparticles as another template to grow FeP, and the SiO_2@FeP NPs were also successfully prepared (Figure 5.4A-C). However, no activity was observed for TMB peroxidation (Figure 5.5A). Therefore, the AuNP core was critical. At pH 5, the zeta-potential of citrate-capped AuNPs was around -15 mV. The low activity of citrate-capped AuNPs for oxidizing TMB might be related to electrostatic interactions. The oxidation product of TMB is positively charged, which may adsorb on the AuNPs to inhibit further

reactions.[138, 286] Although the surface of Au@FeP NPs became less negative with the FeP shell (Figure 5.4D), the zeta-potential of Au@0.1 mM FeP was similar to that of Au@1 mM FeP (both between -5 mV and -10 mV), suggesting that surface charge might not be the determining factor for activity.

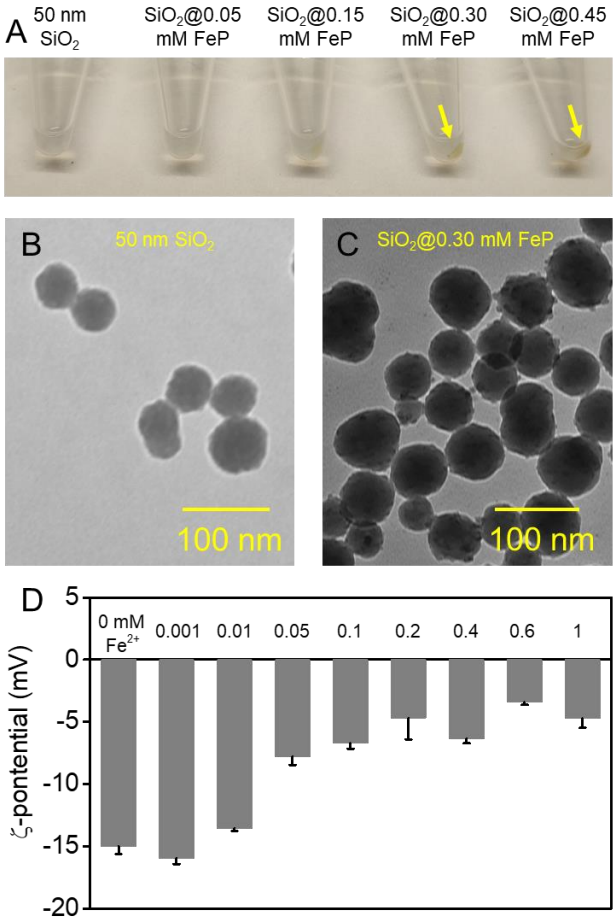

Figure 5.4 (A) The photographs of SiO_2 nanoparticles and the SiO_2 coated by a FeP shell after centrifugation. The yellow products pointed out by the arrowheads suggest the successful synthesis of FeP on SiO_2. The TEM images (B) before and (C) after FeP coating also confirmed the growth of FeP on SiO_2. New features assigned to FeP particles were found on the SiO_2 NPs. (D) The zeta-potentials of the citrate-capped AuNPs and Au@FeP NPs with different FeP shell thicknesses in 20 mM pH 5 acetate buffer. The concentration of the AuNPs was 0.1 nM.

Since thin FeP shells may have more defects where the substrates can access to the Au/FeP interfaces, we speculated that the interfaces might be critical for the enhanced activity. To test this hypothesis, we mixed the AuNPs and the free FeP particles directly, where no improvement was observed (Figure 5.5B). Since it is hard to visually observe the Au/FeP interfaces from the 13 nm spherical AuNP cores, we then employed the anisotropic AuNSs. Although most of the areas were covered by thick FeP

shells, there might still be some exposed Au surface for accessing the Au/FeP interfaces (Figure 5.5C). For the AuNS@FeP NPs, a similar trend in peroxidase-like activity was observed, where too much FeP also inhibited the activity (Figure 5.5D). The AuNS@0.15 mM FeP showed higher activity than AuNS@0.45 mM FeP. For the AuNS@0.15 mM FeP NPs, although a thick FeP shell grew on the base of the AuNS, still a lot of exposed Au surfaces were observed (Figure 5.5E). However, it was hard to see exposed Au of the AuNS@0.45 mM FeP (Figure 5.5F). This experiment supported a positive correlation between the Au/FeP interfaces and the peroxidase-like activity.

To further confirm that the Au surface is critical for TMB oxidation, we used 6-mercapto-1-hexanol (MCH) to cover the Au surface. Due to the strong interaction between Au and thiol, MCH can densely adsorbed on Au surfaces, and inhibit the peroxidase activity (Figure 5.5G). The results showed that the activity of Au@FeP was suppressed by MCH (Figure 5.5H). When the MCH concentration was increased to 500 μM, the peroxidase activity of Au@0.1 mM FeP was nearly fully inhibited. This result again reflected that exposed Au surface is required for activity.

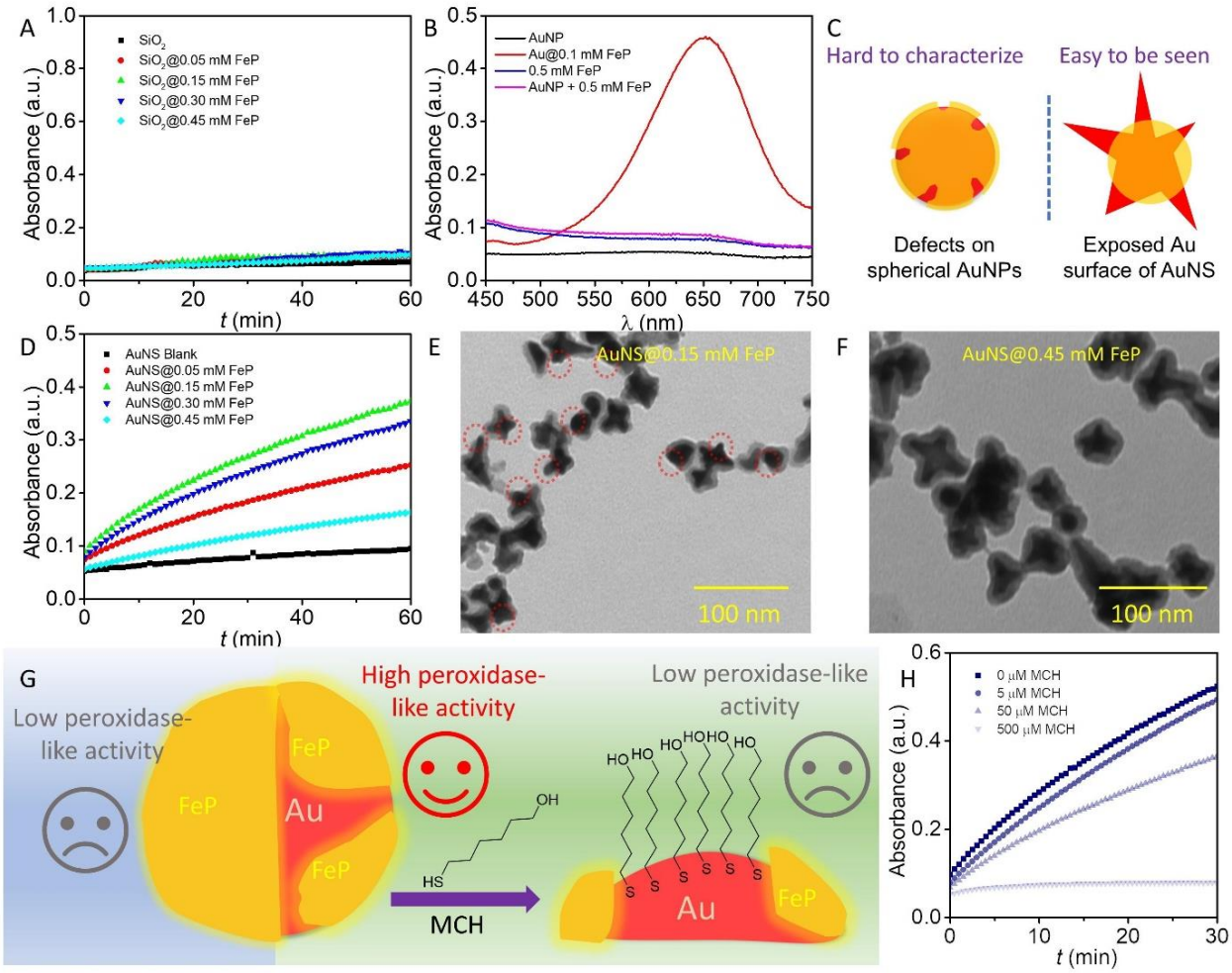

Figure 5.5 (A) The kinetics of TMB oxidation monitored at 652 nm catalyzed by SiO_2 and SiO_2@FeP NPs. (B) The absorbance spectra of oxidized TMB catalyzed by 0.1 nM AuNP, 0.1 nM Au@0.1 mM FeP, 0.5 mM free FeP, and the mixture of 0.1 nM AuNP and 0.5 mM free FeP. (C) Proposed models of FeP growth on spherical AuNP and branched AuNS. (D) The kinetics of TMB oxidation catalyzed by AuNS@FeP NPs with different FeP shell thicknesses. TEM images of (E) AuNS@0.15 mM FeP (The exposed Au surface were circled in red.) and (F) AuNS@0.45 mM FeP. (G) A diagram showed the importance of the Au/FeP interface in peroxidase activity. Blue area represented Au@1 mM FeP. Green area represented Au@0.1 mM FeP. When the interface was blocked by MCH molecules, low-peroxidase-like activity was obtained. (H) The kinetics of TMB oxidation monitored at 652 nm catalyzed by Au@0.1 mM FeP in the presence of different concentrations of MCH.

For Au@FeP NPs, the recyclability was then studied at pH 5. In a typical reaction, 0.5 nM AuNPs were used to catalyze 0.5 μM TMB by 5 mM H_2O_2. After 10 min, the Au@FeP NPs were collected by centrifugation, and the recovered Au@FeP NPs were washed with ethanol and Milli-Q water. For Au@0.2

mM FeP, the catalytic efficiency was 50% for round 2 and 25% for round 3 (Figure 5.6). Compared with Au@0.05 mM FeP, Au@0.2 mM FeP had a better ability of retaining catalytic efficiency. Part of the reason for the decrease of activity could be attributed to the loss of sample during centrifugation and washing. Surface modification of AuNPs has been shown to significantly affect its peroxidase-like activity. For example, Hg^{2+} was able to boost the activity and the mechanism was believed to be the formation of amalgam on the surface. [139, 287-288] This observation has been used for the detection of Hg^{2+}.

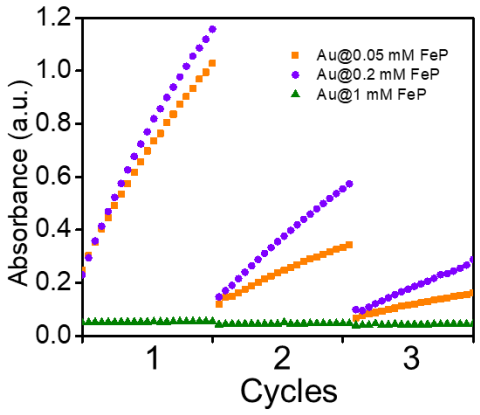

Figure 5.6 The recyclability of the peroxidase-like activity of Au@0.05 mM FeP, Au@0.2 mM FeP and Au@1 mM FeP in three catalytic cycles. The kinetics of TMB oxidation were recorded for 10 min in each cycle. Taking washing time into consideration, each cycle was 40 min. 0.5 nM Au@FeP NPs were used. 5 mM H_2O_2 and 0.5 mM TMB substrate were reacted in 20 mM pH 5 acetate buffer.

5.3.4 **Fe^{2+} detection**

In our system, obvious Fe^{2+}-dependent blue color was also achieved with the oxidation of TMB. Based on this color change, a sensor might be developed for Fe^{2+}. To test if this metal phosphate shell enhanced activity is unique to Fe^{2+}, we tried seven other common transition metal ions. We performed the same synthesis by adding 0.05 mM metal ions to phosphate and the AuNPs remained stably dispersed (Figure 5.8A). Among them, only the Fe^{2+} sample showed deeper red color, indicative that the other metals failed to form a shell. All the NPs were washed with H_2O for three times after the synthesis. From the TMB oxidation products in Figure 5.8B and the kinetics of TMB oxidation by various Au@metal phosphate (Figure 5.8C), only the Au@FeP(Fe^{2+}) NP showed high activity. This may be attributed to that only Fe^{2+} formed a partial phosphate shell on the AuNPs or other metal phosphate shells were inactive.

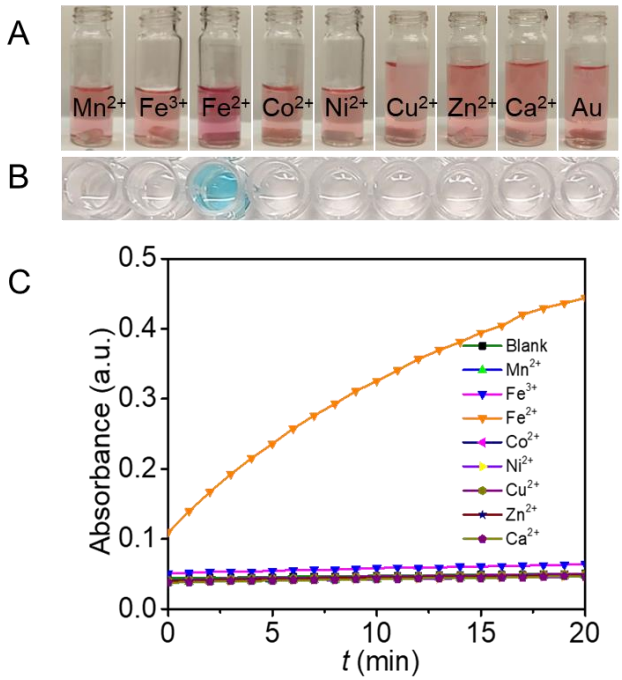

Figure 5.7 (A) Photographs of Au@metal phosphate formed with different transition metals. 0.05 mM metal ions and 1 mM phosphate buffer (pH 7.1) were used. (B) Selectivity test for the detection of Fe^{2+} by the TMB oxidation reaction. The kinetics of TMB oxidation in the presence of AuNPs mixed with various transition metal ions in phosphate buffer. 5 mM H_2O_2 and 0.5 mM TMB substrate were used. The concentration of the NPs was 0.1 nM.

Of note, Hg^{2+} can also increase the activity of AuNPs, which was due to the previously reported mechanism instead of forming a phosphate shell (Figure 5.9A). [139] Fe^{2+} can be distinguished from Hg^{2+} by the activity of the AuNP/metal ion mixtures in the absence of phosphate (Figure 5.9B).

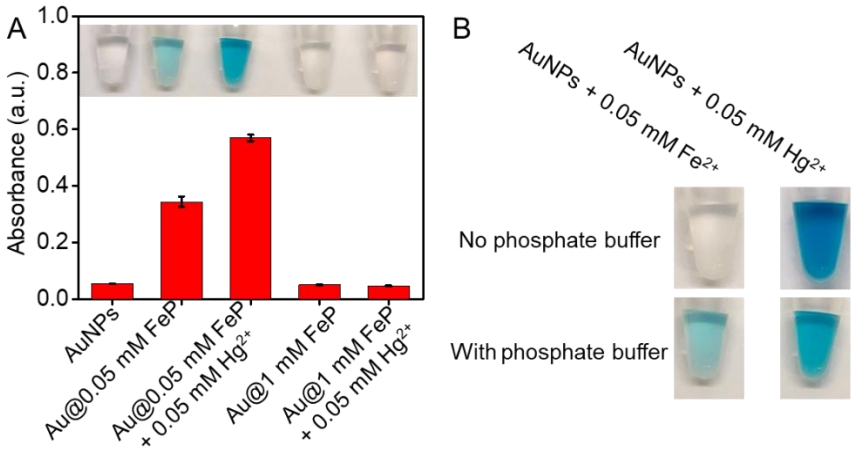

Figure 5.8 (A) The absorbance of oxidized TMB at 652 nm catalyzed by AuNPs, Au@0.05 mM FeP NPs, and Au@1 mM FeP NPs without/with 0.05 mM Hg^{2+}. Inset: corresponding photographs of TMB oxidized by the NPs. (B) Photographs of TMB oxidized by Au/Fe and Au/Hg complexes, which were respectively formed in H_2O and phosphate buffer. All the NPs were washed with H_2O for three times after the synthesis. 0.1 nM NPs, 5 mM H_2O_2, 0.5 mM TMB substrate, and 20 mM pH 5 acetate buffer were used. The absorbance intensities and photos were collected after 15 min reaction. Phosphate promoted the activity of the Fe^{2+} sample, but inhibited the activity of the Hg^{2+} sample, which can be used to tell these two metal ions apart.

After confirming the selectivity for Fe^{2+}, a series of Au@FeP NPs formed with 1 to 50 μM Fe^{2+} were used for TMB oxidation. The higher the TMB concentration, the deeper blue color was obtained (Figure 5.10A). A curve of absorbance of oxidized TMB at 652 nm against Fe^{2+} concentration was collected after reacting for 20 min (Figure 5.10B). From the calibration curve, a detection limit of 0.41 μM Fe^{2+} (3σ/slope) was obtained.

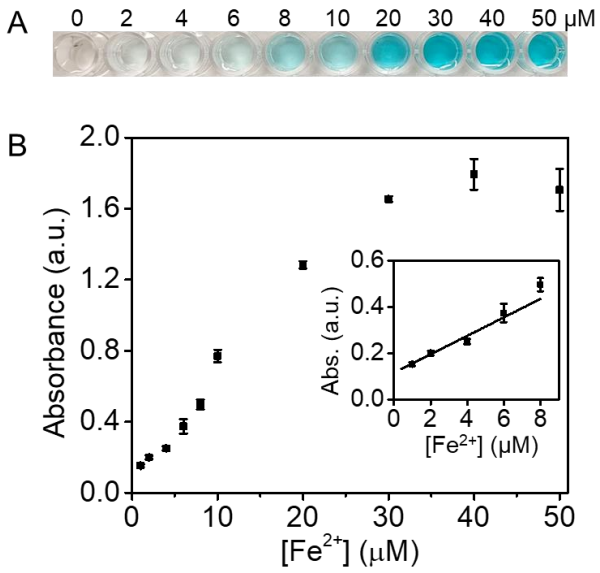

Figure 5.9 (A) A photograph of the sensor at various Fe^{2+} concentrations. (B) The absorbance of TMB at 652 nm produced by the sensor in various concentrations of Fe^{2+}. Inset: the response at a low concentration range. 0.5 nM Au@FeP NPs, 5 mM H_2O_2, and 0.5 mM TMB were used.

5.4 Conclusion

In summary, we have reported a simple method to grow a crystalline FeP shell on AuNPs, and an incomplete shell can boost the peroxidase-like activity of the AuNPs. The coating of FeP was achieved by a one-step reaction in 30 min. The thickness of FeP shell can be altered simply by tuning the Fe^{2+} concentration. To further study the mechanism of activity enhancement, FeP was coated on various cores (citrate-capped AuNPs, HEPES-capped AuNSs, and SiO_2), and the Au/FeP interface was found to be critical for the enhanced activity. Based on the enhanced activity, Au@FeP was used for Fe^{2+} detection. This work offers a simple solution for the stability and activity problems of AuNPs as a peroxidase-mimicking nanozyme, and it could be a useful step to catching up the performance of real enzymes.[289]

Chapter 6 TMB^+-Mediated Rapid Etching of Urchin-like Gold Nanostructures for H_2O_2 Detection

6.1 Introduction

Gold nanoparticles (AuNPs) possess much higher extinction coefficients than organic dyes due to their localized surface plasmon resonance (LSPR), allowing visual observation at low nanomolar and even picomolar concentrations.[70] The positions of LSPR peaks are dependent on the sizes and morphologies of AuNPs. Therefore, colorimetric detection can be made based on morphology changes of AuNPs, especially anisotropic AuNPs.[40] Over the past decades, anisotropic AuNPs etching-based sensors were prevalent.[112] For example, the etching of gold nanorods (AuNRs) can happen along the longitudinal direction, leading to continuous color changes.[290-292] Interestingly, a high concentration of cetrimonium bromide (CTAB) appeared to be essential for etching AuNRs. In the presence of CTAB, the redox potential of $AuBr^{2-}/Au^0$ (0.93 V vs NHE) can be dramatically decreased by the formation of the $AuBr^{2-}$-$(CTA)^{2+}$/Au (< 0.2 V vs NHE).[293-295] The addition of hydrogen peroxide (H_2O_2), acids, and O_2 can also help the oxidation or etching of AuNRs. However, a high CTAB concentration (usually over 50 mM) and extreme conditions (e.g., 250 mM HCl or 45 °C) limited the applications of AuNRs.[121, 294, 296] Therefore, we wish to explore other gold nanostructures that might be etched more easily under mild conditions.

Urchin-like AuNPs (AuNUs) are important anisotropic AuNPs for a broad range of applications from biosensors to cancer therapy.[297-300] AuNUs can grow on AuNP seeds when additional Au^{3+} ions are reduced by sodium citrate and hydroquinone.[301-302] The tip areas on the AuNUs are highly reactive because of their high surface energy,[303-304] and the sharp tips exhibit larger electric fields at their concavo-convex sites compared to neutral curvature areas.[305] With these sharp tips, morphological changes of AuNUs can be triggered easily. For example, upon laser irradiation, AuNUs can melt into spherical AuNPs.[306]

Enzyme-linked immunosorbent assay (ELISA) based detection systems have been widely used for the detection of various kinds of disease biomarkers.[307-308] 3,3',5,5'-tetramethylbenzidine (TMB) is an important substrate that can be oxidized to TMB^+ (blue) or TMB^{2+} (yellow) for colorimetric immunoassays. It was reported that TMB^{2+} can quantitatively and efficiently etch AuNRs, which converts the color of TMB^{2+} to the color change of AuNRs to increase the sensitivity of detection.[290] However, as mentioned above, acids and heating were needed for this reaction to occur.

In this work, we studied TMB^+-induced etching of AuNUs, and comparisons were made with AuNRs. In particular, we tried to understand the role of CTAB and separated its effect on the surfactant part and the halide part. In the presence of a low concentration of CTA^+ and Br^- ions, TMB^+ can efficiently etch the branches of AuNUs. As a result, the morphology change of AuNUs was accompanied by a vivid

color variation. Based on these understandings, we used the TMB^+-induced etching of AuNUs to design a highly sensitive colorimetric biosensor for H_2O_2 detection under ambient conditions.

6.2 Materials and Methods

6.2.1 Chemicals

Gold (III) chloride trihydrate ($HAuCl_4 \cdot 3H_2O$), H_2O_2 (30 wt%), 3,3′,5,5′-tetramethylbenzidine (TMB), sodium oleate (NaOL), Triton X-100, Tween 80, and Tween 20, and acetic acid were from Sigma-Aldrich (St Louis, MO). Cetrimonium chloride (CTAC), cetrimonium bromide (CTAB), sodium chloride, sodium fluoride, sodium bromide, sodium hydroxide, sodium citrate, sodium phosphate were from Mandel Scientific (Guelph, Ontario, Canada). Milli-Q water was used for preparing buffers and solutions.

6.2.2 Preparation of spherical Au seeds

Citrate-capped Au seeds were synthesized according to the literature.[213, 309] Briefly, the 100 mL 1 mM $HAuCl_4$ was heated and boiled for 30 s. Then, 10 mL of 38.8 mM sodium citrate was added quickly. The mixture solution changed from light yellow to wine red in 2 min. The 13 nm AuNPs were obtained after refluxing for another 20 min. The same protocol was used to prepare 38 nm Au seeds, except that the concentration of $HAuCl_4$ was doubled.

6.2.3 Preparation of AuNUs

First, 30 mM hydroquinone was freshly prepared with Milli-Q water and used the same day. For a typical synthesis, 1 mL $HAuCl_4$ was diluted with 180 mL H_2O under vigorous stirring. Subsequently, 600 μL AuNP seeds, 3 mL 38.8 mM sodium citrate, and 10 mL 30 mM hydroquinone was added sequentially. The 13 nm and 38 nm spherical Au seeds were, respectively, used for generating AuNUs-13 and AuNUs-38 NPs. The solutions were incubated at room temperature for 30 min under stirring. In the end, the resulting AuNUs were washed with 5 mM pH 6 phosphate buffer at 4000 rpm for 8 min and stored at 4°C for further use. The morphologies of AuNUs were characterized by TEM (Phillips CM10 100 kV) and UV-vis spectroscopy.

6.2.4 Preparation of AuNRs

AuNRs were prepared by a seed-mediated method using a binary surfactant system as reported by Murray.[310] For seed preparation, 5 mL 0.5 mM $HAuCl_4$ was added into 5 mL 0.2 M CTAB solution in a 20 mL scintillation vial. Then, 0.6 mL of ice-cold fresh 0.01 M $NaBH_4$ was diluted to 1 mL with water and injected into the $HAuCl_4$-CTAB mixture under rapid stirring (1200 rpm). After stirring for 2 min, the color of the solution changed from yellow to brown, and the seed solution was used after standing for 30 min at

room temperature. To prepare a growth solution, 7.0 g CTAB and 1.234 g NaOL were dissolved in 250 mL of warm water (50°C) in an Erlenmeyer flask. After the solution was cooled to 30°C, 18 mL 4 mM $AgNO_3$ was added to the solution under stirring. The mixture was kept undisturbed at 30°C for 15 min, and then 250 mL of 1 mM $HAuCl_4$ was added and stirred for another 90 min. 1.5 mL HCl (37 wt% in water) was further added into the solution and stirred for 15 min. Afterward, 1.25 mL of 0.064 M ascorbic acid (AA) was added into the solution under vigorously stirred for 30 s. Finally, 0.4 mL seed solution was injected into the growth solution with stirring for 30 s. The growth solution was left undisturbed for 12 h. Finally, the AuNRs were centrifuged at 7000 rpm for 30 min to remove excess emulsifier, and washed once with water. The final AuNRs were stored in 5 mM CTAB at 4°C.

6.2.5 **The preparation of TMB^+ and TMB^{2+}**

2 mL 0.5 mM TMB substrate in 5 mM pH 4 buffer solution was irradiated under UV light (~370 nm) for 30 min to get blue TMB^+. The final concentration of TMB^+ was determined by the absorbance of TMB^+ at 652 nm with an extinction coefficient ε of 3.9 10^4 $M^{-1}cm^{-1}$. TMB^{2+} was prepared by mixing TMB^+ solution and 250 mM H_2SO_4 with a 1:1 volume ratio. The final concentration of TMB^{2+} was determined by the absorbance of TMB^{2+} at 450 nm with ε of 5.9 10^4 $M^{-1}cm^{-1}$.

6.2.6 **Etching of AuNUs by TMB^+**

In a typical etching experiment, 80.5 μL H_2O, 7.5 μL 100 mM CTAC, 30 μL 100 mM pH 6 phosphate buffer, 20 μL AuNUs, 3 μL 500 mM NaBr were added into microtubes in sequence. Then, 9 μL TMB^+ of various concentrations were pipetted into the microtubes, respectively. The final volume of samples was 150 μL. After vigorous stirring for 30 s, the samples were incubated at room temperature for 30 min before UV-vis absorbance measurements.

6.2.7 **Colorimetric H_2O_2 detection**

First, a 123 μL mixture solution was prepared with 1.5 μL 10 mM TMB substrate, 15 μL 100 mM pH 6 phosphate buffer, 7.5 μL 100 mM CTAC, and 99 μL H_2O. Subsequently, 1 μL 0.1 mg/mL HRP was added into the mixture solution in a 96-well plate, followed by the addition of 20 μL AuNUs-13 NPs, 3 μL 500 mM NaBr, and 3 μL various concentrations of H_2O_2. The total volume in each well was 150 μL. The final concentrations of TMB substrate, phosphate buffer, and CTAC were 100 μM, 20 mM, and 5 mM, respectively. Then, the mixture solution was incubated at room temperature for 30 min. Finally, the UV-vis absorbance was monitored by a plate reader, and the color of the samples was recorded using a digital camera.

6.3 Results and Discussion

6.3.1 **TMB^+-mediated etching of AuNUs**

The AuNUs were synthesized by a seed-mediated growth method. Spherical AuNPs, which were prepared by citrate reduction, were used as seeds. For AuNP seeds of around 38 nm, the resulting urchin-like products were called AuNUs-38. AuNUs grown from 13 nm seeds were also made and named AuNUs-13. From the TEM image shown in Figure 6.3A, these AuNUs-38 had multiple sharp tips. Most of the AuNUs-38 were between 100 nm and 130 nm (Figure 6.3D). Compared with the spherical AuNP seeds with a surface plasmon resonance (SPR) peak at 526 nm (Figure 6.1), the SPR peak of AuNUs-38 showed a large red-shift, yielding a blue solution.

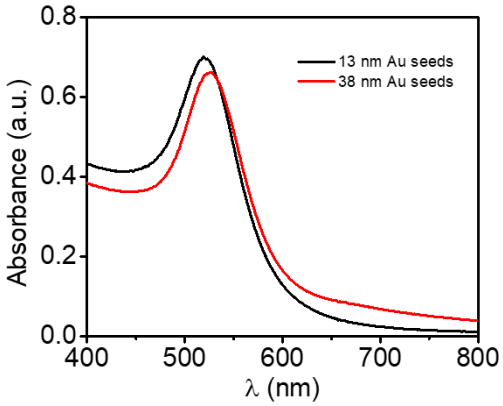

Figure 6.1 UV-vis absorption spectra of 13 nm and 38 nm Au seeds.

These sharp edges have higher surface energy, and they might be more easily etched. TMB is a common chromogenic substrate and upon one-electron oxidation, the TMB^+ product has a blue color. We hope to use TMB^+ to etch the AuNUs to amplify the color change. To avoid potential effects of other molecules, we produced TMB^+ by using UV irradiation (so no H_2O_2 or HPR was added).[290] It needs to be noted that this method only yielded around 11% of TMB^+, while the rest 89% were still the unreacted TMB substrate (Figure 6.2).

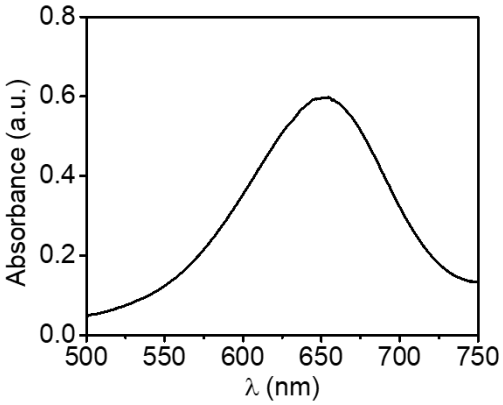

Figure 6.2 UV-vis absorption spectrum of four times diluted TMB oxidation product in pH 4 acetate buffer.

We then studied TMB^+-mediated etching of the AuNUs. In the presence of 5 mM CTAB, the sharp tips of AuNUs-38 were etched and rounded by the added TMB^+ (Figure 6.3B). The blue color of the AuNUs-38 solution turned red in 30 min. Although the etched products were still not spherical, a significant blue shift of SPR peaks (from 691 nm to 603 nm) was observed (Figure 6.3C). From the histogram in Figure 6.3D, the size of etched AuNUs-38 NPs was decreased from 110 nm to around 90 nm.

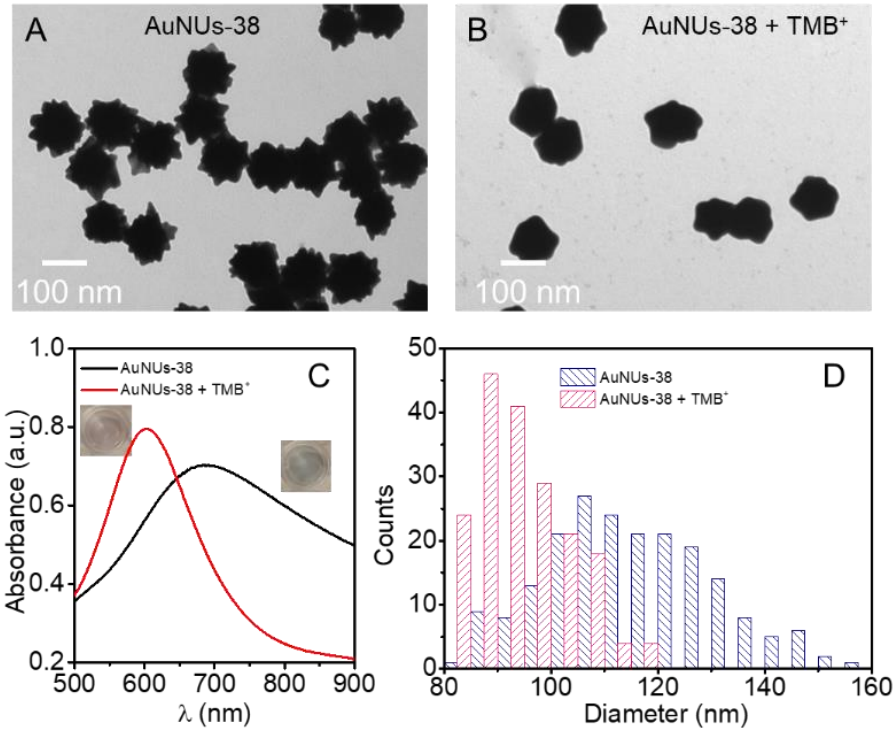

Figure 6.3 TEM images of AuNUs-38 NPs before (A) and after (B) the addition of TMB^+. (C) UV-vis absorbance spectra of AuNUs-38 NPs before and after etching. Inset photos are the color of Au corresponding samples. (D) The distribution histograms of the size change of AuNUs-38 NPs.

6.3.2 **AuNUs are more easily etched than AuNRs**

Since previous work mainly used AuNRs, we then compared the etching of AuNRs and AuNUs. We expected that AuNUs could be more sensitive for TMB^+ since the AuNRs lack the branches with high surface energy (Figure 6.4A). We noticed that while we were able to etch AuNUs using TMB^+, literature reported etching of AuNRs used TMB^{2+} (Figure 6.5A). TMB^{2+} etched AuNRs along their longitudinal direction, leading to a continuous color change.[112] We also studied AuNUs-13, which were smaller than AuNUs-38 in size, but with the same morphology. All the three AuNPs were incubated with various TMB^+ concentrations at room temperature. Interestingly, the AuNRs were quite stable under the etching conditions for AuNUs (Figure 6.5B and C). Even after 24-h incubation, no absorbance peak shift happened for AuNRs (Figure 6.5D). To etch the AuNRs, a high CTAB concentration (50 mM), strong acids, TMB^{2+}, and a high temperature of 80 °C were all required (Figure 6.4B). Even under such a harsh condition, the shift in the absorption spectra was small, and no obvious color change was observed in 1 h (Figure 6.5E).

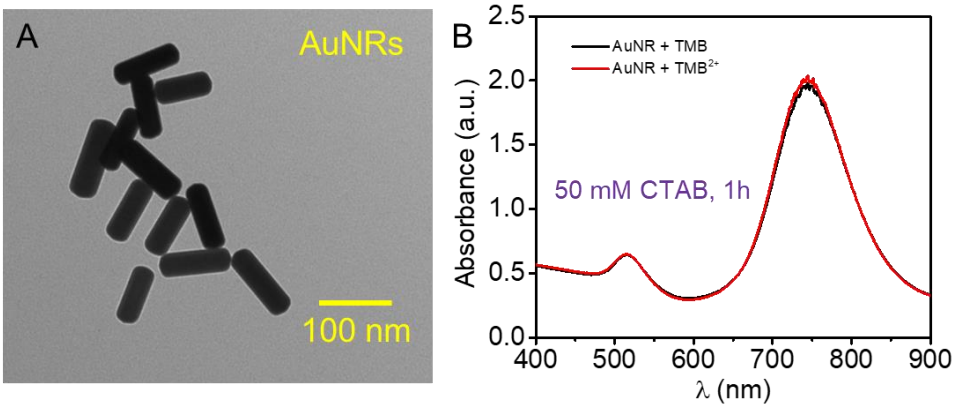

Figure 6.4 (A) The TEM image of AuNRs. (B)UV-vis spectra of AuNRs etched by various concentrations of TMB^+ in the presence of 5 mM CTAB without heating.

For AuNUs, after 1 h incubation, color changes happened for both AuNUs-38 and AuNUs-13 (Figure 6.5B). Although these AuNUs with smaller sizes showed smaller SPR peak shifts, a much more obvious color change was obtained (Figure 6.5C). Therefore, for the subsequent studies, we used the larger AuNUs for quantitative spectroscopic measurements, while used the smaller AuNUs for colorimetric sensing.

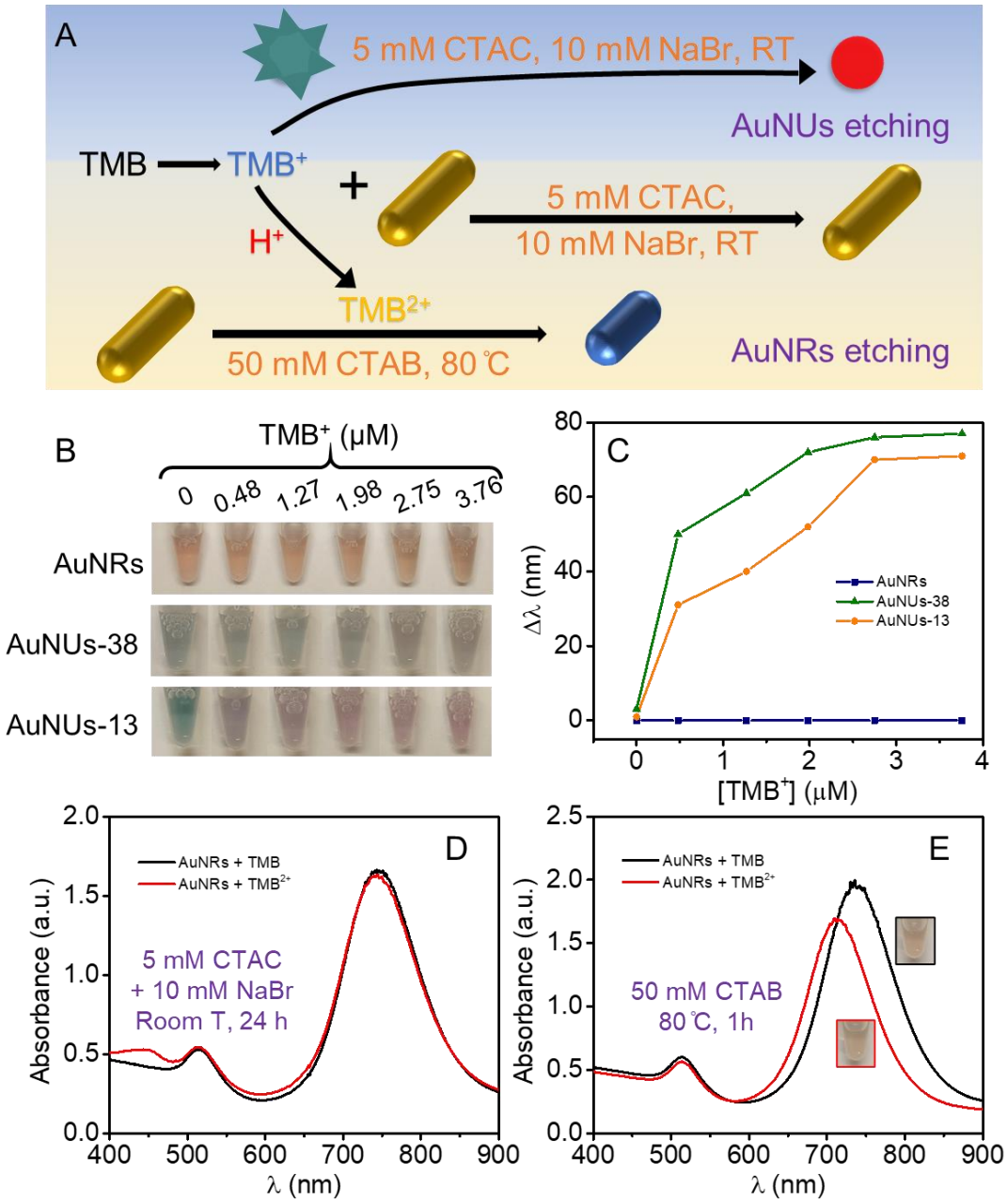

Figure 6.5 (A) Schematic illustration of the etchings of AuNUs and AuNRs by TMB^{+} and TMB^{2+} respectively. (B) Color changes of three AuNPs incubated with TMB^{+}. (C) SPR peak shifts of AuNRs, AuNUs-38, and AuNUs-13 after one-hour incubation with various TMB^{+} concentrations. In these etching experiments, 5 mM CTAC and 10 mM NaBr were used. Absorption spectra measurements of AuNRs reacted with TMB^{2+} in the presence of (D) CTAC and (E) CTAB. 10 μM TMB^{2+} was used in these experiments.

6.3.3 **Effects of halides and surfactants**

To acquire the best etching performance, the effects from the reaction conditions, such as pH, etching time, surfactant, and halide ion were investigated in detail. The difference in SPR peak positions ($\Delta\lambda$) was chosen to indicate the extent of etching of the AuNUs.

We started by optimizing surfactants. The as-synthesized AuNUs were mainly covered by weakly adsorbed citrate groups, which can be easily displaced by other stronger capping agents.[311-312] During our initial experiments, we used cetrimonium bromide (CTAB) as the capping agent since CTA^+ has been well studied on AuNR etching.[293] Herein, A few common surfactants were also evaluated, and interestingly, TMB^+ only etched the AuNUs in the presence of CTAB (Figure 6.6A). We also noticed that the etching was faster with higher CTAB concentrations (Figure 6.6B).

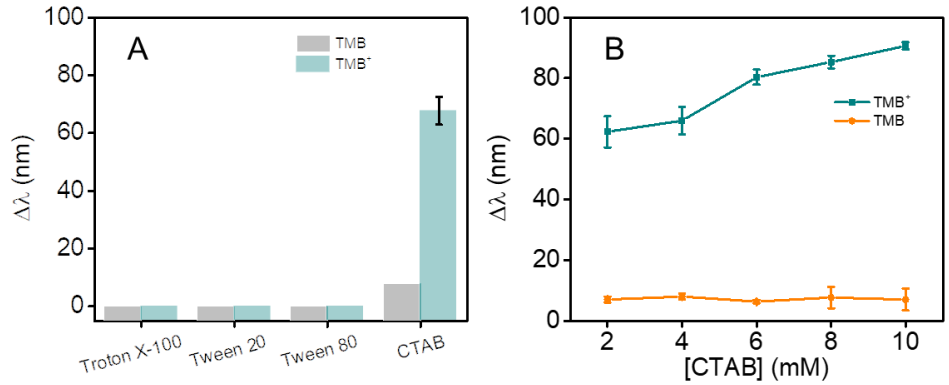

Figure 6.6 (A) SPR peak shifts of AuNUs-38 etched in the presence of 0.1% surfactants. were used. 0.1% CTAC & CTAB were respectively 3.1 mM and 2.7 mM. (B) SPR peak shifts of AuNUs-38 etching as a function of CTAB concentrations.

CTAB contained Br^- as its counterion, and Br^- has a strong affinity to the gold surface.[313] Halides counterions of the surfactant have been proved to be critical in the oxidation of CTAB-capped AuNRs.[314-315] Halides adsorption was widely studied for shape-controlled AuNP synthesis.[316] It is known the adsorbed concentrations of Br^- and I^- are much higher than that of Cl^- ions on Au surface,[317-318] and the interaction strength of halides with gold has the trend of $I^- > Br^- > Cl^-$. Thus, we expected that Br^- might be important during the etching process. Interestingly, without CTA^+, Br^- alone failed to induce the etching process (Figure 6.7A). Therefore, CTA^+ appeared to be required for AuNUs etching.

To confirm the roles of halide counterions for deeper mechanistic understanding, we conducted more etching experiments with the mixture of cetrimonium chloride (CTAC) and three halides (F^-, Cl^-, and Br^-). I^- was omitted here because a low concentration of iodide can cause serious etching of AuNUs without

the help of CTA^+ groups (Figure 6.7B). With 5 mM CTAC and up to 50 mM F^- or Cl^-, no SPR peak shifts were observed with the incubation with 4 μM TMB^+ for 30 min (Figure 6.7C and D). These trends are consistent with the etching of AuNR and Au nanostar.[303, 319] Therefore, Br^- and CTA^+ were both essential for etching the AuNUs.

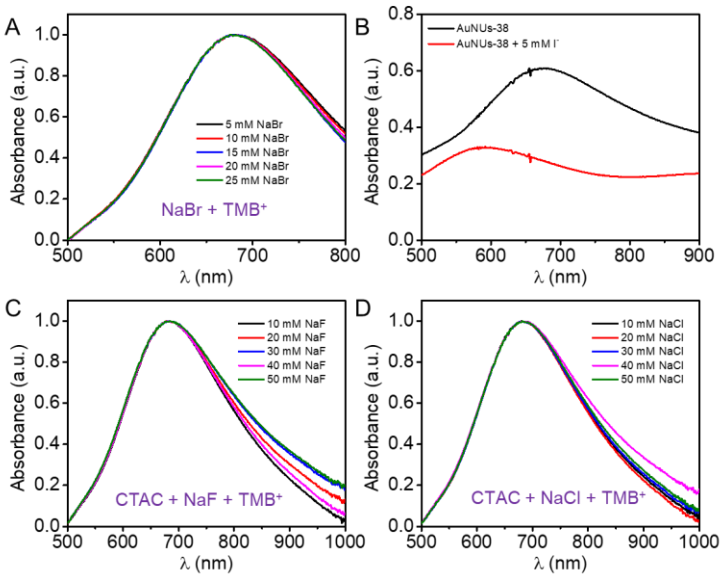

Figure 6.7 (A) The normalized absorption spectra of AuNUs incubated with the mixture of various NaBr concentrations and 4 μM TMB^+. (B) UV-vis spectra of AuNUs(38) NPs incubated with 5 mM NaI for 30 min. I^- ions can etch AuNUs without the addition of TMB^+. The effects of (C) F^- and (D) Cl^- on the etching of AuNUs-38 in the presence of 5 mM CTAC and 4 μM TMB^+.

The importance of Br^- was also confirmed by conducting etching experiments in a mixture of 0.25 mM CTAB 0.75 mM CTAC, 0.5 mM CTAB 0.5 mM CTAC, and 0.75 mM CTAB 0.25 mM CTAC (Figure 6.8). Greater $\Delta\lambda$ was generated with a higher portion of CTAB, again indicating the involvement of Br^- in the etching process.

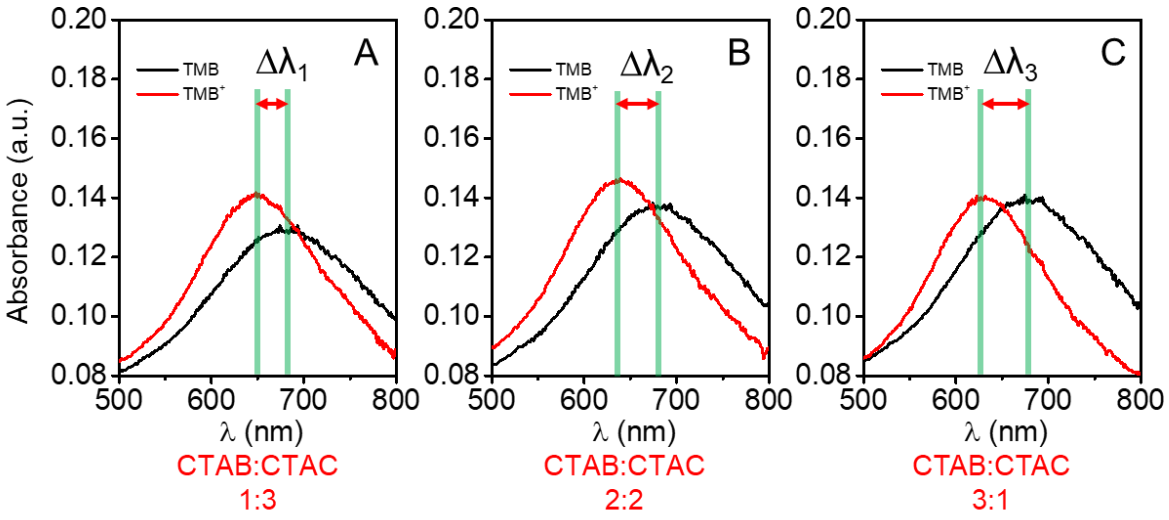

Figure 6.8 UV-vis spectra of AuNUs-38 etched in the presence of (A) 0.25 mM CTAB 0.75 mM CTAC, (B) 0.5 mM CTAB 0.5 mM CTAC, and (C) 0.75 mM CTAB 0.25 mM CTAC. Greater blue shift happened with higher portion of CTAB ($\Delta\lambda 3 > \Delta\lambda 2 > \Delta\lambda 1$).

To get a fast etching speed or a large SPR peak shift, higher CTAB concentrations are needed. However, a too high CTAB concentration may produce many bubbles, which can cause problems for quantitative absorbance measurements. Also, CTAB has poor solubility at room temperature. Therefore, we need to achieve fast etching with the lowest possible surfactant concentration. This goal might be achieved by using a mixture of CTAC (with the Br^- in CTAB replaced by Cl^-) and NaBr.

We fixed the CTAC concentration at 5 mM (10-folder lower than the typical 50 mM CTAB concentration), and larger SPR peak shifts happened with more NaBr added (Figure 6.9A). To avoid the aggregation of the AuNUs, 10 mM NaBr concentration was chosen for the subsequent work (Figure 6.9B). With 10 mM NaBr, larger SPR peak shifts were observed with higher CTAC concentrations (Figure 6.9C). When the CTAC concentration was higher than 2 mM, negligible improvements were obtained. This can be explained by that the critical micelle concentrations (CMC) of CTAB and CTAC are both around 1 mM at room temperature.[320-321] Therefore, we chose to use 5 mM CTAC in this work.

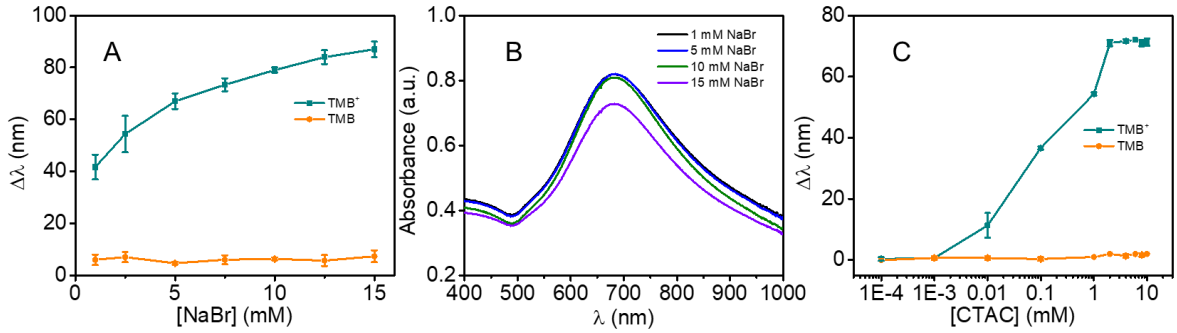

Figure 6.9 (A) SPR peak shifts of AuNUs-38 NPs as a function of NaBr. In these experiments, 5mM CTAC was used. (B) UV-vis spectra of AuNUs-38 in the presence of various NaBr concentrations. Slight aggregation of AuNUs-38 happened with the addition of 15 mM NaBr. (C) SPR peak shifts of AuNUs-38 etched by various concentrations of CTAC and fixed 10 mM NaBr.

6.3.4 **Optimization of etching time and pH**

After understanding the effects of surfactants and Br^-, we further investigated the etching time and pH conditions. Figure 6.10A shows that the etching was fast in the initial 20 min, after which the shift of the SPR peak was pretty slow. In 1 h, nearly 90 nm shift was observed. For the control sample (TMB substrate), only a minor increase in $\Delta\lambda$ (9 nm) after even 1 h. As a result, all the samples were incubated for 30 min to get a large and relatively stable difference in $\Delta\lambda$.

We then studied the effect of pH on the etching. An acidic environment was shown to facilitate AuNP etching in the presence of dissolved oxygen.[294, 322] However, many proteins are only stable in a narrow pH range near neutral. For example, horseradish peroxidase (HRP) loses its structural and conformational stability at pH < 4.[323] Thus, the etching of AuNUs-38 was studied between pH 4 and 8. From Figure 6.10B, at pH 4, the $\Delta\lambda$ of the TMB control sample was very close to TMB^+. The color difference of these two samples was indistinguishable with such close absorbance peak positions. As such, the etching was mainly caused by the low pH, and detection of TMB^+ was difficult at pH 4. The largest $\Delta\lambda$ difference was observed at pH 6. When the pH was higher than 6, the etching activity of TMB^+ decreased dramatically. This can be explained by the low stability of TMB^+ at higher pH (Figure 6.10C). Therefore, pH 6 was chosen as the optimal pH for further study. In terms of surface charges of AuNUs-38, all of them were negatively charged from pH 4 to 8 and thus should not be the reason for the difference (Figure 6.10D).

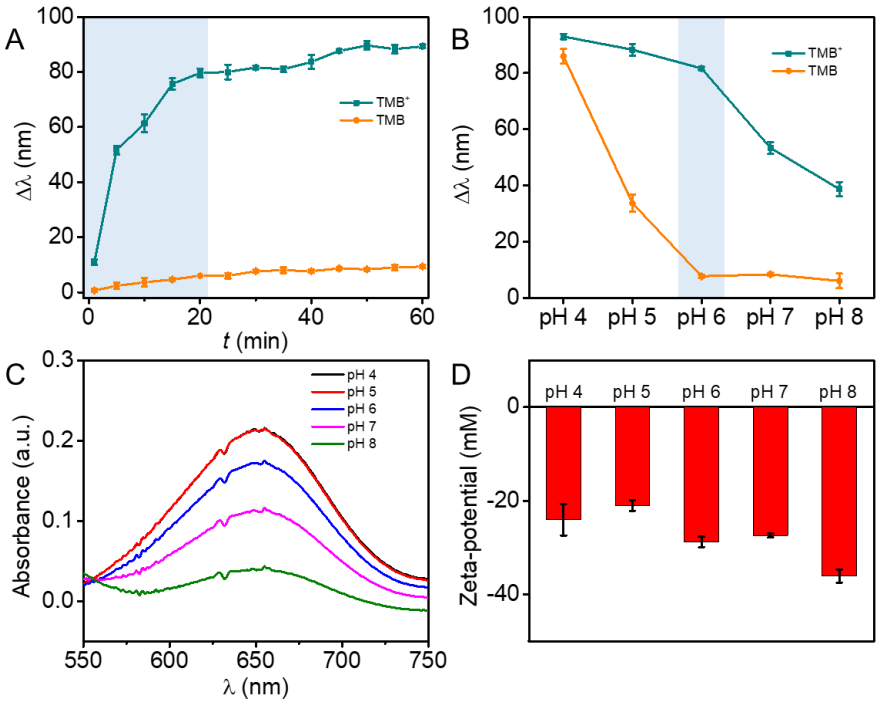

Figure 6.10 (A) The etching kinetics of AuNUs-38 where SPR peak shifts were used. (B) The SPR peak shifts of AuNUs-38 which were incubated in different pH environments. Acetate buffers were used for pH 4 and 5; phosphate buffers were used for pH 6-8. (C) The stabilities of TMB^+ produced by UV light at different pHs. (D) Zeta-potentials of AuNUs-38 at different pH values.

6.3.5 **Visual detection of H_2O_2**

H_2O_2 is an important by-product of many enzymatic reactions and has been used as a target molecule of many biosensors.[324-326] For example, the oxidation of glucose by glucose oxidase (GOx) can produce H_2O_2. It is well known that H_2O_2 can oxidize AuNRs in the presence of Br^- under acid conditions at high temperatures.[322] However, the concentration used for AuNRs oxidation is much higher than that used in our experiments. Over 1 mM H_2O_2 is required to cause slight etching of AuNUs (Figure 6.11).

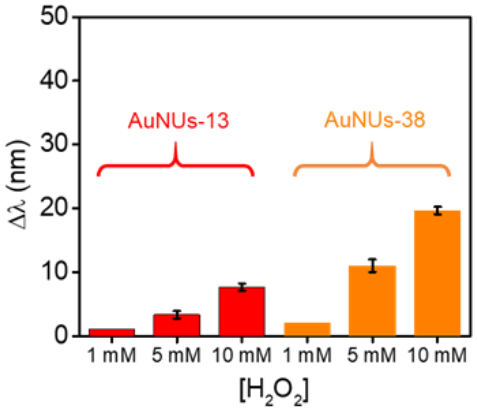

Figure 6.11 The stabilities of AuNUs-13 and AuNUs-38 in different concentrations of H_2O_2.

To realize the visual detection, the AuNUs synthesized from smaller Au seeds were used. A more vivid color change was generated with the sharp tips characteristic but smaller sized AuNUs (Figure 6.5B and Figure 6.12A). The experimental setup is similar to the conventional colorimetric ELISA. Horseradish peroxidase (HRP) enzymes can catalyze H_2O_2 to produce a more reactive radical species (•OH). Then •OH was quantitatively reacted with TMB substrate to generate TMB^+ (Figure 6.12B). Thanks to the mild conditions for AuNUs etching, HRP-H_2O_2 catalysis and AuNUs etching can be realized in one step. After TMB^+-mediated etching, an obvious blue shift for the SPR peak happed (Figure 6.12C). The etching reaction also happened fast in 20 min, and the control samples are very stable at pH 6 (Figure 6.12D and E). Only the samples with HRP displayed a color change (from blue to red). The images of color change are shown in Figure 6.12F.

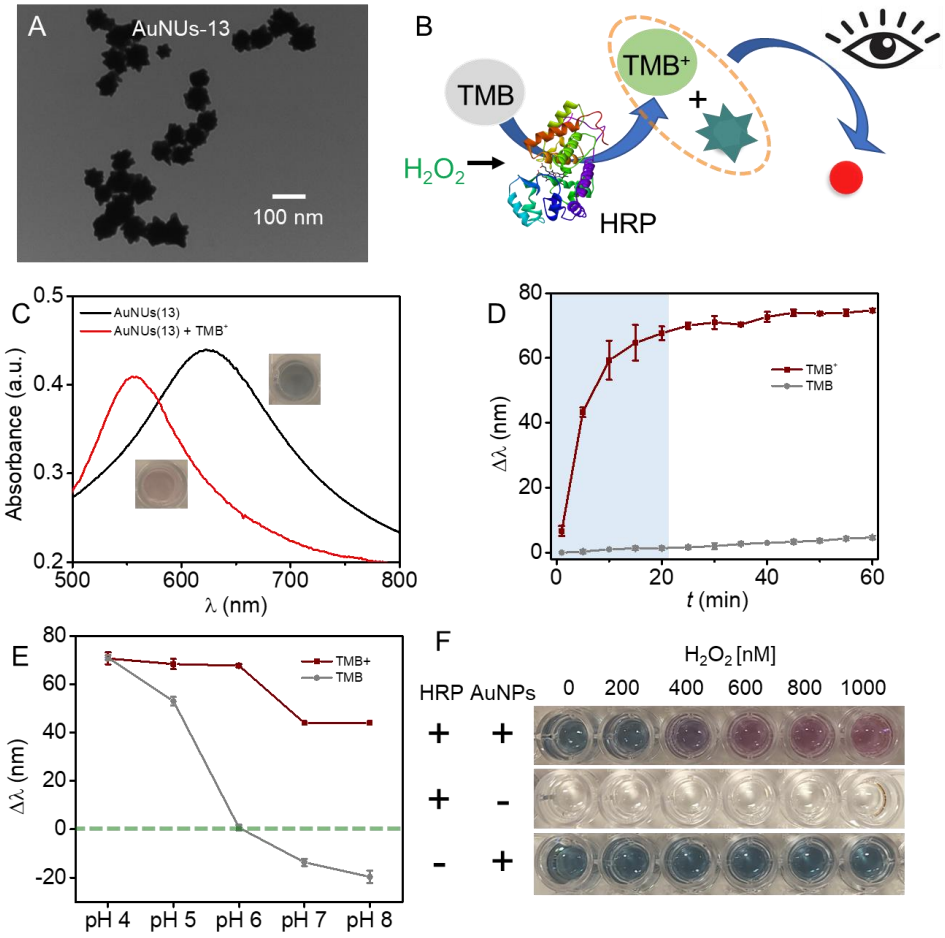

Figure 6.12 (A) A TEM image of AuNUs synthesized from 13 nm spherical AuNPs. (B) Schematic illustration of the etching of AuNUs induced by the product of HRP-catalysed TMB. (C) UV-vis spectra change of AuNUs-13 NPs with and without the addition of TMB^+. (D) The etching kinetics of AuNUs-13 NPs where SPR peak shifts were used. (E) The SPR peak shifts of AuNUs-13 NPs incubated in different pH environments. Acetate buffers were used for pH 4 and 5; phosphate buffers were used for pH 6-8. When $\Delta\lambda$ was negative, the aggregation of AuNUs-13 NPs happened. (F) Color changes of the proposed method with the increase of H_2O_2 concentration.

A significant color change when the concentration of H_2O_2 is equal to or higher than 400 nM. Under conditions used in this study, the limit of detection for H_2O_2 is 80.23 nM (3σ/slope, inset) (Figure 6.13). The sensitivity of this AuNP-based colorimetric sensors for H_2O_2 detection is ~7-fold more sensitive than the previous colorimetric detection.[327]

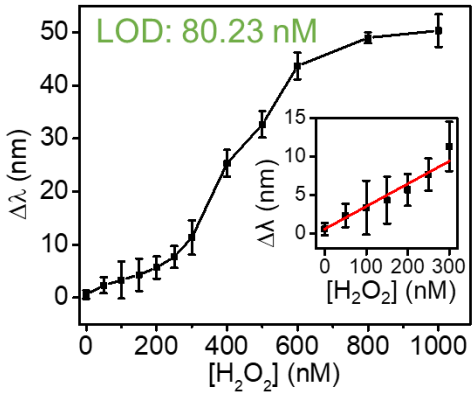

Figure 6.13 LSPR shifts of AuNUs-13 as a function of H_2O_2 concentration. Inset: the response at a low concentration range.

6.4 Conclusion

In summary, we reported rapid etching of AuNUs by TMB^+ under mild conditions. The reaction conditions including time, pH, and surface ligands were also optimized. All CTA^+, TMB^+, and Br^- molecules were important in etching AuNUs. Although the blue color of TMB^+ at low concentrations failed to be discerned with the naked eyes, nanomolar level TMB^+ can still cause vivid color changing of AuNUs solution by etching. With these observes, we developed a new one-step colorimetric biosensing platform for H_2O_2 detection by TMB^+-mediated etching of AuNUs. This work has expanded TMB^+-mediated etching of gold nanomaterials and is useful for improving plasmonic biosensors.

Chapter 7 Conclusions and Future Work

7.1 Conclusions and Original Contributions

DNA and metal ion mediated modification of nanomaterials has produced a wide variety of multifunctional composite complexes. In this thesis, I explored the direct adsorption of PS-modified DNA on GO, and PO DNA on Ti_2C MXene. In addition, I explored the various applications of Fe^{2+} mediated nanoshells in AuNP-based colorimetric sensors.

In Chapter 2, I have systematically studied the adsorption of PS DNA on GO mediated by Na^+ and Mg^{2+}. By using oligonucleotides displacement experiments, PS DNA strands were confirmed to have stronger binding affinities than the same sequenced PO DNA on GO. Both washing experiments and MD simulations showed that the sulfur atoms could have stronger VDW forces. By comparing different homo oligonucleotides, poly-C DNA, in general, has a high affinity to the GO surface, and PS poly-C DNA can adsorb even stronger, making it an ideal anchoring sequence on GO for functionalization. With this knowledge, non-covalent functionalization of GO with a diblock DNA is demonstrated, where a PS poly-C block is used to anchor on the surface and the other block is for hybridization with the target DNA. This conjugate achieves better hybridization than the PO DNA of the same sequence for hybridization with the complementary DNA.

In Chapter 3, I have discovered that Mn^{2+} can promote DNA adsorption on unmodified Ti_2C MXene via interactions with the phosphate backbone. The displacement experiments by denaturing or competing molecules indicated that neither VDW forces nor hydrogen bonding contributed much to DNA adsorption. In comparison with previously reported methods, a record high DNA adsorption capacity (298 nM 12mer DNA on 20 μg/ml Ti_2C MXene) was reached. In addition, delayed DNA desorption was observed by adding inorganic phosphate due to the formation of manganese phosphate to extract Mn^{2+} gradually from the DNA/MXene complex. Finally, DNA-induced DNA desorption from the Ti_2C MXene can hardly distinguish the complementary DNA from a random DNA, which is very different from GO. This difference is likely due to the distinct surface chemistry between the MXene and GO.

In Chapter 4, I grew a DNA/Fe shell on DNA-functionalized AuNPs. The high local DNA density on AuNPs make the nucleation of DNA/Fe CP much easier. As a result, the number of DNA oligonucleotides required for CPs formation was dramatically decreased by 98%. Since both the core and shell can be selectively etched, this hybrid material allowed potential drug loading and colorimetric sensing applications. With low DNA concentration, the AuNPs were trapped in merged DNA/Fe CP shells. This can be utilized for the colorimetric detection of phosphate. The phosphate is an essential plant nutrient and

a major component of fertilizers. This sensor may be helpful in monitoring phosphate levels in water. In addition, these DNA/Fe CPs are promising in oligonucleotide drug deliveries.

In Chapter 5, for the first time, we prepared metal phosphate FeP coatings directly on AuNPs. Using citrate-capped AuNPs as peroxidase-mimicking enzymes to design biosensors is hindered by their low catalytic activity and poor colloidal stability, resulting in limited sensitivity and large variations. The growth of an incomplete FeP shell on AuNPs can boot the peroxidase-like activity by up to 20-fold. By comparing the activities of FeP shells on various surfaces, the Au/FeP interface was found to be critical for activity enhancements. The inhibited activity caused by the strong capping MCH ligands also reflected the importance of the Au/FeP interface. In addition, the growth of crystallized FeP nearby DNA strands could also be affected. Moreover, a FeP shell can stabilize AuNPs against freezing and a high NaCl concentration of 1 M. Other tested transition metal phosphates failed to enhance the peroxidase-like activity of AuNPs. Therefore, a Fe^{2+} sensor was designed with a detection limit of 0.41 μM.

In chapter 6, I developed a new colorimetric biosensing platform with AuNUs. The morphology-dependent LSPR phenomenon of gold nanomaterials is widely utilized for sensors. One of the successful sensors is the gold nanoparticle-etching-based colorimetric sensor. In previous work, TMB^{2+} was found to etch AuNRs quantitatively and efficiently, leading to multiple color changes. However, the preparation of TMB^{2+} needs the extra addition of a strong acid solution. As a result, the AuNR-etching-based sensors always need multiple steps and acid conditions, which limits their applications. Unlike AuNRs, the etching of AuNUs can happen under mild conditions in the existence of TMB^{+} at pH 6. Such mild reaction conditions also ensured that the AuNUs etching process could happen without disrupting the activities of many natural proteins. As a byproduct of many enzymatic reactions, H_2O_2 is a popular target of many sensors. In this paper, a one-step colorimetric detection of H_2O_2 was realized based on the TMB^{+}-mediated etching of AuNUs. In this reaction, the oxidation of TMB substrate and the etching of AuNUs happened simultaneously in the presence of HRP and H_2O_2. In addition, the AuNUs-etching-based sensors were also fast (in 30 min) and sensitive. The sensitivity limit for H_2O_2 detection is 80 nM, which is ~7-fold more sensitive than the previous colorimetric detection.[327]

7.2 Future Work

The results presented in this thesis have proved that the DNA phosphate backbone is critical for multivalent ion mediated adsorption on GO and Ti_2C MXene. Moreover, the results about AuNP-based sensors also have shown that DNA/metal CPs hold great potential for sensing. Several future research directions could be carried on.

First, mechanistic work is still needed to understand multivalent metal ion mediated DNA adsorption on nanomaterials. By now, my experiments were mainly conducted at room temperature and physiological pH. Recently, our group found that temperature can direct the region of DNA oligonucleotide adsorption on GO.[55] Therefore, to further understand multivalent ion mediated DNA adsorption, more experiments could be conducted under different pH or temperature conditions.

Second, the stability of DNA/Fe CPs might be a problem in applications. There are two main methods to improve the stability of DNA/Fe CPs: surface coating and enhancement of coordination strength. Because SiO_2 has been widely used to stabilize AuNP@DNA, a possibility is to apply a SiO_2 layer on DNA/Fe CP surfaces. The DNA-Fe coordination strength is dependent on DNA sequences. Therefore, DNA sequences are needed to be optimized, especially those that can form i-motif or G-quadruplex structures.

Third, exploring DNA/Fe CP coatings on other surfaces. As mentioned in Chapter 4, the introduction of DNA-rich surfaces could significantly facilitate the DNA/Fe formation reaction. In addition, more functionalities could be brought with the various templates. Besides AuNPs, it should be possible to grow DNA/Fe CPs on Fe_3O_4 NPs and GO, since both nanomaterials are good platforms for DNA adsorption. Both nanomaterials have useful properties. For example, Fe_3O_4 NPs are magnetic and are an important peroxidase-like nanozyme. Our group has developed a series of molecularly imprinted polymers (MIPs) with functional DNAs in the past few years.[328-329] The molecularly imprinted DNA/Fe CPs could be grown on Fe_3O_4 nanozymes. Compared with traditional MIPs, no toxic initiators are involved in forming the DNA/Fe based MIPs. As a result, they are more environment-friendly and biocompatible.

Finally, new DNA/metal CPs could be developed by substituting the metal ion. Besides Fe^{2+}, I wish to investigate other metal ions such as Cu^{2+}. More kinds of DNA/metal hybrids with different properties could be synthesized by substituting metal ions.

References

1. Seeman, N. C., Nucleic Acid Junctions and Lattices. *J. Theor. Biol.* **1982,** *99* (2), 237-247.

2. Stulz, E.; Clever, G.; Shionoya, M.; Mao, C., DNA in a Modern World. *Chem. Soc. Rev.* **2011,** *40* (12), 5633-5635.

3. Madsen, M.; Gothelf, K. V., Chemistries for DNA Nanotechnology. *Chem. Rev.* **2019,** *119* (10), 6384-6458.

4. Choi, J.; Majima, T., Conformational Changes of Non-B DNA. *Chem. Soc. Rev.* **2011,** *40* (12), 5893-5909.

5. Yao, G.; Li, J.; Li, Q.; Chen, X.; Liu, X.; Wang, F.; Qu, Z.; Ge, Z.; Narayanan, R. P.; Williams, D.; Pei, H.; Zuo, X.; Wang, L.; Yan, H.; Feringa, B. L.; Fan, C., Programming Nanoparticle Valence Bonds with Single-Stranded DNA Encoders. *Nat. Mater.* **2020,** *19* (7), 781-788.

6. Wilner, O. I.; Willner, I., Functionalized DNA Nanostructures. *Chem. Rev.* **2012,** *112* (4), 2528-2556.

7. Rosi, N. L.; Mirkin, C. A., Nanostructures in Biodiagnostics. *Chem. Rev.* **2005,** *105* (4), 1547-1562.

8. Chen, Z.; Liu, C.; Cao, F.; Ren, J.; Qu, X., DNA Metallization: Principles, Methods, Structures, and Applications. *Chem. Soc. Rev.* **2018,** *47* (11), 4017-4072.

9. Liu, J., Adsorption of DNA onto Gold Nanoparticles and Graphene Oxide: Surface Science and Applications. *Phys. Chem. Chem. Phys.* **2012,** *14* (30), 10485-96.

10. Urdaneta, E. C.; Beckmann, B. M., Fast and Unbiased Purification of RNA-protein Complexes After UV Cross-linking. *Methods* **2020,** *178*, 72-82.

11. Iztok, T.; Jakob, K., Interactions of Metal Ions with DNA, Its Constituents and Derivatives, which may be Relevant for Anticancer Research. *Curr. Trends Med. Chem.* **2011,** *11* (21), 2661-2687.

12. Sigel, R. K. O.; Sigel, H., A Stability Concept for Metal Ion Coordination to Single-Stranded Nucleic Acids and Affinities of Individual Sites. *Acc. Chem. Res.* **2010,** *43* (7), 974-984.

13. Zhou, W.; Saran, R.; Liu, J., Metal Sensing by DNA. *Chem Rev* **2017,** *117* (12), 8272-8325.

14. Eichhorn, G. L.; Shin, Y. A., Interaction of Metal Ions with Polynucleotides and Related Compounds. XII. The Relative Effect of Various Metal Ions on DNA Helicity. *J. Am. Chem. Soc.* **1968,** *90* (26), 7323-7328.

15. Jia, S.; Wang, J.; Xie, M.; Sun, J.; Liu, H.; Zhang, Y.; Chao, J.; Li, J.; Wang, L.; Lin, J.; Gothelf, K. V.; Fan, C., Programming DNA Origami Patterning with Non-canonical DNA-based Metallization Reactions. *Nat. Commun.* **2019,** *10* (1), 5597.

16. Liu, B.; Liu, J., Methods for Preparing DNA-functionalized Gold Nanoparticles, a Key Reagent of Bioanalytical Chemistry. *Anal. Methods* **2017,** *9* (18), 2633-2643.

17. Oberemok, V. V.; Laikova, K. V.; Repetskaya, A. I.; Kenyo, I. M.; Gorlov, M. V.; Kasich, I. N.; Krasnodubets, A. M.; Gal'chinsky, N. V.; Fomochkina, II; Zaitsev, A. S.; Bekirova, V. V.; Seidosmanova, E. E.; Dydik, K. I.; Meshcheryakova, A. O.; Nazarov, S. A.; Smagliy, N. N.; Chelengerova, E. L.; Kulanova, A. A.; Deri, K.; Subbotkin, M. V.; Useinov, R. Z.; Shumskykh, M. N.; Kubyshkin, A. V., A Half-Century History of Applications of Antisense Oligonucleotides in Medicine, Agriculture and Forestry: We Should Continue the Journey. *Molecules* **2018,** *23* (6).

18. Hu, Q.; Li, H.; Wang, L.; Gu, H.; Fan, C., DNA Nanotechnology-Enabled Drug Delivery Systems. *Chem. Rev.* **2018**.

19. Roberts, T. C.; Langer, R.; Wood, M. J. A., Advances in Oligonucleotide Drug Delivery. *Nat. Rev. Drug Discovery* **2020,** *19* (10), 673-694.

20. Liang, H.; Zhang, X. B.; Lv, Y. F.; Gong, L.; Wang, R. W.; Zhu, X. Y.; Yang, R. H.; Tan, W. H., Functional DNA-Containing Nanomaterials: Cellular Applications in Biosensing, Imaging, and Targeted Therapy. *Acc. Chem. Res.* **2014,** *47* (6), 1891-1901.

21. Cruse, W. B. T.; Salisbury, S. A.; Brown, T.; Cosstick, R.; Eckstein, F.; Kennard, O., Chiral Phosphorothioate Analogues of B-DNA: The Crystal Structure of Rp-d¦Gp(S)CpGp(S)CpGp(S)C¦. *J. Mol. Biol.* **1986,** *192* (4), 891-905.

22. Ma, N.; Sargent, E. H.; Kelley, S. O., One-Step DNA-Programmed Growth of Luminescent and Biofunctionalized Nanocrystals. *Nat Nano* **2009,** *4* (2), 121-125.

23. Lee, J. H.; Wong, N. Y.; Tan, L. H.; Wang, Z.; Lu, Y., Controlled Alignment of Multiple Proteins and Nanoparticles with Nanometer Resolution via Backbone-Modified Phosphorothioate DNA and Bifunctional Linkers. *J. Am. Chem. Soc.* **2010,** *132* (26), 8906-8908.

24. Lee, J. H.; Wernette, D. P.; Yigit, M. V.; Liu, J.; Wang, Z.; Lu, Y., Site-Specific Control of Distances between Gold Nanoparticles Using Phosphorothioate Anchors on DNA and a Short Bifunctional Molecular Fastener. *Angew. Chem. Int. Ed.* **2007,** *46* (47), 9006-9010.

25. Liu, B.; Liu, J., Freezing Directed Construction of Bio/Nano Interfaces: Reagentless Conjugation, Denser Spherical Nucleic Acids, and Better Nanoflares. *J. Am. Chem. Soc.* **2017,** *139* (28), 9471-9474.

26. Zhao, D.; Kong, Y.; Zhao, S.; Xing, H., Engineering Functional DNA–Protein Conjugates for Biosensing, Biomedical, and Nanoassembly Applications. *Top. Curr. Chem.* **2020,** *378* (3), 41.

27. Zhang, X.; Gouriye, T.; Göeken, K.; Servos, M. R.; Gill, R.; Liu, J., Toward Fast and Quantitative Modification of Large Gold Nanoparticles by Thiolated DNA: Scaling of Nanoscale Forces, Kinetics, and the Need for Thiol Reduction. *J. Phys. Chem. C* **2013,** *117* (30), 15677-15684.

28. Samanta, A.; Medintz, I. L., Nanoparticles and DNA - a Powerful and Growing Functional Combination in Bionanotechnology. *Nanoscale* **2016,** *8* (17), 9037-9095.

29. Bock, L. C.; Griffin, L. C.; Latham, J. A.; Vermaas, E. H.; Toole, J. J., Selection of Single-stranded DNA Molecules that Bind and Inhibit Human Thrombin. *Nature* **1992,** *355* (6360), 564-566.

30. Li, L.; Xing, H.; Zhang, J.; Lu, Y., Functional DNA Molecules Enable Selective and Stimuli-Responsive Nanoparticles for Biomedical Applications. *Acc. Chem. Res.* **2019,** *52* (9), 2415-2426.

31. Pei, H.; Zuo, X.; Zhu, D.; Huang, Q.; Fan, C., Functional DNA Nanostructures for Theranostic Applications. *Acc. Chem. Res.* **2014,** *47* (2), 550-559.

32. Rothemund, P. W. K., Folding DNA to Create Nanoscale Shapes and Patterns. *Nature* **2006,** *440* (7082), 297-302.

33. Kallenbach, N. R.; Ma, R.-I.; Seeman, N. C., An Immobile Nucleic Acid Junction Constructed from Oligonucleotides. *Nature* **1983,** *305* (5937), 829-831.

34. Dey, S.; Fan, C.; Gothelf, K. V.; Li, J.; Lin, C.; Liu, L.; Liu, N.; Nijenhuis, M. A. D.; Saccà, B.; Simmel, F. C.; Yan, H.; Zhan, P., DNA Origami. *Nat. Rev. Dis. Primers* **2021,** *1* (1), 13.

35. Rogers, W. B.; Shih, W. M.; Manoharan, V. N., Using DNA to Program the Self-assembly of Colloidal Nanoparticles and Microparticles. *Nat. Rev. Mater.* **2016,** *1* (3), 16008.

36. Liu, J.; Lu, Y., Fast Colorimetric Sensing of Adenosine and Cocaine Based on a General Sensor Design Involving Aptamers and Nanoparticles. *Angew. Chem., Int. Ed.* **2006,** *45* (1), 90-94.

37. Naguib, M.; Mochalin, V. N.; Barsoum, M. W.; Gogotsi, Y., 25th Anniversary Article: MXenes: A New Family of Two-dimensional Materials. *Adv. Mater.* **2014,** *26* (7), 992-1005.

38. Lin, H.; Chen, Y.; Shi, J., Insights into 2D MXenes for Versatile Biomedical Applications: Current Advances and Challenges Ahead. *Adv. Sci.* **2018,** *5* (10), 1800518.

39. Tang, L.; Wang, Y.; Li, J., The Graphene/Nucleic Acid Nanobiointerface. *Chem. Soc. Rev.* **2015,** *44* (19), 6954-6980.

40. Saha, K.; Agasti, S. S.; Kim, C.; Li, X.; Rotello, V. M., Gold Nanoparticles in Chemical and Biological Sensing. *Chem. Rev.* **2012,** *112* (5), 2739-2779.

41. Yu, W.; Sisi, L.; Haiyan, Y.; Jie, L., Progress in the Functional Modification of Graphene/graphene Oxide: A Review. *RSC Adv.* **2020,** *10* (26), 15328-15345.

42. Ahmad, R. T. M.; Hong, S.-H.; Shen, T.-Z.; Song, J.-K., Water-assisted Stable Dispersal of Graphene Oxide in Non-dispersible Solvents and Skin Formation on the GO Dispersion. *Carbon* **2016,** *98*, 188-194.

43. Wang, M.; Niu, Y.; Zhou, J.; Wen, H.; Zhang, Z.; Luo, D.; Gao, D.; Yang, J.; Liang, D.; Li, Y., The Dispersion and Aggregation of Graphene Oxide in Aqueous Media. *Nanoscale* **2016,** *8* (30), 14587-14592.

44. Sun, H.; Ren, J.; Qu, X., Carbon Nanomaterials and DNA: from Molecular Recognition to Applications. *Acc. Chem. Res.* **2016,** *49* (3), 461-470.

45. Chen, Y.; Tan, C.; Zhang, H.; Wang, L., Two-dimensional Graphene Analogues for Biomedical Applications. *Chem. Soc. Rev.* **2015,** *44* (9), 2681-2701.

46. Liu, B.; Sun, Z.; Zhang, X.; Liu, J., Mechanisms of DNA Sensing on Graphene Oxide. *Anal. Chem.* **2013,** *85* (16), 7987-93.

47. Huang, Z.; Zhao, Y.; Liu, B.; Guan, S.; Liu, J., Stronger Adsorption of Phosphorothioate DNA Oligonucleotides on Graphene Oxide by van der Waals Forces. *Langmuir* **2020,** *36* (45), 13708-13715.

48. Lopez, A.; Liu, J., Covalent and Noncovalent Functionalization of Graphene Oxide with DNA for Smart Sensing. *Adv. Intell. Syst.* **2020,** *2* (11), 2000123.

49. Liu, B.; Salgado, S.; Maheshwari, V.; Liu, J., DNA Adsorbed on Graphene and Graphene Oxide: Fundamental Interactions, Desorption and Applications. *Curr. Opin. Colloid Interface Sci.* **2016,** *26*, 41-49.

50. Huang, Z.; Liu, J., Length-Dependent Diblock DNA with Poly-cytosine (Poly-C) as High-Affinity Anchors on Graphene Oxide. *Langmuir* **2018,** *34* (3), 1171-1177.

51. Huang, P.-J. J.; Liu, J., DNA-Length-Dependent Fluorescence Signaling on Graphene Oxide Surface. *Small* **2012,** *8* (7), 977-983.

52. Xu, Z.; Lei, X.; Tu, Y.; Tan, Z.-J.; Song, B.; Fang, H., Dynamic Cooperation of Hydrogen Binding and π Stacking in ssDNA Adsorption on Graphene Oxide. *Chem. - Eur. J.* **2017,** *23* (53), 13100-13104.

53. Kim, H. S.; Farmer, B. L.; Yingling, Y. G., Effect of Graphene Oxidation Rate on Adsorption of Poly-Thymine Single Stranded DNA. *Adv. Mater. Interfaces* **2017,** *4* (8), 1601168.

54. Reina, G.; Chau, N. D. Q.; Nishina, Y.; Bianco, A., Graphene Oxide Size and Oxidation Degree Govern its Supramolecular Interactions with siRNA. *Nanoscale* **2018,** *10* (13), 5965-5974.

55. Liu, B.; Zhao, Y.; Jia, Y.; Liu, J., Heating Drives DNA to Hydrophobic Regions While Freezing Drives DNA to Hydrophilic Regions of Graphene Oxide for Highly Robust Biosensors. *J. Am. Chem. Soc.* **2020,** *142* (34), 14702-14709.

56. Lu, C.; Huang, P.-J. J.; Liu, B.; Ying, Y.; Liu, J., Comparison of Graphene Oxide and Reduced Graphene Oxide for DNA Adsorption and Sensing. *Langmuir* **2016,** *32* (41), 10776-10783.

57. Wu, M.; Kempaiah, R.; Huang, P.-J. J.; Maheshwari, V.; Liu, J., Adsorption and Desorption of DNA on Graphene Oxide Studied by Fluorescently Labeled Oligonucleotides. *Langmuir* **2011,** *27* (6), 2731-2738.

58. Tang, L.; Wang, Y.; Liu, Y.; Li, J., DNA-Directed Self-Assembly of Graphene Oxide with Applications to Ultrasensitive Oligonucleotide Assay. *ACS Nano* **2011,** *5* (5), 3817-3822.

59. Lukatskaya, M. R.; Mashtalir, O.; Ren, C. E.; Dall'Agnese, Y.; Rozier, P.; Taberna, P. L.; Naguib, M.; Simon, P.; Barsoum, M. W.; Gogotsi, Y., Cation Intercalation and High Volumetric Capacitance of Two-Dimensional Titanium Carbide. *Science* **2013,** *341* (6153), 1502-1505.

60. Zhu, J.; Ha, E.; Zhao, G.; Zhou, Y.; Huang, D.; Yue, G.; Hu, L.; Sun, N.; Wang, Y.; Lee, L. Y. S.; Xu, C.; Wong, K.-Y.; Astruc, D.; Zhao, P., Recent Advance in MXenes: A Promising 2D Material for Catalysis, Sensor and Chemical Adsorption. *Coord. Chem. Rev.* **2017,** *352*, 306-327.

61. Gao, G.; O'Mullane, A. P.; Du, A., 2D MXenes: A New Family of Promising Catalysts for the Hydrogen Evolution Reaction. *ACS Catal.* **2017,** *7* (1), 494-500.

62. Rozmysłowska-Wojciechowska, A.; Wojciechowski, T.; Ziemkowska, W.; Chlubny, L.; Olszyna, A.; Jastrzębska, A. M., Surface Interactions between 2D Ti_3C_2/Ti_2C MXenes and Lysozyme. *Appl. Surf. Sci.* **2019,** *473*, 409-418.

63. Xu, B.; Zhu, M.; Zhang, W.; Zhen, X.; Pei, Z.; Xue, Q.; Zhi, C.; Shi, P., Ultrathin MXene-Micropattern-Based Field-Effect Transistor for Probing Neural Activity. *Adv. Mater.* **2016,** *28* (17), 3333-3339.

64. Kumar, S.; Lei, Y.; Alshareef, N. H.; Quevedo-Lopez, M. A.; Salama, K. N., Biofunctionalized Two-dimensional Ti_3C_2 MXenes for Ultrasensitive Detection of Cancer Biomarker. *Biosens. Bioelectron.* **2018,** *121*, 243-249.

65. Meng, F.; Seredych, M.; Chen, C.; Gura, V.; Mikhalovsky, S.; Sandeman, S.; Ingavle, G.; Ozulumba, T.; Miao, L.; Anasori, B.; Gogotsi, Y., MXene Sorbents for Removal of Urea from Dialysate: A Step toward the Wearable Artificial Kidney. *ACS Nano* **2018,** *12* (10), 10518-10528.

66. Zhang, Q.; Wang, F.; Zhang, H.; Zhang, Y.; Liu, M.; Liu, Y., Universal Ti_3C_2 MXenes Based Self-Standard Ratiometric Fluorescence Resonance Energy Transfer Platform for Highly Sensitive Detection of Exosomes. *Anal. Chem.* **2018,** *90* (21), 12737-12744.

67. Wang, S.; Wei, S.; Wang, S.; Zhu, X.; Lei, C.; Huang, Y.; Nie, Z.; Yao, S., A Chimeric DNA-functionalized Titanium Carbide MXenes for Simultaneous Mapping of Dual Cancer Biomarkers in Living Cells. *Anal. Chem.* **2018,** *91* (21), 1651-1658.

68. Satheeshkumar, E.; Makaryan, T.; Melikyan, A.; Minassian, H.; Gogotsi, Y.; Yoshimura, M., One-step Solution Processing of Ag, Au and Pd@MXene Hybrids for SERS. *Sci. Rep.* **2016,** *6*, 32049.

69. Yang, X.; Feng, M.; Xia, J.; Zhang, F.; Wang, Z., An Electrochemical Biosensor Based on AuNPs/Ti_3C_2 MXene Three-dimensional Nanocomposite for MicroRNA-155 Detection by Exonuclease III-aided Cascade Target Recycling. *J. Electroanal. Chem.* **2020,** *878*, 114669.

70. Ghosh, S. K.; Pal, T., Interparticle Coupling Effect on the Surface Plasmon Resonance of Gold Nanoparticles: From Theory to Applications. *Chem. Rev.* **2007,** *107* (11), 4797-4862.

71. Eustis, S.; El-Sayed, M. A., Why Gold Nanoparticles are More Precious than Pretty Gold: Noble Metal Surface Plasmon Resonance and Its Enhancement of the Radiative and Nonradiative Properties of Nanocrystals of Different Shapes. *Chem. Soc. Rev.* **2006,** *35* (3), 209-217.

72. Zong, C.; Xu, M.; Xu, L.-J.; Wei, T.; Ma, X.; Zheng, X.-S.; Hu, R.; Ren, B., Surface-Enhanced Raman Spectroscopy for Bioanalysis: Reliability and Challenges. *Chem. Rev.* **2018**.

73. Jones, M. R.; Seeman, N. C.; Mirkin, C. A., Programmable Materials and the Nature of the DNA Bond. *Science* **2015,** *347* (6224), 1260901.

74. Cutler, J. I.; Auyeung, E.; Mirkin, C. A., Spherical Nucleic Acids. *J. Am. Chem. Soc.* **2012,** *134* (3), 1376-1391.

75. Kimura-Suda, H.; Petrovykh, D. Y.; Tarlov, M. J.; Whitman, L. J., Base-Dependent Competitive Adsorption of Single-Stranded DNA on Gold. *J. Am. Chem. Soc.* **2003,** *125* (30), 9014-9015.

76. Opdahl, A.; Petrovykh, D. Y.; Kimura-Suda, H.; Tarlov, M. J.; Whitman, L. J., Independent Control of Grafting Density and Conformation of Single-Stranded DNA Brushes. *Proc. Natl. Acad. Sci. U. S. A.* **2007,** *104* (1), 9-14.

77. Herne, T. M.; Tarlov, M. J., Characterization of DNA Probes Immobilized on Gold Surfaces. *J. Am. Chem. Soc.* **1997,** *119* (38), 8916-8920.

78. Hao, Y.; Li, Y.; Song, L.; Deng, Z., Flash Synthesis of Spherical Nucleic Acids with Record DNA Density. *J. Am. Chem. Soc.* **2021,** *143* (8), 3065-3069.

79. Liu, B.; Liu, J., Interface-Driven Hybrid Materials Based on DNA-Functionalized Gold Nanoparticles. *Matter* **2019,** *1* (4), 825-847.

80. Zhang, X.; Servos, M. R.; Liu, J., Instantaneous and Quantitative Functionalization of Gold Nanoparticles with Thiolated DNA Using A pH-Assisted and Surfactant-Free Route. *J. Am. Chem. Soc.* **2012,** *134* (17), 7266-9.

81. Liu, B.; Wu, T.; Huang, Z.; Liu, Y.; Liu, J., Freezing-Directed Stretching and Alignment of DNA Oligonucleotides. *Angew. Chem. Int. Ed.* **2019,** *58* (7), 2109-2113.

82. Van Vleet, M. J.; Weng, T.; Li, X.; Schmidt, J. R., In Situ, Time-Resolved, and Mechanistic Studies of Metal–Organic Framework Nucleation and Growth. *Chem. Rev.* **2018**.

83. Liu, X.; Zhou, Y.; Zhang, J.; Tang, L.; Luo, L.; Zeng, G., Iron Containing Metal–Organic Frameworks: Structure, Synthesis, and Applications in Environmental Remediation. *ACS Appl. Mater. Interfaces* **2017,** *9* (24), 20255-20275.

84. Wang, S.; McGuirk, C. M.; d'Aquino, A.; Mason, J. A.; Mirkin, C. A., Metal–Organic Framework Nanoparticles. *Adv. Mater.* **2018,** *30* (37), 1800202.

85. Qiu, T.; Gao, S.; Liang, Z.; Wang, D.-G.; Tabassum, H.; Zhong, R.; Zou, R., Pristine Hollow Metal–Organic Frameworks: Design, Synthesis and Application. *Angew. Chem. Int. Ed.* **2020,** *n/a* (n/a).

86. Xu, L.; Zhang, P.; Liu, Y.; Fang, X.; Zhang, Z.; Liu, Y.; Peng, L.; Liu, J., Continuously Tunable Nucleotide/Lanthanide Coordination Nanoparticles for DNA Adsorption and Sensing. *ACS Omega* **2018,** *3* (8), 9043-9051.

87. Liu, B.; Zhang, J.; Li, L., Metal–DNA Coordination-Driven Self-Assembly: A Conceptual Methodology to Expand the Repertoire of DNA Nanobiotechnology. *Chem. - Eur. J.* **2019,** *25* (59), 13452-13457.

88. He, Y.; Lopez, A.; Zhang, Z.; Chen, D.; Yang, R.; Liu, J., Nucleotide and DNA Coordinated Lanthanides: From Fundamentals to Applications. *Coord. Chem. Rev.* **2019,** *387*, 235-248.

89. Li, M.; Wang, C.; Di, Z.; Li, H.; Zhang, J.; Xue, W.; Zhao, M.; Zhang, K.; Zhao, Y.; Li, L., Engineering Multifunctional DNA Hybrid Nanospheres through Coordination-Driven Self-Assembly. *Angew. Chem. Int. Ed.* **2019,** *58* (5), 1350-1354.

90. Lopez, A.; Liu, J., Self-Assembly of Nucleobase, Nucleoside and Nucleotide Coordination Polymers: From Synthesis to Applications. *ChemNanoMat* **2017,** *3* (10), 670-684.

91. Wu, J.; Du, F.; Zhang, P.; Khan, I. A.; Chen, J.; Liang, Y., Thermodynamics of the Interaction of Aluminum Ions with DNA: Implications for the Biological Function of Aluminum. *J. Inorg. Biochem.* **2005,** *99* (5), 1145-1154.

92. Kanellis, V. G.; dos Remedios, C. G., A Review of Heavy Metal Cation Binding to Deoxyribonucleic Acids for the Creation of Chemical Sensors. *Biophys. Rev.* **2018,** *10* (5), 1401-1414.

93. Wei, H.; Li, B.; Du, Y.; Dong, S.; Wang, E., Nucleobase−Metal Hybrid Materials: Preparation of Submicrometer-Scale, Spherical Colloidal Particles of Adenine−Gold(III) via a Supramolecular Hierarchical Self-Assembly Approach. *Chem. Mater.* **2007,** *19* (12), 2987-2993.

94. Tan, H.; Chen, Y., Ag^+-enhanced Fluorescence of Lanthanide/nucleotide Coordination Polymers and Ag^+ Sensing. *Chem. Commun.* **2011,** *47* (45), 12373-12375.

95. Gao, R.-R.; Shi, S.; Li, Y.-J.; Wumaier, M.; Hu, X.-C.; Yao, T.-M., Coordination Polymer Nanoparticles from Nucleotide and Lanthanide Ions as a Versatile Platform for Color-tunable Luminescence and Integrating Boolean Logic Operations. *Nanoscale* **2017,** *9* (27), 9589-9597.

96. Cotruvo, J. A.; Featherston, E. R.; Mattocks, J. A.; Ho, J. V.; Laremore, T. N., Lanmodulin: A Highly Selective Lanthanide-Binding Protein from a Lanthanide-Utilizing Bacterium. *J. Am. Chem. Soc.* **2018,** *140* (44), 15056-15061.

97. Nishiyabu, R.; Hashimoto, N.; Cho, T.; Watanabe, K.; Yasunaga, T.; Endo, A.; Kaneko, K.; Niidome, T.; Murata, M.; Adachi, C.; Katayama, Y.; Hashizume, M.; Kimizuka, N., Nanoparticles of Adaptive

Supramolecular Networks Self-Assembled from Nucleotides and Lanthanide Ions. *J. Am. Chem. Soc.* **2009,** *131* (6), 2151-2158.

98. Liu, B.; Hu, F.; Zhang, J.; Wang, C.; Li, L., A Biomimetic Coordination Nanoplatform for Controlled Encapsulation and Delivery of Drug-Gene Combinations. *Angew. Chem. Int. Ed.* **2019,** *58* (26), 8804-8808.

99. Liu, Y.; Liu, J., Growing a Nucleotide/Lanthanide Coordination Polymer Shell on Liposomes. *Langmuir* **2019,** *35* (34), 11217-11224.

100. Liang, H.; Liu, B.; Yuan, Q.; Liu, J., Magnetic Iron Oxide Nanoparticle Seeded Growth of Nucleotide Coordinated Polymers. *ACS Appl. Mater. Interfaces* **2016,** *8* (24), 15615-15622.

101. Qi, C.; Zhu, Y.-J.; Ding, G.-J.; Wu, J.; Chen, F., Solvothermal Synthesis of Hydroxyapatite Nanostructures with Various Morphologies Using Adenosine 5′-monophosphate Sodium Salt as an Organic Phosphorus Source. *RSC Adv.* **2015,** *5* (5), 3792-3798.

102. Lee, D.; Upadhye, K.; Kumta, P. N., Nano-sized Calcium Phosphate (CaP) Carriers for Non-viral Gene Deilvery. *Mater. Sci. Eng., B* **2012,** *177* (3), 289-302.

103. Wu, G.-J.; Zhou, L.-Z.; Wang, K.-W.; Chen, F.; Sun, Y.; Duan, Y.-R.; Zhu, Y.-J.; Gu, H.-C., Hydroxylapatite Nanorods: An Efficient and Promising Carrier for Gene Transfection. *J. Colloid Interface Sci.* **2010,** *345* (2), 427-432.

104. Wu, S.; Zhang, M.; Song, J.; Weber, S.; Liu, X.; Fan, C.; Wu, Y., Fine Customization of Calcium Phosphate Nanostructures with Site-Specific Modification by DNA Templated Mineralization. *ACS Nano* **2021,** *15* (1), 1555-1565.

105. Liu, X.; Jing, X.; Liu, P.; Pan, M.; Liu, Z.; Dai, X.; Lin, J.; Li, Q.; Wang, F.; Yang, S.; Wang, L.; Fan, C., DNA Framework-Encoded Mineralization of Calcium Phosphate. *Chem* **2020,** *6* (2), 472-485.

106. Li, D.; Fang, Z.; Duan, H.; Liang, L., Polydopamine-mediated Synthesis of Core–shell Gold@calcium Phosphate Nanoparticles for Enzyme Immobilization. *Biomater. Sci.* **2019,** *7* (7), 2841-2849.

107. Chai, F.; Wang, C.; Wang, T.; Li, L.; Su, Z., Colorimetric Detection of Pb2+ Using Glutathione Functionalized Gold Nanoparticles. *ACS Appl. Mater. Interfaces* **2010,** *2* (5), 1466-1470.

108. Hoang, M.; Huang, P.-J. J.; Liu, J., G-Quadruplex DNA for Fluorescent and Colorimetric Detection of Thallium(I). *ACS Sensors* **2016,** *1* (2), 137-143.

109. Zheng, B.; Cheng, S.; Liu, W.; Lam, M. H.; Liang, H., A Simple Colorimetric pH Alarm Constructed from DNA-gold Nanoparticles. *Anal. Chim. Acta* **2012,** *741*, 106-13.

110. Wang, H.; Rao, H.; Luo, M.; Xue, X.; Xue, Z.; Lu, X., Noble Metal Nanoparticles Growth-based Colorimetric Strategies: From Monocolorimetric to Multicolorimetric Sensors. *Coord. Chem. Rev.* **2019,** *398*, 113003.

111. Rao, H.; Xue, X.; Wang, H.; Xue, Z., Gold Nanorod Etching-based Multicolorimetric Sensors: Strategies and Applications. *J. Mater. Chem. C* **2019,** *7* (16), 4610-4621.

112. Ma, X.; He, S.; Qiu, B.; Luo, F.; Guo, L.; Lin, Z., Noble Metal Nanoparticle-Based Multicolor Immunoassays: An Approach toward Visual Quantification of the Analytes with the Naked Eye. *ACS Sensors* **2019,** *4* (4), 782-791.

113. Zhang, F.; Huang, P.-J. J.; Liu, J., Sensing Adenosine and ATP by Aptamers and Gold Nanoparticles: Opposite Trends of Color Change from Domination of Target Adsorption Instead of Aptamer Binding. *ACS Sensors* **2020,** *5* (9), 2885-2893.

114. Li, H.; Rothberg, L. J., Label-Free Colorimetric Detection of Specific Sequences in Genomic DNA Amplified by the Polymerase Chain Reaction. *J. Am. Chem. Soc.* **2004,** *126* (35), 10958-10961.

115. Li, H.; Rothberg, L., Colorimetric Detection of DNA Sequences Based on Electrostatic Interactions with Unmodified Gold Nanoparticles. *Proc. Natl. Acad. Sci. U. S. A.* **2004,** *101* (39), 14036-14039.

116. Liu, J.; Lu, Y., Accelerated Color Change of Gold Nanoparticles Assembled by DNAzymes for Simple and Fast Colorimetric Pb^{2+} Detection. *J. Am. Chem. Soc.* **2004,** *126* (39), 12298-12305.

117. Liu, J.; Lu, Y., Non-Base Pairing DNA Provides a New Dimension for Controlling Aptamer-Linked Nanoparticles and Sensors. *J. Am. Chem. Soc.* **2007,** *129* (27), 8634-8643.

118. Tan, L.; Chen, Z.; Zhang, C.; Wei, X.; Lou, T.; Zhao, Y., Colorimetric Detection of Hg^{2+} Based on the Growth of Aptamer-Coated AuNPs: The Effect of Prolonging Aptamer Strands. *Small* **2017,** *13* (14), 1603370.

119. Kang, F.; Hou, X.; Xu, K., Highly Sensitive Colorimetric Detection of Glucose in a Serum Based on DNA-embeded Au@Ag Core–shell Nanoparticles. *Nanotechnology* **2015,** *26* (40), 405707.

120. Samal, A. K.; Polavarapu, L.; Rodal-Cedeira, S.; Liz-Marzán, L. M.; Pérez-Juste, J.; Pastoriza-Santos, I., Size Tunable Au@Ag Core–Shell Nanoparticles: Synthesis and Surface-Enhanced Raman Scattering Properties. *Langmuir* **2013,** *29* (48), 15076-15082.

121. Kermanshahian, K.; Yadegar, A.; Ghourchian, H., Gold Nanorods Etching as a Powerful Signaling Process for Plasmonic Multicolorimetric Chemo-/Biosensors: Strategies and Applications. *Coord. Chem. Rev.* **2021,** *442*, 213934.

122. Wu, J.; Wang, X.; Wang, Q.; Lou, Z.; Li, S.; Zhu, Y.; Qin, L.; Wei, H., Nanomaterials with Enzyme-like Characteristics (Nanozymes): Next-Generation Artificial Enzymes (II). *Chem. Soc. Rev.* **2019,** *48* (4), 1004-1076.

123. Wei, H.; Wang, E., Nanomaterials with Enzyme-like Characteristics (Nanozymes): Next-Generation Artificial Enzymes. *Chem. Soc. Rev.* **2013,** *42* (14), 6060-6093.

124. Comotti, M.; Della Pina, C.; Matarrese, R.; Rossi, M., The Catalytic Activity of "Naked" Gold Particles. *Angew. Chem. Int. Ed.* **2004,** *43* (43), 5812-5815.

125. Gao, L.; Zhuang, J.; Nie, L.; Zhang, J.; Zhang, Y.; Gu, N.; Wang, T.; Feng, J.; Yang, D.; Perrett, S.; Yan, X., Intrinsic Peroxidase-like Activity of Ferromagnetic Nanoparticles. *Nat. Nanotechnol.* **2007,** *2*, 577.

126. Lee, S.; Tak, E.; Lee, J.; Rashid, M. A.; Murphy, M. P.; Ha, J.; Kim, S. S., Mitochondrial H_2O_2 Generated From Electron Transport Chain Complex I Stimulates Muscle Differentiation. *Cell Res.* **2011,** *21* (5), 817-834.

127. Sun, Y.; Wang, R.; Liu, X.; Shan, G.; Chen, Y.; Tong, T.; Liu, Y., Laser-induced Formation of Au/Pt Nanorods with Peroxidase Mimicking and SERS Enhancement Properties for Application to the Colorimetric Determination of H_2O_2. *Microchim. Acta* **2018,** *185* (9), 445.

128. Deng, H.-H.; Luo, B.-Y.; He, S.-B.; Chen, R.-T.; Lin, Z.; Peng, H.-P.; Xia, X.-H.; Chen, W., Redox Recycling-Triggered Peroxidase-Like Activity Enhancement of Bare Gold Nanoparticles for Ultrasensitive Colorimetric Detection of Rare-Earth Ce^{3+} Ion. *Anal. Chem.* **2019,** *91* (6), 4039-4046.

129. Han, L.; Li, C.; Zhang, T.; Lang, Q.; Liu, A., Au@Ag Heterogeneous Nanorods as Nanozyme Interfaces with Peroxidase-Like Activity and Their Application for One-Pot Analysis of Glucose at Nearly Neutral pH. *ACS Appl. Mater. Interfaces* **2015,** *7* (26), 14463-14470.

130. Luo, W.; Zhu, C.; Su, S.; Li, D.; He, Y.; Huang, Q.; Fan, C., Self-Catalyzed, Self-Limiting Growth of Glucose Oxidase-Mimicking Gold Nanoparticles. *ACS Nano* **2010,** *4* (12), 7451-7458.

131. Jv, Y.; Li, B.; Cao, R., Positively-charged Gold Nanoparticles as Peroxidiase Mimic and Their Application in Hydrogen Peroxide and Glucose Detection. *Chem. Commun.* **2010,** *46* (42), 8017-8019.

132. Hu, Y.; Cheng, H.; Zhao, X.; Wu, J.; Muhammad, F.; Lin, S.; He, J.; Zhou, L.; Zhang, C.; Deng, Y.; Wang, P.; Zhou, Z.; Nie, S.; Wei, H., Surface-Enhanced Raman Scattering Active Gold Nanoparticles with Enzyme-Mimicking Activities for Measuring Glucose and Lactate in Living Tissues. *ACS Nano* **2017,** *11* (6), 5558-5566.

133. Jiang, C.; Zhu, J.; Li, Z.; Luo, J.; Wang, J.; Sun, Y., Chitosan–gold Nanoparticles as Peroxidase Mimic and Their Application in Glucose Detection in Serum. *RSC Adv.* **2017,** *7* (70), 44463-44469.

134. Lou-Franco, J.; Das, B.; Elliott, C.; Cao, C., Gold Nanozymes: From Concept to Biomedical Applications. *Nano-Micro Letters* **2020,** *13* (1), 10.

135. Shah, J.; Purohit, R.; Singh, R.; Karakoti, A. S.; Singh, S., ATP-enhanced Peroxidase-like Activity of Gold Nanoparticles. *J. Colloid Interface Sci.* **2015,** *456*, 100-107.

136. Kumar, V.; Bano, D.; Singh, D. K.; Mohan, S.; Singh, V. K.; Hasan, S. H., Size-Dependent Synthesis of Gold Nanoparticles and Their Peroxidase-Like Activity for the Colorimetric Detection of Glutathione from Human Blood Serum. *ACS Sustainable Chemistry & Engineering* **2018,** *6* (6), 7662-7675.

137. Hizir, M. S.; Top, M.; Balcioglu, M.; Rana, M.; Robertson, N. M.; Shen, F.; Sheng, J.; Yigit, M. V., Multiplexed Activity of perAuxidase: DNA-Capped AuNPs Act as Adjustable Peroxidase. *Anal. Chem.* **2016,** *88* (1), 600-605.

138. Wang, S.; Chen, W.; Liu, A.-L.; Hong, L.; Deng, H.-H.; Lin, X.-H., Comparison of the Peroxidase-Like Activity of Unmodified, Amino-Modified, and Citrate-Capped Gold Nanoparticles. *ChemPhysChem* **2012,** *13* (5), 1199-1204.

139. Long, Y. J.; Li, Y. F.; Liu, Y.; Zheng, J. J.; Tang, J.; Huang, C. Z., Visual Observation of the Mercury-stimulated Peroxidase Mimetic Activity of Gold Nanoparticles. *Chem. Commun.* **2011,** *47* (43), 11939-11941.

140. Panferov, V. G.; Safenkova, I. V.; Zherdev, A. V.; Dzantiev, B. B., Urchin Peroxidase-mimicking Au@Pt Nanoparticles as a Label in Lateral Flow Immunoassay: Impact of Nanoparticle Composition on Detection Limit of Clavibacter Michiganensis. *Microchim. Acta* **2020,** *187* (5), 268.

141. Liu, J.; Cao, Z.; Lu, Y., Functional Nucleic Acid Sensors. *Chem. Rev.* **2009,** *109* (5), 1948-1998.

142. Wang, Y.; Li, Z.; Weber, T. J.; Hu, D.; Lin, C.-T.; Li, J.; Lin, Y., In Situ Live Cell Sensing of Multiple Nucleotides Exploiting DNA/RNA Aptamers and Graphene Oxide Nanosheets. *Anal. Chem.* **2013,** *85* (14), 6775-6782.

143. Yang, H.; Zhao, W.; Deng, S.; Zhang, K.; Zhao, Z.; Deng, R.; He, Q.; Li, J., Intrinsic Conformation-Induced Fluorescence Resonance Energy Transfer Aptasensor. *ACS Applied Bio Materials* **2020,** *3* (5), 2553-2559.

144. Langille, M. R.; Personick, M. L.; Zhang, J.; Mirkin, C. A., Defining Rules for the Shape Evolution of Gold Nanoparticles. *J. Am. Chem. Soc.* **2012,** *134* (35), 14542-14554.

145. Tan, L. H.; Xing, H.; Lu, Y., DNA as a Powerful Tool for Morphology Control, Spatial Positioning, and Dynamic Assembly of Nanoparticles. *Acc. Chem. Res.* **2014,** *47* (6), 1881-1890.

146. Giljohann, D. A.; Seferos, D. S.; Daniel, W. L.; Massich, M. D.; Patel, P. C.; Mirkin, C. A., Gold Nanoparticles for Biology and Medicine. *Angew. Chem., Int. Ed.* **2010,** *49* (19), 3280-3294.

147. Kushalkar, M. P.; Liu, B.; Liu, J., Promoting DNA Adsorption by Acids and Polyvalent Cations: Beyond Charge Screening. *Langmuir* **2020,** *36* (38), 11183-11195.

148. Lee, J.; Yim, Y.; Kim, S.; Choi, M.-H.; Choi, B.-S.; Lee, Y.; Min, D.-H., In-Depth Investigation of the Interaction Between DNA and Nano-Sized Graphene Oxide. *Carbon* **2016,** *97*, 92-98.

149. Chang, H.; Tang, L.; Wang, Y.; Jiang, J.; Li, J., Graphene Fluorescence Resonance Energy Transfer Aptasensor for the Thrombin Detection. *Anal. Chem.* **2010,** *82* (6), 2341-2346.

150. Liu, B.; Ma, L.; Huang, Z.; Hu, H.; Wu, P.; Liu, J., Janus DNA Orthogonal Adsorption of Graphene Oxide and Metal Oxide Nanoparticles Enabling Stable Sensing in Serum. *Mater. Horiz.* **2018,** *5* (1), 65-69.

151. Lu, C.-H.; Yang, H.-H.; Zhu, C.-L.; Chen, X.; Chen, G.-N., A Graphene Platform for Sensing Biomolecules. *Angew. Chem. Int. Ed.* **2009,** *48* (26), 4785-4787.

152. Wang, Y.; Tang, L.; Li, Z.; Lin, Y.; Li, J., In situ simultaneous monitoring of ATP and GTP using a graphene oxide nanosheet–based sensing platform in living cells. *Nature Protocols* **2014,** *9*, 1944.

153. Zhu, C.; Zeng, Z.; Li, H.; Li, F.; Fan, C.; Zhang, H., Single-Layer MoS_2-Based Nanoprobes for Homogeneous Detection of Biomolecules. *J. Am. Chem. Soc.* **2013,** *135* (16), 5998-6001.

154. Xi, Q.; Zhou, D.-M.; Kan, Y.-Y.; Ge, J.; Wu, Z.-K.; Yu, R.-Q.; Jiang, J.-H., Highly Sensitive and Selective Strategy for MicroRNA Detection Based on WS_2 Nanosheet Mediated Fluorescence Quenching and Duplex-Specific Nuclease Signal Amplification. *Anal. Chem.* **2014,** *86* (3), 1361-1365.

155. Ge, J.; Tang, L.-J.; Xi, Q.; Li, X.-P.; Yu, R.-Q.; Jiang, J.-H.; Chu, X., A WS_2 Nanosheet Based Sensing Platform for Highly Sensitive Detection of T4 Polynucleotide Kinase and Its Inhibitors. *Nanoscale* **2014,** *6* (12), 6866-6872.

156. Lu, C.; Huang, Z.; Liu, B.; Liu, Y.; Ying, Y.; Liu, J., Poly-cytosine DNA as a High-Affinity Ligand for Inorganic Nanomaterials. *Angew. Chem. Int. Ed.* **2017,** *56* (22), 6208-6212.

157. Ge, H.; Wang, D.; Pan, Y.; Guo, Y.; Li, H.; Zhang, F.; Zhu, X.; Li, Y.; Zhang, C.; Huang, L., Sequence-Dependent DNA Functionalization of Upconversion Nanoparticles and Their Programmable Assemblies. *Angew. Chem. Int. Ed.* **2020,** *59* (21), 8133-8137.

158. Zhou, Y.; Huang, Z.; Yang, R.; Liu, J., Selection and Screening of DNA Aptamers for Inorganic Nanomaterials. *Chem. - Eur. J.* **2018,** *24* (11), 2525-2532.

159. Zheng, M.; Jagota, A.; Semke, E. D.; Diner, B. A.; McLean, R. S.; Lustig, S. R.; Richardson, R. E.; Tassi, N. G., DNA-Assisted Dispersion and Separation of Carbon Nanotubes. *Nat. Mater.* **2003,** *2* (5), 338-42.

160. Zheng, M.; Jagota, A.; Strano, M. S.; Santos, A. P.; Barone, P.; Chou, S. G.; Diner, B. A.; Dresselhaus, M. S.; McLean, R. S.; Onoa, G. B.; Samsonidze, G. G.; Semke, E. D.; Usrey, M.; Walls, D. J., Structure-Based Carbon Nanotube Sorting by Sequence-Dependent DNA Assembly. *Science* **2003,** *302* (5650), 1545-8.

161. Tu, X.; Manohar, S.; Jagota, A.; Zheng, M., DNA Sequence Motifs for Structure-Specific Recognition and Separation of Carbon Nanotubes. *Nature* **2009,** *460*, 250.

162. Lopez, A.; Liu, B.; Huang, Z.; Zhang, F.; Liu, J., Fluorescein-Stabilized i-Motif DNA and Its Unfolding Leading to a Stronger Adsorption Affinity. *Langmuir* **2019,** *35* (36), 11932-11939.

163. Wang, L.; Zhang, Z.; Liu, B.; Liu, Y.; Lopez, A.; Wu, J.; Liu, J., Interfacing DNA Oligonucleotides with Calcium Phosphate and Other Metal Phosphates. *Langmuir* **2017,** *34*, 14975–14982.

164. Ryoo, S.-R.; Lee, J.; Yeo, J.; Na, H.-K.; Kim, Y.-K.; Jang, H.; Lee, J. H.; Han, S. W.; Lee, Y.; Kim, V. N.; Min, D.-H., Quantitative and Multiplexed MicroRNA Sensing in Living Cells Based on Peptide Nucleic Acid and Nano Graphene Oxide (PANGO). *ACS Nano* **2013,** *7* (7), 5882-5891.

165. Guo, S.; Du, D.; Tang, L.; Ning, Y.; Yao, Q.; Zhang, G.-J., PNA-Assembled Graphene Oxide for Sensitive and Selective Detection of DNA. *Analyst* **2013,** *138* (11), 3216-3220.

166. Huang, P.-J. J.; Liu, J., An Ultrasensitive Light-up Cu^{2+} Biosensor Using a New DNAzyme Cleaving a Phosphorothioate-Modified Substrate. *Anal. Chem.* **2016,** *88* (6), 3341-3347.

167. Zhou, W.; Wang, F.; Ding, J.; Liu, J., Tandem Phosphorothioate Modifications for DNA Adsorption Strength and Polarity Control on Gold Nanoparticles. *ACS Appl. Mater. Interfaces* **2014,** *6* (17), 14795-14800.

168. Farlow, J.; Seo, D.; Broaders, K. E.; Taylor, M. J.; Gartner, Z. J.; Jun, Y.-w., Formation of Targeted Monovalent Quantum Qots by Steric Exclusion. *Nat Meth* **2013,** *10* (12), 1203-1205.

169. Saran, R.; Huang, Z.; Liu, J., Phosphorothioate Nucleic Acids for Probing Metal Binding, Biosensing and Nanotechnology. *Coord. Chem. Rev.* **2021,** *428*, 213624.

170. Hess, B.; Kutzner, C.; van der Spoel, D.; Lindahl, E., GROMACS 4: Algorithms for Highly Efficient, Load-Balanced, and Scalable Molecular Simulation. *J. Chem. Theory Comput.* **2008,** *4* (3), 435-447.

171. Li, S.; Olson, W. K.; Lu, X.-J., Web 3DNA 2.0 for the Analysis, Visualization, and Modeling of 3D Nucleic Acid Structures. *Nucleic Acids Res.* **2019,** *47* (W1), W26-W34.

172. Yang, J.; Shi, G.; Tu, Y.; Fang, H., High Correlation between Oxidation Loci on Graphene Oxide. *Angew. Chem. Int. Ed.* **2014,** *53* (38), 10190-10194.

173. Maier, J. A.; Martinez, C.; Kasavajhala, K.; Wickstrom, L.; Hauser, K. E.; Simmerling, C., ff14SB: Improving the Accuracy of Protein Side Chain and Backbone Parameters from ff99SB. *J. Chem. Theory Comput.* **2015,** *11* (8), 3696-3713.

174. Jorgensen, W. L.; Chandrasekhar, J.; Madura, J. D.; Impey, R. W.; Klein, M. L., Comparison of Simple Potential Functions for Simulating Liquid Water. *J. Chem. Phys* **1983,** *79* (2), 926-935.

175. Stauffer, D.; Dragneva, N.; Floriano, W. B.; Mawhinney, R. C.; Fanchini, G.; French, S.; Rubel, O., An Atomic Charge Model for Graphene Oxide for Exploring its Bioadhesive Properties in Explicit Water. *J. Chem. Phys* **2014,** *141* (4), 044705.

176. Wang, J.; Wolf, R. M.; Caldwell, J. W.; Kollman, P. A.; Case, D. A., Development and Testing of a General Amber Force Field. *J. Comput. Chem.* **2004,** *25* (9), 1157-1174.

177. Darden, T.; York, D.; Pedersen, L., Particle Mesh Ewald: An N·log(N) Method for Ewald Sums in Large Systems. *J. Chem. Phys* **1993,** *98* (12), 10089-10092.

178. Hoke, G. D.; Draper, K.; Freier, S. M.; Gonzalez, C.; Driver, V. B.; Zounes, M. C.; Ecker, D. J., Effects of Phosphorothioate Capping on Antivense Oligonucleotide Stability, Hybridization and Antiviral Efficacy Versus Eerpes Simplex Virus Infection. *Nucleic Acids Res.* **1991,** *19* (20), 5743-5748.

179. Chen, C.; Song, G.; Ren, J.; Qu, X., A Simple and Sensitive Colorimetric pH Meter Based on DNA Conformational Switch and Gold Nanoparticle Aggregation. *Chem. Commun.* **2008,** (46), 6149-6151.

180. Huang, Z.; Liu, B.; Liu, J., Parallel Polyadenine Duplex Formation at Low pH Facilitates DNA Conjugation onto Gold Nanoparticles. *Langmuir* **2016,** *32* (45), 11986-11992.

181. Chakraborty, S.; Sharma, S.; Maiti, P. K.; Krishnan, Y., The Poly dA Helix: A New Structural Motif for High Performance DNA-based Molecular Switches. *Nucleic Acids Res.* **2009,** *37* (9), 2810-7.

182. Kanaori, K.; Sakamoto, S.; Yoshida, H.; Guga, P.; Stec, W.; Tajima, K.; Makino, K., Effect of Phosphorothioate Chirality on i-Motif Structure and Stability. *Biochemistry* **2004,** *43* (19), 5672-5679.

183. Kanehara, H.; Mizuguchi, M.; Tajima, K.; Kanaori, K.; Makino, K., Spectroscopic Evidence for the Formation of Four-Stranded Solution Structure of Oligodeoxycytidine Phosphorothioate. *Biochemistry* **1997,** *36* (7), 1790-1797.

184. Stein, C. A.; Subasinghe, C.; Shinozuka, K.; Cohen, J. S., Physicochemical Properties of Phosphorothioate Oligodeoxynucleotides. *Nucleic Acids Res.* **1988,** *16* (8), 3209-3221.

185. Kanaori, K.; Tamura, Y.; Wada, T.; Nishi, M.; Kanehara, H.; Morii, T.; Tajima, K.; Makino, K., Structure and Stability of the Consecutive Stereoregulated Chiral Phosphorothioate DNA Duplex. *Biochemistry* **1999,** *38* (49), 16058-16066.

186. Park, J. S.; Na, H.-K.; Min, D.-H.; Kim, D.-E., Desorption of Single-Stranded Nucleic Acids from Graphene Oxide by Disruption of Hydrogen Bonding. *Analyst* **2013,** *138* (6), 1745-1749.

187. Lu, C.; Liu, Y.; Ying, Y.; Liu, J., Comparison of MoS_2, WS_2, and Graphene Oxide for DNA Adsorption and Sensing. *Langmuir* **2017,** *33* (2), 630-637.

188. Raize, O.; Argaman, Y.; Yannai, S., Mechanisms of Biosorption of Different Heavy Metals by Brown Marine Macroalgae. *Biotechnol. Bioeng.* **2004,** *87* (4), 451-458.

189. Platts, J. A.; Howard, S. T.; Bracke, B. R. F., Directionality of Hydrogen Bonds to Sulfur and Oxygen. *J. Am. Chem. Soc.* **1996,** *118* (11), 2726-2733.

190. Ranganathan, S. V.; Halvorsen, K.; Myers, C. A.; Robertson, N. M.; Yigit, M. V.; Chen, A. A., Complex Thermodynamic Behavior of Single-Stranded Nucleic Acid Adsorption to Graphene Surfaces. *Langmuir* **2016,** *32* (24), 6028-6034.

191. Zhu, Y.; Murali, S.; Cai, W.; Li, X.; Suk, J. W.; Potts, J. R.; Ruoff, R. S., Graphene and Graphene Oxide: Synthesis, Properties, and Applications. *Adv. Mater.* **2010,** *22* (35), 3906-24.

192. Li, H.; Wu, J.; Yin, Z.; Zhang, H., Preparation and Applications of Mechanically Exfoliated Single-Layer and Multilayer MoS_2 and WSe_2 Nanosheets. *Acc. Chem. Res.* **2014,** *47* (4), 1067-1075.

193. Gutiérrez, H. R.; Perea-López, N.; Elías, A. L.; Berkdemir, A.; Wang, B.; Lv, R.; López-Urías, F.; Crespi, V. H.; Terrones, H.; Terrones, M., Extraordinary Room-Temperature Photoluminescence in Triangular WS_2 Monolayers. *Nano Lett.* **2013,** *13* (8), 3447-3454.

194. Ding, X.; Peng, F.; Zhou, J.; Gong, W.; Slaven, G.; Loh, K. P.; Lim, C. T.; Leong, D. T., Defect Engineered Bioactive Transition Metals Dichalcogenides Quantum Dots. *Nat. Commun.* **2019,** *10* (1), 41.

195. Zhang, J.; Li, Z.; Zhao, S.; Lu, Y., Size-Dependent Modulation of Graphene Oxide–Aptamer Interactions for an Amplified Fluorescence-based Detection of Aflatoxin B1 with a Tunable Dynamic Range. *Analyst* **2016,** *141* (13), 4029-4034.

196. Ran, J.; Gao, G.; Li, F.-T.; Ma, T.-Y.; Du, A.; Qiao, S.-Z., Ti_3C_2 MXene Co-catalyst on Metal Sulfide Photo-absorbers for Enhanced Visible-light Photocatalytic Hydrogen Production. *Nat. Commun.* **2017,** *8*, 13907.

197. Liu, G.; Zou, J.; Tang, Q.; Yang, X.; Zhang, Y.; Zhang, Q.; Huang, W.; Chen, P.; Shao, J.; Dong, X., Surface Modified Ti_3C_2 MXene Nanosheets for Tumor Targeting Photothermal/Photodynamic/Chemo Synergistic Therapy. *ACS Appl. Mater. Interfaces* **2017,** *9* (46), 40077-40086.

198. Dai, C.; Lin, H.; Xu, G.; Liu, Z.; Wu, R.; Chen, Y., Biocompatible 2D Titanium Carbide (MXenes) Composite Nanosheets for pH-Responsive MRI-Guided Tumor Hyperthermia. *Chem. Mater.* **2017,** *29* (20), 8637-8652.

199. Zheng, J.; Wang, B.; Ding, A.; Weng, B.; Chen, J., Synthesis of MXene/DNA/Pd/Pt Nanocomposite for Sensitive Detection of Dopamine. *J. Electroanal. Chem.* **2018,** *816*, 189-194.

200. Rakhi, R. B.; Nayak, P.; Xia, C.; Alshareef, H. N., Novel Amperometric Glucose Biosensor Based on MXene Nanocomposite. *Sci. Rep.* **2016,** *6*, 36422.

201. Er, D.; Li, J.; Naguib, M.; Gogotsi, Y.; Shenoy, V. B., Ti_3C_2 MXene as a High Capacity Electrode Material for Metal (Li, Na, K, Ca) Ion Batteries. *ACS Appl. Mater. Interfaces* **2014,** *6* (14), 11173-11179.

202. Wang, H.; Yang, R.; Yang, L.; Tan, W., Nucleic Acid Conjugated Nanomaterials for Enhanced Molecular Recognition. *ACS Nano* **2009,** *3* (9), 2451-2460.

203. Liu, Z.; Liu, B.; Ding, J.; Liu, J., Fluorescent Sensors Using DNA-functionalized Graphene Oxide. *Anal. Bioanal. Chem.* **2014,** *406* (27), 6885-6902.

204. Chen, D.; Feng, H.; Li, J., Graphene Oxide: Preparation, Functionalization, and Electrochemical Applications. *Chem. Rev.* **2012,** *112* (11), 6027-6053.

205. Lu, C.-H.; Yang, H.-H.; Zhu, C.-L.; Chen, X.; Chen, G.-N., A Graphene Platform for Sensing Biomolecules. *Angew. Chem.* **2009,** *121* (26), 4879-4881.

206. He, S.; Song, B.; Li, D.; Zhu, C.; Qi, W.; Wen, Y.; Wang, L.; Song, S.; Fang, H.; Fan, C., A Graphene Nanoprobe for Rapid, Sensitive, and Multicolor Fluorescent DNA Analysis. *Adv. Funct. Mater.* **2010,** *20* (3), 453-459.

207. Wang, T.; Zhu, R.; Zhuo, J.; Zhu, Z.; Shao, Y.; Li, M., Direct Detection of DNA below ppb Level Based on Thionin-Functionalized Layered MoS_2 Electrochemical Sensors. *Anal. Chem.* **2014,** *86* (24), 12064-12069.

208. Park, J. S.; Goo, N.-I.; Kim, D.-E., Mechanism of DNA Adsorption and Desorption on Graphene Oxide. *Langmuir* **2014,** *30* (42), 12587-12595.

209. Liang, X.; Garsuch, A.; Nazar, L. F., Sulfur Cathodes Based on Conductive MXene Nanosheets for High-Performance Lithium–Sulfur Batteries. *Angew. Chem. Int. Ed.* **2015,** *54* (13), 3907-3911.

210. Liu, F.; Zhou, A.; Chen, J.; Zhang, H.; Cao, J.; Wang, L.; Hu, Q., Preparation and Methane Adsorption of Two-Dimensional Carbide Ti_2C. *Adsorption* **2016,** *22* (7), 915-922.

211. Ahmed, B.; Anjum, D. H.; Hedhili, M. N.; Gogotsi, Y.; Alshareef, H. N., H_2O_2 Assisted Room Temperature Oxidation of Ti_2C MXene for Li-ion Battery Anodes. *Nanoscale* **2016,** *8* (14), 7580-7587.

212. Karwowska, E.; Basiak, D.; Zawada, A.; Ziemkowska, W.; Wojciechowski, T.; Jakubowska, D.; Olszyna, A., Biological Activity and Bio-sorption Properties of the Ti_2C Studied by Means of Zeta-potential and SEM. *Int. J. Electrochem. Sci* **2017,** *12*, 2159-2172.

213. Liu, J.; Lu, Y., Preparation of Aptamer-linked Gold Nanoparticle Purple Aggregates for Colorimetric Sensing of Analytes. *Nat. Protoc.* **2006,** *1*, 246.

214. Meng, Y.; Liu, P.; Zhou, W.; Ding, J.; Liu, J., Bioorthogonal DNA Adsorption on Polydopamine Nanoparticles Mediated by Metal Coordination for Highly Robust Sensing in Serum and Living Cells. *ACS Nano* **2018,** *12* (9), 9070-9080.

215. Ainalem, M.-L.; Kristen, N.; Edler, K. J.; Höök, F.; Sparr, E.; Nylander, T., DNA Binding to Zwitterionic Model Membranes. *Langmuir* **2010,** *26* (7), 4965-4976.

216. Jin, K.; Park, J.; Lee, J.; Yang, K. D.; Pradhan, G. K.; Sim, U.; Jeong, D.; Jang, H. L.; Park, S.; Kim, D.; Sung, N.-E.; Kim, S. H.; Han, S.; Nam, K. T., Hydrated Manganese(II) Phosphate ($Mn_3(PO_4)_2 \cdot 3H_2O$) as a Water Oxidation Catalyst. *J. Am. Chem. Soc.* **2014,** *136* (20), 7435-7443.

217. Wang, L.; Zhang, Z.; Liu, B.; Liu, Y.; Lopez, A.; Wu, J.; Liu, J., Interfacing DNA Oligonucleotides with Calcium Phosphate and Other Metal Phosphates. *Langmuir* **2017,** *34* (49), 14975-14982.

218. Zhao, Z.; Fan, H.; Zhou, G.; Bai, H.; Liang, H.; Wang, R.; Zhang, X.; Tan, W., Activatable Fluorescence/MRI Bimodal Platform for Tumor Cell Imaging via MnO_2 Nanosheet–Aptamer Nanoprobe. *J. Am. Chem. Soc.* **2014,** *136* (32), 11220-11223.

219. Liu, Y.; Tang, Z., Nanoscale Biocoordination Polymers: Novel Materials from an Old Topic. *Chem. - Eur. J.* **2012,** *18* (4), 1030-1037.

220. Zhou, P.; Shi, R.; Yao, J.-f.; Sheng, C.-f.; Li, H., Supramolecular Self-assembly of Nucleotide–metal Coordination Complexes: From Simple Molecules to Nanomaterials. *Coord. Chem. Rev.* **2015,** *292*, 107-143.

221. Jastrząb, R.; Nowak, M.; Skrobańska, M.; Tolińska, A.; Zabiszak, M.; Gabryel, M.; Marciniak, Ł.; Kaczmarek, M. T., DNA as a Target for Lanthanide(III) Complexes Influence. *Coord. Chem. Rev.* **2019,** *382*, 145-159.

222. Jiao, M.; Li, Z.; Li, X.; Zhang, Z.; Yuan, Q.; Vriesekoop, F.; Liang, H.; Liu, J., Solving the H_2O_2 By-product Problem Using a Catalase-mimicking Nanozyme Cascade to Enhance Glycolic Acid Oxidase. *Chem. Eng. J. (Lausanne)* **2020**, 124249.

223. Mu, J.; He, L. C.; Huang, P.; Chen, X. Y., Engineering of Nanoscale Coordination Polymers with Biomolecules for Advanced Applications. *Coord. Chem. Rev.* **2019,** *399*, 213039.

224. Terrón, A.; Tomàs, L.; Bauzá, A.; García-Raso, A.; Fiol, J. J.; Molins, E.; Frontera, A., The First X-ray Structure of a Silver−nucleotide Complex: Interaction of Ion Ag(i) with Cytidine-5′-monophosphate. *CrystEngComm* **2017,** *19* (39), 5830-5834.

225. Liang, H.; Jiang, S.; Yuan, Q.; Li, G.; Wang, F.; Zhang, Z.; Liu, J., Co-immobilization of Multiple Enzymes by Metal Coordinated Nucleotide Hydrogel Nanofibers: Improved Stability and an Enzyme Cascade for Glucose Detection. *Nanoscale* **2016,** *8* (11), 6071-6078.

226. Liang, H.; Zhang, Z.; Yuan, Q.; Liu, J., Self-healing Metal-coordinated Hydrogels Using Nucleotide Ligands. *Chem. Commun.* **2015,** *51* (82), 15196-15199.

227. Demirbaş, Ü.; Barut, B.; Özel, A.; Çelik, F.; Kantekin, H.; Sancak, K., Synthesis, Characterization and DNA Interaction Properties of the Novel Peripherally Tetra 4-(3-methyl-4-(3-morpholinopropyl)-5-oxo-4,5-Dihydro-1H-1,2,4-triazol-1-yl) Substituted Water Soluble Zn(II) and Cu(II) Phthalocyanines. *J. Mol. Struct.* **2019,** *1177*, 571-578.

228. Pu, F.; Ran, X.; Ren, J.; Qu, X., Artificial Tongue Based on Metal–biomolecule Coordination Polymer Nanoparticles. *Chem. Commun.* **2016,** *52* (16), 3410-3413.

229. Wang, F.; Liu, B.; Huang, P. J.; Liu, J., Rationally Designed Nucleobase and Nucleotide Coordinated Nanoparticles for Selective DNA Adsorption and Detection. *Anal. Chem.* **2013,** *85* (24), 12144-51.

230. Pu, F.; Ren, J.; Qu, X., Nucleobases, Nucleosides, and Nucleotides: Versatile Biomolecules for Generating Functional Nanomaterials. *Chem. Soc. Rev.* **2018,** *47* (4), 1285-1306.

231. Xu, L.; Zhang, Z.; Fang, X.; Liu, Y.; Liu, B.; Liu, J., Robust Hydrogels from Lanthanide Nucleotide Coordination with Evolving Nanostructures for a Highly Stable Protein Encapsulation. *ACS Appl. Mater. Interfaces* **2018,** *10* (17), 14321-14330.

232. Ma, Q.; Li, F.; Tang, J.; Meng, K.; Xu, X.; Yang, D., Luminescent Ultralong Microfibers Prepared through Supramolecular Self-Assembly of Lanthanide Ions and Thymidine in Water. *Chem. - Eur. J.* **2018,** *24* (71), 18890-18896.

233. Nishiyabu, R.; Aimé, C.; Gondo, R.; Noguchi, T.; Kimizuka, N., Confining Molecules within Aqueous Coordination Nanoparticles by Adaptive Molecular Self-Assembly. *Angew. Chem. Int. Ed.* **2009,** *48* (50), 9465-9468.

234. Johansson, M. K.; Cook, R. M.; Xu, J.; Raymond, K. N., Time Gating Improves Sensitivity in Energy Transfer Assays with Terbium Chelate/Dark Quencher Oligonucleotide Probes. *J. Am. Chem. Soc.* **2004,** *126* (50), 16451-16455.

235. Aimé, C.; Nishiyabu, R.; Gondo, R.; Kimizuka, N., Switching On Luminescence in Nucleotide/Lanthanide Coordination Nanoparticles via Synergistic Interactions with a Cofactor Ligand. *Chem. - Eur. J.* **2010,** *16* (12), 3604-3607.

236. Zeng, H.-H.; Qiu, W.-B.; Zhang, L.; Liang, R.-P.; Qiu, J.-D., Lanthanide Coordination Polymer Nanoparticles as an Excellent Artificial Peroxidase for Hydrogen Peroxide Detection. *Anal. Chem.* **2016,** *88* (12), 6342-6348.

237. Liang, H.; Lin, F.; Zhang, Z.; Liu, B.; Jiang, S.; Yuan, Q.; Liu, J., Multicopper Laccase Mimicking Nanozymes with Nucleotides as Ligands. *ACS Appl. Mater. Interfaces* **2017,** *9* (2), 1352-1360.

238. Yuan, H.; Bai, H.; Liu, L.; Lv, F.; Wang, S., A Glucose-powered Antimicrobial System Using Organic–inorganic Assembled Network Materials. *Chem. Commun.* **2015,** *51* (4), 722-724.

239. Duan, F.; Feng, X.; Yang, X.; Sun, W.; Jin, Y.; Liu, H.; Ge, K.; Li, Z.; Zhang, J., A Simple and Powerful Co-delivery System Based on pH-responsive Metal-organic Frameworks for Enhanced Cancer Immunotherapy. *Biomaterials* **2017,** *122*, 23-33.

240. Zhou, L.; Li, Z.; Liu, Z.; Yin, M.; Ren, J.; Qu, X., One-step Nucleotide-programmed Growth of Porous Upconversion Nanoparticles: Application to Cell Labeling and Drug Delivery. *Nanoscale* **2014,** *6* (3), 1445-1452.

241. Wang, C. L.; Di, Z. H.; Fan, Z. T.; Li, L. L., Self-assembly of DNA Nanostructures via Bioinspired Metal Ion Coordination. *Chem. Res. Chin. Univ.* **2019**.

242. Ruan, L.; Wang, M.; Zhou, M.; Lu, H.; Zhang, J.; Gao, J.; Chen, J.; Hu, Y., Doxorubicin–Metal Coordinated Micellar Nanoparticles for Intracellular Codelivery and Chemo/Chemodynamic Therapy in Vitro. *ACS Applied Bio Materials* **2019,** *2* (11), 4703-4707.

243. Storhoff, J. J.; Lazarides, A. A.; Mucic, R. C.; Mirkin, C. A.; Letsinger, R. L.; Schatz, G. C., What Controls the Optical Properties of DNA-Linked Gold Nanoparticle Assemblies? *J. Am. Chem. Soc.* **2000,** *122* (19), 4640-4650.

244. Lermusiaux, L.; Sereda, A.; Portier, B.; Larquet, E.; Bidault, S., Reversible Switching of the Interparticle Distance in DNA-Templated Gold Nanoparticle Dimers. *ACS Nano* **2012,** *6* (12), 10992-10998.

245. Liu, J. W.; Lu, Y., A Colorimetric Lead Biosensor Using DNAzyme-directed Assembly of Gold Nanoparticles. *J. Am. Chem. Soc.* **2003,** *125* (22), 6642-6643.

246. Hill, H. D.; Mirkin, C. A., The Bio-barcode Assay for the Detection of Protein and Nucleic Acid Targets Using DTT-induced Ligand Exchange. *Nat. Protoc.* **2006,** *1* (1), 324-336.

247. Hurst, S. J.; Lytton-Jean, A. K. R.; Mirkin, C. A., Maximizing DNA Loading on a Range of Gold Nanoparticle Sizes. *Anal. Chem.* **2006,** *78* (24), 8313-8318.

248. Curry, D.; Cameron, A.; MacDonald, B.; Nganou, C.; Scheller, H.; Marsh, J.; Beale, S.; Lu, M.; Shan, Z.; Kaliaperumal, R.; Xu, H.; Servos, M.; Bennett, C.; MacQuarrie, S.; Oakes, K. D.; Mkandawire, M.; Zhang, X., Adsorption of Doxorubicin on Citrate-capped Aold Nanoparticles: Insights into Engineering Potent Chemotherapeutic Delivery Systems. *Nanoscale* **2015,** *7* (46), 19611-19619.

249. Chinen, A. B.; Guan, C. M.; Ferrer, J. R.; Barnaby, S. N.; Merkel, T. J.; Mirkin, C. A., Nanoparticle Probes for the Detection of Cancer Biomarkers, Cells, and Tissues by Fluorescence. *Chem. Rev.* **2015,** *115* (19), 10530-10574.

250. Cecconello, A.; Besteiro, L. V.; Govorov, A. O.; Willner, I., Chiroplasmonic DNA-based Nanostructures. *Nat. Rev. Mater.* **2017,** *2* (9), 17039.

251. Ebrahimi, S. B.; Samanta, D.; Mirkin, C. A., DNA-Based Nanostructures for Live-Cell Analysis. *J. Am. Chem. Soc.* **2020,** *142* (26), 11343-11356.

252. Laramy, C. R.; O'Brien, M. N.; Mirkin, C. A., Crystal Engineering with DNA. *Nat. Rev. Mater.* **2019,** *4* (3), 201-224.

253. Sharifi, M.; Faryabi, K.; Talaei, A. J.; Shekha, M. S.; Ale-Ebrahim, M.; Salihi, A.; Nanakali, N. M. Q.; Aziz, F. M.; Rasti, B.; Hasan, A.; Falahati, M., Antioxidant Properties of Gold Nanozyme: A Review. *J. Mol. Liq.* **2020,** *297*, 112004.

254. Zhang, Y.; Li, S.; Liu, H.; Long, W.; Zhang, X. D., Enzyme-Like Properties of Gold Clusters for Biomedical Application. *Front. Chem. (Columbus, Ohio)* **2020,** *8* (219), 219.

255. Zhang, F.; Wang, S.; Liu, J., Gold Nanoparticles Adsorb DNA and Aptamer Probes Too Strongly and a Comparison with Graphene Oxide for Biosensing. *Anal. Chem.* **2019,** *91* (22), 14743-14750.

256. Wang, S.; Chen, Z.; Choo, J.; Chen, L., Naked-eye Sensitive ELISA-like Assay Based on Gold-enhanced Peroxidase-like Immunogold Activity. *Anal. Bioanal. Chem.* **2016,** *408* (4), 1015-1022.

257. Chen, J.; Wu, W.; Huang, L.; Ma, Q.; Dong, S., Self-Indicative Gold Nanozyme for H_2O_2 and Glucose Sensing. *Chem. - Eur. J.* **2019,** *25* (51), 11940-11944.

258. Biella, S.; Prati, L.; Rossi, M., Selective Oxidation of D-Glucose on Gold Catalyst. *J. Catal.* **2002,** *206* (2), 242-247.

259. Zhang, Z.; Bragg, L. M.; Servos, M. R.; Liu, J., Gold Nanoparticles as Dehydrogenase Mimicking Nanozymes for Estradiol Degradation. *Chin. Chem. Lett.* **2019,** *30* (9), 1655-1658.

260. Huang, Y.; Ren, J.; Qu, X., Nanozymes: Classification, Catalytic Mechanisms, Activity Regulation, and Applications. *Chem. Rev.* **2019,** *119* (6), 4357-4412.

261. Jiang, D.; Ni, D.; Rosenkrans, Z. T.; Huang, P.; Yan, X.; Cai, W., Nanozyme: New Horizons for Responsive Biomedical Applications. *Chem. Soc. Rev.* **2019,** *48* (14), 3683-3704.

262. Tao, X.; Wang, X.; Liu, B.; Liu, J., Conjugation of Antibodies and Aptamers on Nanozymes for Developing Biosensors. *Biosens. Bioelectron.* **2020,** *168*, 112537.

263. Lopez, A.; Liu, J., Coordination Nanoparticles Formed by Fluorescent 2-Aminopurine and Au^{3+}: Stability and Nanozyme Activities. *J. Anal. Test.* **2019,** *3* (3), 219-227.

264. Liu, B.; Liu, J., Surface Modification of Nanozymes. *Nano Res.* **2017,** *10* (4), 1125-1148.

265. Liu, Y.; Xiang, Y.; Zhen, Y.; Guo, R., Halide Ion-Induced Switching of Gold Nanozyme Activity Based on Au–X Interactions. *Langmuir* **2017,** *33* (25), 6372-6381.

266. Ray, S.; Biswas, R.; Banerjee, R.; Biswas, P., A Gold Nanoparticle-intercalated Mesoporous Silica-based Nanozyme for the Selective Colorimetric Detection of Dopamine. *Nanoscale Adv.* **2020,** *2* (2), 734-745.

267. Liu, S.; Han, M.-Y., Silica-Coated Metal Nanoparticles. *Chem. - Asian J.* **2010,** *5* (1), 36-45.

268. Guerrero-Martínez, A.; Pérez-Juste, J.; Liz-Marzán, L. M., Recent Progress on Silica Coating of Nanoparticles and Related Nanomaterials. *Adv. Mater.* **2010,** *22* (11), 1182-1195.

269. Lukosi, M.; Zhu, H.; Dai, S., Recent Advances in Gold-metal Oxide Core-shell Nanoparticles: Synthesis, Characterization, and Their Application for Heterogeneous Catalysis. *Front. Chem. Sci. Eng.* **2016,** *10* (1), 39-56.

270. Zhou, W.; Ding, J.; Liu, J., A Platinum Shell for Ultraslow Ligand Exchange: Unmodified DNA Adsorbing More Stably on Platinum than Thiol and Dithiol on Gold. *Chem. Commun.* **2015,** *51* (60), 12084-7.

271. Gawande, M. B.; Goswami, A.; Asefa, T.; Guo, H.; Biradar, A. V.; Peng, D.-L.; Zboril, R.; Varma, R. S., Core–shell Nanoparticles: Synthesis and Applications in Catalysis and Electrocatalysis. *Chem. Soc. Rev.* **2015,** *44* (21), 7540-7590.

272. Qing, Z.; Luo, G.; Xing, S.; Zou, Z.; Lei, Y.; Liu, J.; Yang, R., Pt–S Bond-Mediated Nanoflares for High-Fidelity Intracellular Applications by Avoiding Thiol Cleavage. *Angew. Chem. Int. Ed.* **2020,** *59* (33), 14044-14048.

273. Zhao, J.; Jian, Z.; Ma, J.; Wang, F.; Hu, Y.-S.; Chen, W.; Chen, L.; Liu, H.; Dai, S., Monodisperse Iron Phosphate Nanospheres: Preparation and Application in Energy Storage. *ChemSusChem* **2012,** *5* (8), 1495-1500.

274. Yin, Y.; Zhang, H.; Wu, P.; Zhou, B.; Cai, C., Iron Phosphate Nanostructures Synthesized by Microwave Method and Their Applications in Biosensing. *Nanotechnology* **2010,** *21* (42), 425504.

275. Wang, W.; Jiang, X.; Chen, K., Iron Phosphate Microflowers as Peroxidase Mimic and Superoxide Dismutase Mimic for Biocatalysis and Biosensing. *Chem. Commun.* **2012,** *48* (58), 7289-7291.

276. Zhang, T.; Lu, Y.; Luo, G., Synthesis of Hierarchical Iron Hydrogen Phosphate Crystal as a Robust Peroxidase Mimic for Stable H_2O_2 Detection. *ACS Appl. Mater. Interfaces* **2014,** *6* (16), 14433-14438.

277. Zhong, D.; Liu, L.; Li, D.; Wei, C.; Wang, Q.; Hao, G.; Zhao, Q.; Li, J., Facile and Fast Fabrication of Iron-phosphate Supported on Nickel Foam as a Highly Efficient and Stable Oxygen Evolution Catalyst. *J. Mater. Chem. A* **2017,** *5* (35), 18627-18633.

278. Song, C.; Ding, W.; Zhao, W.; Liu, H.; Wang, J.; Yao, Y.; Yao, C., High Peroxidase-like Activity Realized by Facile Synthesis of FeS_2 Nanoparticles for Sensitive Colorimetric Detection of H_2O_2 and Glutathione. *Biosens. Bioelectron.* **2020,** *151*, 111983.

279. Zhou, D.; Zeng, K.; Yang, M., Gold Nanoparticle-loaded Hollow Prussian Blue Nanoparticles with Peroxidase-like Activity for Colorimetric Determination of L-lactic Acid. *Microchim. Acta* **2019,** *186* (2), 121.

280. Jimmy Huang, P.-J.; Yang, J.; Chong, K.; Ma, Q.; Li, M.; Zhang, F.; Moon, W. J.; Zhang, G.; Liu, J., Good's Buffers have Various Affinities to Gold Nanoparticles Regulating Fluorescent and Colorimetric DNA Sensing. *Chem. Sci.* **2020,** *11* (26), 6795-6804.

281. Kwon, K.; Lee, K. Y.; Lee, Y. W.; Kim, M.; Heo, J.; Ahn, S. J.; Han, S. W., Controlled Synthesis of Icosahedral Gold Nanoparticles and Their Surface-Enhanced Raman Scattering Property. *J. Phys. Chem. C* **2007,** *111* (3), 1161-1165.

282. Liu, B.; Liu, J., Freezing-Driven DNA Adsorption on Gold Nanoparticles: Tolerating Extremely Low Salt Concentration but Requiring High DNA Concentration. *Langmuir* **2019,** *35* (19), 6476-6482.

283. Liz-Marzán, L. M.; Giersig, M.; Mulvaney, P., Synthesis of Nanosized Gold−Silica Core−Shell Particles. *Langmuir* **1996,** *12* (18), 4329-4335.

284. Liu, S. H.; Han, M. Y., Synthesis, Functionalization, and Bioconjugation of Monodisperse, Silica-Coated Gold Nanoparticles: Robust Bioprobes. *Adv. Funct. Mater.* **2005,** *15* (6), 961-967.

285. Zhang, T.; Lu, Y.; Luo, G., Effects of Temperature and Phosphoric Acid Addition on the Solubility of Iron Phosphate Dihydrate in Aqueous Solutions. *Chin. J. Chem. Eng.* **2017,** *25* (2), 211-215.

286. Zhao, Y.; Wang, Y.; Mathur, A.; Wang, Y.; Maheshwari, V.; Su, H.; Liu, J., Fluoride-capped Nanoceria as a Highly Efficient Oxidase-mimicking Nanozyme: Inhibiting Product Adsorption and Increasing Oxygen Vacancies. *Nanoscale* **2019,** *11* (38), 17841-17850.

287. Logan, N.; McVey, C.; Elliott, C.; Cao, C., Amalgamated Gold-nanoalloys with Enhanced Catalytic Activity for the Detection of Mercury Ions (Hg^{2+}) in Seawater Samples. *Nano Res.* **2020,** *13* (4), 989-998.

288. Lien, C.-W.; Tseng, Y.-T.; Huang, C.-C.; Chang, H.-T., Logic Control of Enzyme-Like Gold Nanoparticles for Selective Detection of Lead and Mercury Ions. *Anal. Chem.* **2014,** *86* (4), 2065-2072.

289. Li, Y.; Liu, J., Nanozyme's Catching Up: Activity, Specificity, Reaction Conditions and Reaction Types. *Mater. Horiz.* **2021,** *8* (2), 336-350.

290. Ma, X.; Lin, Y.; Guo, L.; Qiu, B.; Chen, G.; Yang, H.-h.; Lin, Z., A Universal Multicolor Immunosensor for Semiquantitative Visual Detection of Biomarkers with the Naked Eyes. *Biosens. Bioelectron.* **2017,** *87*, 122-128.

291. Ma, X.; Chen, Z.; Kannan, P.; Lin, Z.; Qiu, B.; Guo, L., Gold Nanorods as Colorful Chromogenic Substrates for Semiquantitative Detection of Nucleic Acids, Proteins, and Small Molecules with the Naked Eye. *Anal. Chem.* **2016,** *88* (6), 3227-3234.

292. Chen, Z.; Chen, C.; Huang, H.; Luo, F.; Guo, L.; Zhang, L.; Lin, Z.; Chen, G., Target-Induced Horseradish Peroxidase Deactivation for Multicolor Colorimetric Assay of Hydrogen Sulfide in Rat Brain Microdialysis. *Anal. Chem.* **2018,** *90* (10), 6222-6228.

293. Zhu, Q.; Wu, J.; Zhao, J.; Ni, W., Role of Bromide in Hydrogen Peroxide Oxidation of CTAB-Stabilized Gold Nanorods in Aqueous Solutions. *Langmuir* **2015,** *31* (14), 4072-4077.

294. Tsung, C.-K.; Kou, X.; Shi, Q.; Zhang, J.; Yeung, M. H.; Wang, J.; Stucky, G. D., Selective Shortening of Single-Crystalline Gold Nanorods by Mild Oxidation. *J. Am. Chem. Soc.* **2006,** *128* (16), 5352-5353.

295. Lin, Y.; Zhao, M.; Guo, Y.; Ma, X.; Luo, F.; Guo, L.; Qiu, B.; Chen, G.; Lin, Z., Multicolor Colormetric Biosensor for the Determination of Glucose based on the Etching of Gold Nanorods. *Sci. Rep.* **2016,** *6* (1), 37879.

296. Wu, S.; Li, D.; Gao, Z.; Wang, J., Controlled Eetching of Gold Nanorods by the Au(III)-CTAB Complex, and Its Application to Semi-quantitative Visual Determination of Organophosphorus Pesticides. *Microchim. Acta* **2017,** *184* (11), 4383-4391.

297. Chen, L.; Huang, Y.; Xing, T. T.; Ge, L.; Yang, T.; Chen, B.; Huang, C. Z., A Portable Multi-channel Sensing Device Using Au Nano-urchins as Probes for Melamine Detection in Milk. *J. Mater. Chem. C* **2017,** *5* (31), 7806-7812.

298. Chen, B.; Liu, C.; Shang, L.; Guo, H.; Qin, J.; Ge, L.; Jing, C. J.; Feng, C.; Hayashi, K., Electric-field Enhancement of Molecularly Imprinted Sol–gel-coated Au Nano-urchin Sensors for Vapor Detection of Plant Biomarkers. *J. Mater. Chem. C* **2020,** *8* (1), 262-269.

299. Li, J.; Wang, W.; Zhao, L.; Rong, L.; Lan, S.; Sun, H.; Zhang, H.; Yang, B., Hydroquinone-Assisted Synthesis of Branched Au–Ag Nanoparticles with Polydopamine Coating as Highly Efficient Photothermal Agents. *ACS Appl. Mater. Interfaces* **2015,** *7* (21), 11613-11623.

300. Ong, Z. Y.; Chen, S.; Nabavi, E.; Regoutz, A.; Payne, D. J.; Elson, D. S.; Dexter, D. T.; Dunlop, I. E.; Porter, A. E., Multibranched Gold Nanoparticles with Intrinsic LAT-1 Targeting Capabilities for Selective Photothermal Therapy of Breast Cancer. *ACS Appl. Mater. Interfaces* **2017,** *9* (45), 39259-39270.

301. Li, J.; Wu, J.; Zhang, X.; Liu, Y.; Zhou, D.; Sun, H.; Zhang, H.; Yang, B., Controllable Synthesis of Stable Urchin-like Gold Nanoparticles Using Hydroquinone to Tune the Reactivity of Gold Chloride. *J. Phys. Chem. C* **2011,** *115* (9), 3630-3637.

302. Perrault, S. D.; Chan, W. C. W., Synthesis and Surface Modification of Highly Monodispersed, Spherical Gold Nanoparticles of 50−200 nm. *J. Am. Chem. Soc.* **2009,** *131* (47), 17042-17043.

303. Xianyu, Y.; Lin, Y.; Chen, Q.; Belessiotis-Richards, A.; Stevens, M. M.; Thomas, M. R., Iodide-Mediated Rapid and Sensitive Surface Etching of Gold Nanostars for Biosensing. *Angew. Chem. Int. Ed.* **2021,** *60* (18), 9891-9896.

304. Yang, L.; Zhou, Z.; Song, J.; Chen, X., Anisotropic Nanomaterials for Shape-dependent Physicochemical and Biomedical Applications. *Chem. Soc. Rev.* **2019,** *48* (19), 5140-5176.

305. Xi, W.; Haes, A. J., Elucidation of HEPES Affinity to and Structure on Gold Nanostars. *J. Am. Chem. Soc.* **2019,** *141* (9), 4034-4042.

306. Li, J.; Han, J.; Xu, T.; Guo, C.; Bu, X.; Zhang, H.; Wang, L.; Sun, H.; Yang, B., Coating Urchinlike Gold Nanoparticles with Polypyrrole Thin Shells To Produce Photothermal Agents with High Stability and Photothermal Transduction Efficiency. *Langmuir* **2013,** *29* (23), 7102-7110.

307. Shan, Z.; Lyu, M.; Curry, D.; Oakley, D.; Oakes, K.; Zhang, X., Cu-DNAzyme Facilitates Highly Sensitive Immunoassay. *Chin. Chem. Lett.* **2019,** *30* (9), 1652-1654.

308. Chen, Z.-J.; Huang, Z.; Huang, S.; Zhao, J.-L.; Sun, Y.; Xu, Z.-L.; Liu, J., Effect of Proteins on the Oxidase-like Activity of CeO_2 Nanozymes for Immunoassays. *Analyst* **2021,** *146* (3), 864-873.

309. Frens, G., Controlled Nucleation for the Regulation of the Particle Size in Monodisperse Gold Suspensions. *Nature, Phys. Sci.* **1973,** *241* (105), 20-22.

310. Wei, W.; Wang, Y.; Ji, J.; Zuo, S.; Li, W.; Bai, F.; Fan, H., Fabrication of Large-Area Arrays of Vertically Aligned Gold Nanorods. *Nano Lett.* **2018,** *18* (7), 4467-4472.

311. Grys, D. B.; de Nijs, B.; Salmon, A. R.; Huang, J.; Wang, W.; Chen, W. H.; Scherman, O. A.; Baumberg, J. J., Citrate Coordination and Bridging of Gold Nanoparticles: The Role of Gold Adatoms in AuNP Aging. *ACS Nano* **2020,** *14* (7), 8689-8696.

312. Al-Johani, H.; Abou-Hamad, E.; Jedidi, A.; Widdifield, C. M.; Viger-Gravel, J.; Sangaru, S. S.; Gajan, D.; Anjum, D. H.; Ould-Chikh, S.; Hedhili, M. N.; Gurinov, A.; Kelly, M. J.; El Eter, M.; Cavallo, L.; Emsley, L.; Basset, J. M., The Structure and Binding Mode of Citrate in the Stabilization of Gold Nanoparticles. *Nat Chem* **2017,** *9* (9), 890-895.

313. Liu, B.; Wu, P.; Huang, Z.; Ma, L.; Liu, J., Bromide as a Robust Backfiller on Gold for Precise Control of DNA Conformation and High Stability of Spherical Nucleic Acids. *J. Am. Chem. Soc.* **2018,** *140* (13), 4499-4502.

314. Saa, L.; Coronado-Puchau, M.; Pavlov, V.; Liz-Marzán, L. M., Enzymatic Etching of Gold Nanorods by Horseradish Peroxidase and Application to Blood Glucose Detection. *Nanoscale* **2014,** *6* (13), 7405-7409.

315. Hauwiller, M. R.; Ye, X.; Jones, M. R.; Chan, C. M.; Calvin, J. J.; Crook, M. F.; Zheng, H.; Alivisatos, A. P., Tracking the Effects of Ligands on Oxidative Etching of Gold Nanorods in Graphene Liquid Cell Electron Microscopy. *ACS Nano* **2020,** *14* (8), 10239-10250.

316. Lohse, S. E.; Burrows, N. D.; Scarabelli, L.; Liz-Marzán, L. M.; Murphy, C. J., Anisotropic Noble Metal Nanocrystal Growth: The Role of Halides. *Chem. Mater.* **2014,** *26* (1), 34-43.

317. Meena, S. K.; Celiksoy, S.; Schäfer, P.; Henkel, A.; Sönnichsen, C.; Sulpizi, M., The Role of Halide Ions in the Anisotropic Growth of Gold Nanoparticles: A Microscopic, Atomistic Perspective. *Phys. Chem. Chem. Phys.* **2016,** *18* (19), 13246-13254.

318. Almora-Barrios, N.; Novell-Leruth, G.; Whiting, P.; Liz-Marzán, L. M.; López, N., Theoretical Description of the Role of Halides, Silver, and Surfactants on the Structure of Gold Nanorods. *Nano Lett.* **2014,** *14* (2), 871-875.

319. Rodríguez-Lorenzo, L.; Romo-Herrera, J. M.; Pérez-Juste, J.; Alvarez-Puebla, R. A.; Liz-Marzán, L. M., Reshaping and LSPR tuning of Au nanostars in the presence of CTAB. *J. Mater. Chem.* **2011,** *21* (31), 11544-11549.

320. Huang, X.; Yang, J.; Zhang, W.; Zhang, Z.; An, Z., Determination of the Critical Micelle Concentration of Cationic Surfactants: An Undergraduate Experiment. *J. Chem. Educ.* **1999,** *76* (1), 93.

321. Wang, L.; Verrall, R. E., Apparent Molar Volume and Apparent Molar Adiabatic Compressibility Studies of Anesthetic Molecules in Aqueous Micelle Solutions of CTAB and CTAC as a Function of Surfactant Concentration and Temperature. *J. Phys. Chem. C* **1994,** *98* (16), 4368-4374.

322. Ni, W.; Kou, X.; Yang, Z.; Wang, J., Tailoring Longitudinal Surface Plasmon Wavelengths, Scattering and Absorption Cross Sections of Gold Nanorods. *ACS Nano* **2008,** *2* (4), 677-686.

323. Chattopadhyay, K.; Mazumdar, S., Structural and Conformational Stability of Horseradish Peroxidase: Effect of Temperature and pH. *Biochemistry* **2000,** *39* (1), 263-270.

324. Meier, J.; M Hofferber, E.; A Stapleton, J.; M Iverson, N., Hydrogen Peroxide Sensors for Biomedical Applications. *Chemosensors* **2019,** *7* (4).

325. Liu, F.; Yang, L.; Yin, X.; Liu, X.; Ge, L.; Li, F., A Facile Homogeneous Electrochemical Biosensing Strategy Based on Displacement Reaction for Intracellular and Extracellular Hydrogen Peroxide Detection. *Biosens. Bioelectron.* **2019,** *141*, 111446.

326. Li, Q.; Niu, J.; Dou, M.; Zhang, Z.; Wang, F., Porous Microtubes of Nickel-cobalt Double Oxides as Non-enzymatic Hydrogen Peroxide Sensors. *Chin. Chem. Lett.* **2021,** *32* (3), 1181-1185.

327. Lu, M.; Su, L.; Luo, Y.; Ma, X.; Duan, Z.; Zhu, D.; Xiong, Y., Gold Nanoparticle Etching Induced by an Enzymatic-like Reaction for the Colorimetric Detection of Hydrogen Peroxide and Glucose. *Anal. Methods* **2019,** *11* (37), 4829-4834.

328. Zhang, Z.; Liu, J., Intracellular Delivery of a Molecularly Imprinted Peroxidase Mimicking DNAzyme for Selective Oxidation. *Mater. Horiz.* **2018,** *5* (4), 738-744.

329. Zhang, Z.; Liu, J., Molecular Imprinting with Functional DNA. *Small* **2019,** *15* (26), 1805246.